THE IMPACT OF HURRICANE IKE ON THE GEOMORPHOLOGY OF FOLLETT'S ISLAND, TEXAS – SHORT AND LONG TERM EFFECTS

A Thesis

by

CRAIG F. HARTER

Submitted to the Office of Graduate and Professional Studies of
Texas A&M University
in partial fulfillment of the requirements for the degree of

MASTER OF SCIENCE

Chair of Committee,	James Kaihatu
Co-Chair of Committee,	Jens Figlus
Committee Member,	Tim Dellapenna
Head of Department,	Robin Autenrieth

August 2015

Major Subject: Ocean Engineering

ABSTRACT

In many places along the U.S. East and Gulf Coast, barrier islands are the first line of defense against extreme weather events threatening our coastlines. Follett's Island is a sediment-starved barrier island located on the Upper Texas Coast; a stretch of coastline that experiences on average four hurricanes and four tropical cyclones per decade. As the topic of this thesis the impact of Hurricane Ike on Follett's Island (FI), TX is studied. The goal of this study is to address how Hurricane Ike affected the sediment supply on the subaerial beach and foredune of FI, how the island recovered following the hurricane, and what physical processes governed the response of the island during the hurricane.

This study first outlines the collection of available hydrographic, atmospheric, aerial and survey data and provides an analysis of these data to characterize the long term metocean and geomorphological state of the island. It was found that water levels at FI during Hurricane Ike exceeded the 100 year water levels, and wave heights matched roughly the 40 year exceedance levels. From LiDAR surveys, it is clear that despite an initial sediment volume loss after the hurricane, the foredune and subaerial beach ultimately experienced a net gain in sediment volume (up to 25%), and an extension of the shoreline (up to 25 m) after a five year recovery period.

Numerical modeling tools XBeach and CSHORE were employed in an attempt to numerically reproduce the observed effects of the hurricane on FI. The ultimate goal of the numerical modeling is to show a real time response of the island during the passing of the storm, rather than the before and after snapshots provided by LiDAR data. XBeach displayed a decent model skill of 0.34 and was very useful in qualitatively visualizing erosion and deposition patterns. CSHORE also displayed a decent model skill of 0.33 and was able to accurately predict the post-storm beach slope and shoreline, but was less effective at simulating the foredune morphology.

Based on these data, the subaerial beach and foredune ultimately experienced a net gain in sediment volume after recovering from Hurricane Ike. This is a phenomenon that

is contrary to the findings of other studies, and thus it is clear that sediment-starved barrier islands like FI need fundamentally different coastal protection considerations than other coastal systems.

ACKNOWLEDGEMENTS

I would foremost like to thank my faculty advisor and committee co-chair, Dr. Jens Figlus for being extremely flexible and accommodating of my needs and for being a tremendous mentor through this journey. I'd also like to thank my official committee chair, Dr. James Kaihatu, and committee member Dr. Tim Dellapenna, for their guidance and support throughout the course of this research.

Support during the data mining process was provided by the Texas General Land Office, Dr. Casey Dietrich of NC State University and Coast & Harbor Engineering, a Division of Hatch-Mott McDonald. This publication was supported by grants from the Texas General Land Office and NOAA through the Texas Coastal Management Program, Grant number 13-431-000-7890 and from an Institutional Grant (NA14OAR4170102) to the Texas Sea Grant College Program from the National Sea Grant Office, National Oceanic and Atmospheric Administration, U.S. Department of Commerce. In addition,

Thanks also to my good friends for their support through this process (I'm sorry if I've been too busy for you this past year), and to the wonderful staff at TAMU and TAMUG who happily assisted me throughout this process. Finally, and most importantly, thank you to my mother, father and sisters for their continued love and encouragement over the past 28 years.

NOMENCLATURE

CR-257	Bluewater highway
CSTORM	Coastal storm modeling system
D_{50}	Median grain size
D_{90}	90th percentile grain size
DEM	Digital elevation model
DoC	Department of Commerce
ERDC	USACE Engineer Research and Development Center
FI	Follett's island
GEV	Generalized extreme value
GLO	Texas General Land Office
GMT	Greenwich mean time
H_{rms}	Root-mean-square wave height
H_s	Significant wave height
IG	Infragravity
Ike	Hurricane Ike
LATEX	Louisiana-Texas
LiDAR	Light detection and ranging
MHW	Mean high water
MHHW	Mean higher high water
MLW	Mean low water
MLLW	Mean lower low water
Morfac	Morphological acceleration
MSL	Mean sea level
NAD83	North American Datum of 1983
NAIP	National Agriculture Imagery Program
NAVD88	North American Vertical Datum of 1988
NGDC	NOAA National Geophysical Data Center

NOAA	National Oceanographic and Atmospheric Administration
Point cloud	Set of non-gridded data points in some 3D coordinate system
RMS	Root mean square
SIFT	Short-term inundation forecasting for tsunamis
SLP	San Luis Pass
Smax	Maximum shields number
SMS	Surface water modeling software
TAMU	Texas A&M University
T_p	Peak wave period
TxDAPA	Texas Digital Aerial Photo Archive
USACE	United States Army Corps of Engineers
USGS	United States Geological Survey
UT-BEG	University of Texas Bureau of Economic Geology
UTC	Coordinated universal time
UTM	Universal transverse mercator coordinate system
WSEL	Water surface elevation

TABLE OF CONTENTS

Page

LIST OF FIGURES

Page

LIST OF TABLES

Page

1. INTRODUCTION

In many places along the U.S. East and Gulf Coast, barrier islands are the first line of defense against extreme weather events threatening our coastlines. Barrier islands comprise roughly 13% of the world's shorelines and 85% of the East and Gulf Coasts of the United States. Barrier islands are usually characterized by elongate bodies of sand or gravel separated from the mainland by a lagoon or marsh [6][20].

The three prominent theories explaining barrier island creation are those proposed by Hoyt (1967), de Beaumont (1845) and Gilbert (1885), all of which are summarized by Dalrymple (2004) [6]. Hoyt's theory describes the creation of barrier islands as the "drowning in place" of existing coastal dune features during periods of rapid sea level rise (such as during the late Holocene epoch). The de Beaumont theory describes the formation of barrier islands as a result of a cross-shore sediment balance, whereby an offshore bar is created and then rises in elevation until it becomes subaerial. Finally, the Gilbert theory postulates that barrier islands are created by longshore sediment transport whereby spits are formed in the downdrift direction from features that protrude the coastline (like headlands and inlets), and eventually become disconnected from said features. It is likely that all these theories are valid at different locations and times, and these theories are not necessarily mutually exclusive.

The morphological evolution of barrier islands depends on both long-term and short-term processes and is inherently linked to local sediment availability and local relative sea level rise [22][48][37]. Leatherman (1979) analyzed maps, charts and aerial photographs of Assateague Island, Maryland to identify the respective contributions of storm-driven overwash and tidal inlet dynamics to the overall migration patterns of barrier islands. Leatherman argued that flood-tidal delta formation and migration is the primary contributor to landward migration of the backshore. However, it was also argued that there is a critical width (that varies with the environment) below which hurricane overwash can make a significant contribution to landward migration of a barrier island [22]. In other words, above this critical width, overwash deposits do not

reach the bay, and are instead returned to the beach and foredune system by aeolian transport as the island recovers. However, below this critical width, overwash deposits can reach the bay, thus incrementally contributing to landward migration of the barrier island. Leatherman noted that these observations are specific to sediment-starved systems with prevalent offshore winds [22]. A schematic of a typical barrier island is shown in Figure 1.1. Moving from the Gulf side toward land, the subaqueous upper shoreface merges with the forebeach at the lower tide level. The forebeach is generally a milder slope than the upper shoreface, and in areas where the beach is wide, a beach berm also exists with either a flat or negatively sloping back beach which extends to the toe of the foredune. If no back beach exists, the forebeach extends directly to the dune toe. The foredune is marked by a rapid rise in elevation which typically crests as the highest elevation on the island before rapidly decreasing in elevation and merging with a level back-barrier, which extends to the back bay.

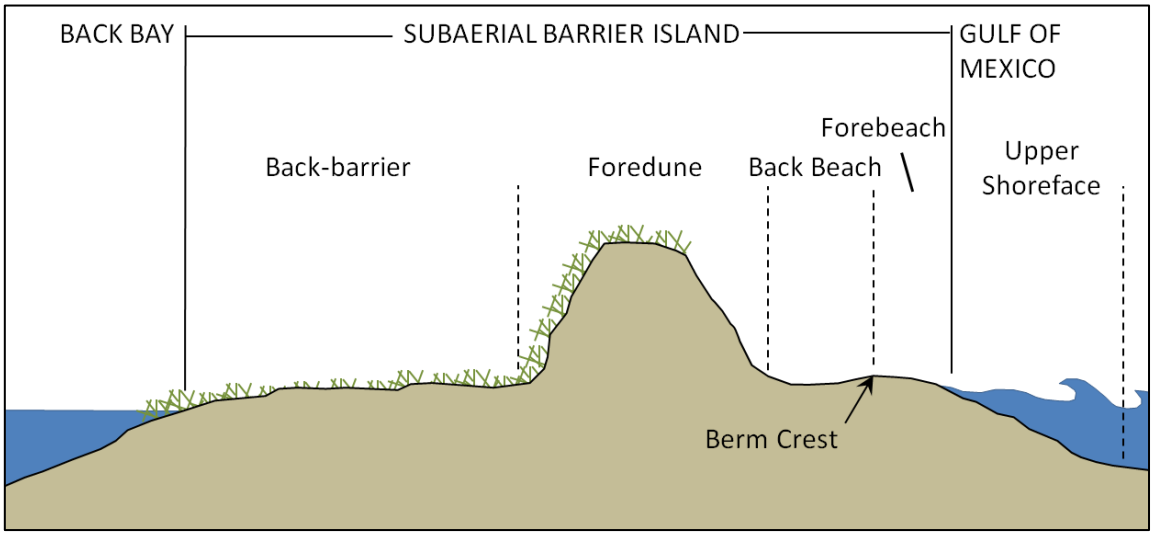

Figure 1.1: Schematic of the barrier island system showing the different zones of the subaerial island as well as the offshore and back-bay regions.

Although the long-term migration of barrier islands is episodic in nature, the island morphology in the immediate wake of a storm will not reflect the long-term morphology trend. The island must first undergo a recovery period until an equilibrium profile is reached. Morton et al. (1994) studied the recovery process of Galveston Island for a ten year period after Hurricane Alicia [29]. This study describes the stages of post-storm recovery of fine-grain sand beaches along a microtidal coast (Figure 1.2). It was found that the post storm recovery occurs in four stages: (1) rapid forebeach accretion, (2) backbeach aggradation, (3) foredune formation, and (4) foredune expansion and vegetation recolonization. Stage 1 recovery primarily involves onshore transport of sand that was stored directly offshore in the bars and on the upper shoreface. This occurs fairly rapidly as the equilibrium forebeach is reestablished. Stage 2 of recovery mostly involves subaerial deposition of sediment due to partial flooding of the back beach and aeolian transport, raising the elevation of the berm crest. This raising of the berm crest reduces the frequency of flooding, making it a critical step for reestablishing the foredune in Stage 3. During Stage 3, wind-blown dry sand is able to accumulate around clusters of vegetation and debris, facilitating dune growth. Stage 4 of recovery is characterized by stabilization of the dune vegetation, allowing the foredune to grow taller and wider and become more stable [29].

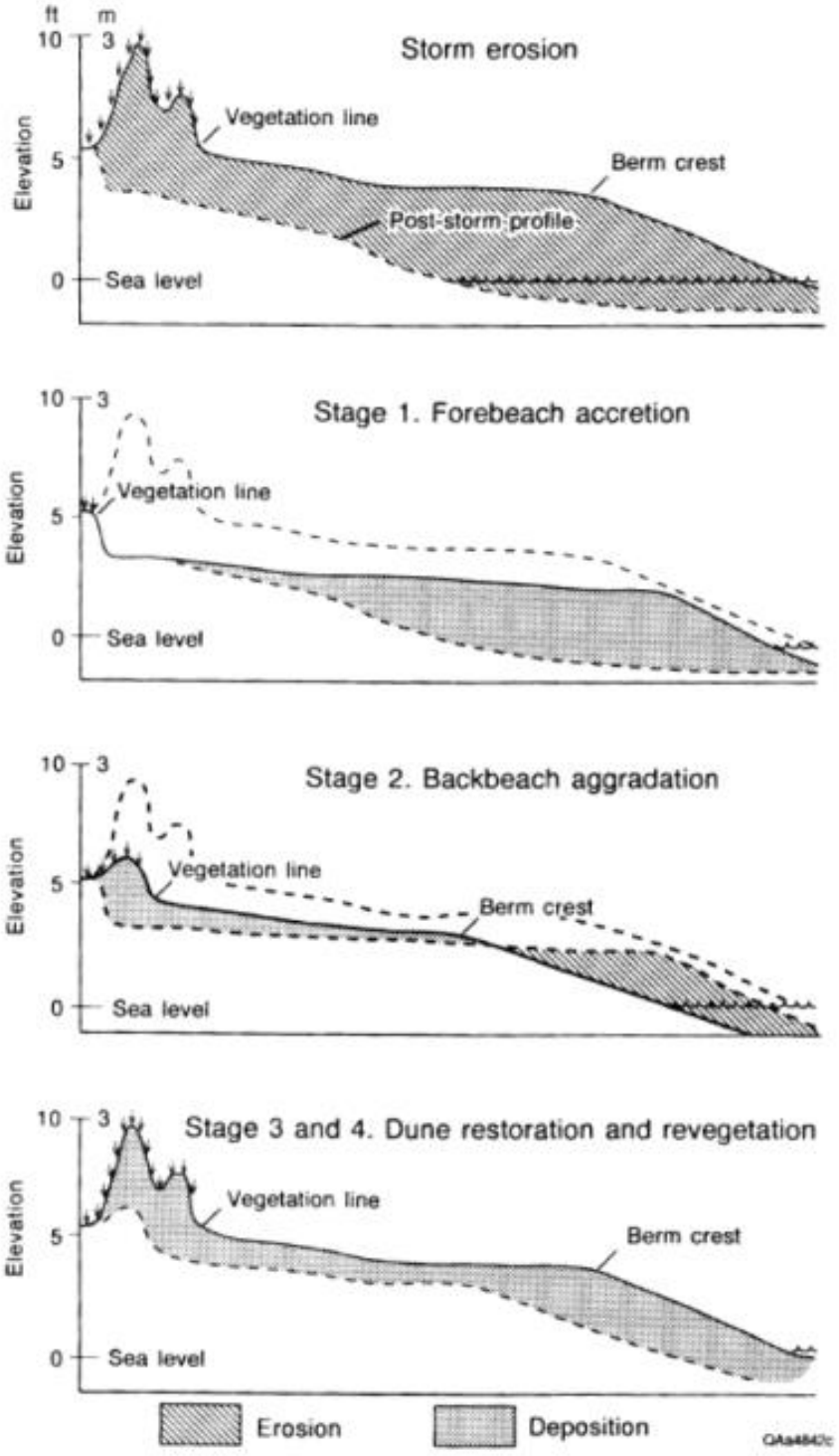

Figure 1.2: Stages of beach and foredune recovery [29].

It was found that this recovery process occurred over an average of four to five years, with total volume of recovered sediment ranging from 7% to 100%. The maximum cumulative recovered sediment volume occurred after four years with 67% of the initial sediment loss having been recovered (12% in the barrier flat as washover deposits and 55% recovered to the beach and foredune system).

The Upper Texas Coast (UTC) is tentatively defined as the coastal region between the Sabine Pass and the Brazos River [1]. On average, approximately four hurricanes and four tropical cyclones make landfall per decade [38]. Since the long term morphology of barrier islands is strongly influenced by the frequency of large scale episodic events, the UTC is particularly vulnerable to large scale erosion.

As the topic of this thesis the impact of Hurricane Ike on Follett's Island, a sediment-starved barrier island on the UTC, is studied. This study first outlines the collection of available hydrographic, atmospheric, aerial and survey data and provides an analysis of these data to characterize the long term metocean and geomorphologic state of the island. Particular attention is paid to the immediate response of the island to Hurricane Ike and the subsequent recovery period based on LiDAR data. The analysis of these LiDAR data will help determine how the hurricane impacted the sediment volume on the subaerial beach and foredune. Finally, numerical modeling tools XBeach and CSHORE are employed to numerically reproduce the observed effects of the hurricane on Follett's Island. The ultimate goal of the numerical modeling is to show a real time response of the island during the passing of the storm, rather than before and after snapshots provided by LiDAR data. This can help us better understand the hydrodynamic and morphodynamic processes inherent to barrier island overwash. If the models are accurate, they could be used for modeling the hypothetical coastal response from synthetic storms or for testing the efficacy of proposed coastal protection projects.

The goals of this study are to address the following questions:

1) How did Hurricane Ike affect the sediment volume on the subaerial beach and foredune of Follett's Island?
2) What was the driving mechanism behind the recovery of the subaerial island following the hurricane?
3) What hydrodynamic processes were most significant to the morphological response of Follett's Island during the hurricane?

1.1. Follett's Island

The UTC is characterized by long, narrow barrier islands comprised of fine sand (less than 0.2 mm), and a microtidal wave-dominated hydrodynamic environment with a tidal range of 0.54 m between Mean-Lower-Low-Water (MLLW) and Mean-Higher-High-Water (MHHW) (see Table 2.2 for tidal datum reference) [29][24]. FI is one of the most vulnerable stretches of the UTC due to its narrow width and high background erosion rates. The island is 25 km long, low-lying (-0.14 m – 2.06 m NAVD88), ranges between only 0.23 - 0.45 km in width and contains a series of beach communities, including Treasure Island and Surfside. FI also protects important economic and ecological assets like Christmas Bay, the Brazoria National Wildlife Refuge, the Bluewater Highway (CR-257), the Gulf Intracoastal Waterway (GIWW), and parts of the port of Freeport including the Naval Petroleum Reserve and a liquefied natural gas (LNG) de-liquification plant (Figure 1.3).

Freeport is also the original location of the mouth of the Brazos River, the 11th largest river in the U.S. [15]. Before 1881 the mouth of the Brazos River was natural with a small subaerial delta on the west flank and a shallow channel extending slightly eastward into the gulf. Until 1881, the Brazos River was the primary source of sediment for FI. Construction of the Freeport Jetties in 1881 lead to rapid accretion on the west side of the jetties and moderate accretion on the east side, indicating a net westward sediment transport [24].

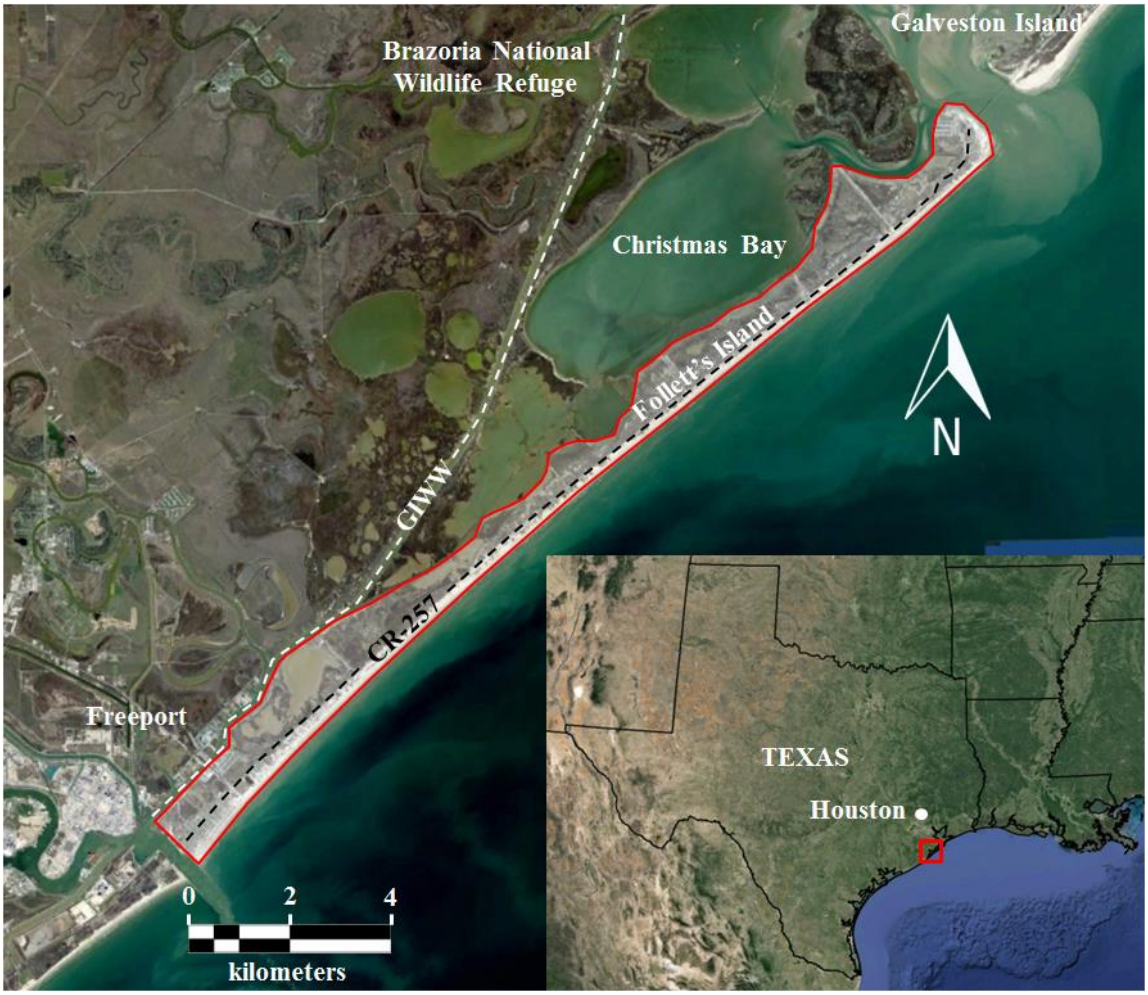

Figure 1.3: Follett's Island area map showing important economic assets such as the Port of Freeport and the Gulf Intracoastal Waterway (GIWW), and the CR-257 highway as well as ecological assets like Christmas Bay and the Brazoria National Wildlife Refuge.

FI is currently classified as a sediment-starved barrier island; a diversion channel was constructed in 1929, rerouting the Brazos River 6.5 miles west of the Freeport jetties, thus removing the islands primary sediment supply. This rerouting of the Brazos River sparked rapid formation of a new delta at the new location, which reached its maximum volume by 1948. The rapid formation of the new delta was accompanied by erosion of the accretionary fillets on both sides of the Freeport jetties. After 1948,

reduced flow in the Brazos River resulting from heavy upstream dam construction began to take its toll on the new delta. With an estimated one-third of the river's pre-1940 sediment supply, the new Brazos River delta began receding after 1948 [40].

On the east end of FI, the San Luis Pass separates Galveston and Follett's islands, connecting the Gulf of Mexico to the West Bay, Chocolate Bay, Bastrop Bay, and Christmas Bay. Before 1867, San Luis Island and Follett's Island were separated by the Cold Pass, which connected Christmas Bay directly to the Gulf of Mexico. However, by 1933 Follett's Island had merged with San Luis Island, rerouting the Cold Pass to the north between San Luis Island and Mud Island [24][28]. The San Luis Pass is characterized by a dominant flood tidal delta with a smaller ebb tidal delta. Between 1853 and 1933, the ebb tidal delta increased in volume by approximately 48,000 cubic meters per year [24]. Both the flood and ebb tidal deltas exhibit long-term increases in sediment volume, mostly due to large-scale episodic events such as hurricanes.

Morton and Pieper (1975) documented the shoreline changes in the vicinity of the Brazos River Delta by compiling shoreline and vegetation line positions from coastal charts, topographic maps, and aerial photographs. Both short-term and long-term trends were identified over the 122-year period of study from 1852 to 1974. It was found that the average net erosion east of the old Brazos delta along Follett's Island was 234 meters (approximately 1.9 meters per year), with a maximum net erosion of 403 meters (3.3 meters per year) at the San Luis Pass. Morton and Pieper (1975) asserted that the major factors affecting shoreline changes along the Texas Coast are a deficit in sediment supply and relative sea-level rise [28].

Paine et al. (2012) studied the historical shoreline change of the Texas Gulf Coast through 2007 by analyzing shoreline positions from nautical charts, topographic charts and aerial photographs. Long-term shoreline erosion rates on Follett's Island ranged between -4.5 m/yr. at the mouth of the San Luis Pass to stable at the center of the island (Figure 1.4). Over half of Follett's Island displays long term erosion rates in excess of the state average 1.24 m/yr [32].

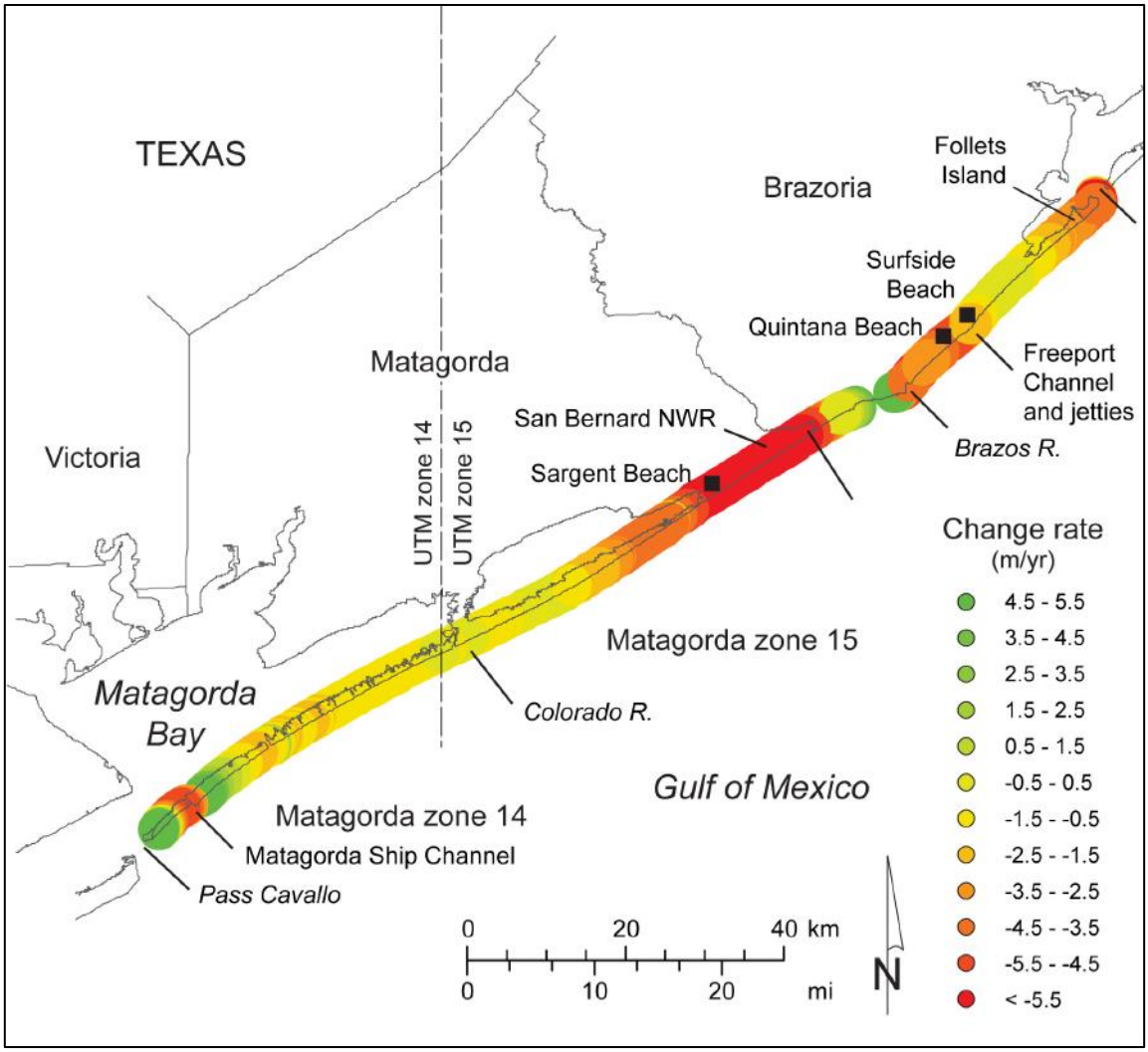

Figure 1.4: Long-term shoreline erosion rates through 2007 with Follett's Island depicted in the upper-right corner [31].

1.2. Hurricane Ike

In late August, 2008, Hurricane Ike (Ike) developed from a tropical depression off the west coast of Africa. The storm moved west across the Atlantic Ocean, reaching the status of "Major Hurricane" before making landfall on the island of Cuba and turning northwest to the Gulf of Mexico (Figure 1.5). In early September 2008 Hurricane Ike

crossed the Gulf of Mexico making landfall on Galveston Island, 40 km northeast of FI at 7:10 a.m. Greenwich Mean Time (GMT) on September 13, 2008 as a Category 2 hurricane with landfalling wind speeds of 49 m/s [2]. Wave heights as large as 16 meters were reported in the Gulf of Mexico during the passage of the hurricane. Ike is to date one of the costliest hurricanes ever recorded, with reported damages in excess of $12.5 billion in Texas, Louisiana and Arkansas. In addition to property damage in these three states, 21 people were killed as a direct result of the hurricane with an additional 64 indirect deaths due to factors like electrocution, carbon monoxide poisoning, etc. [2].

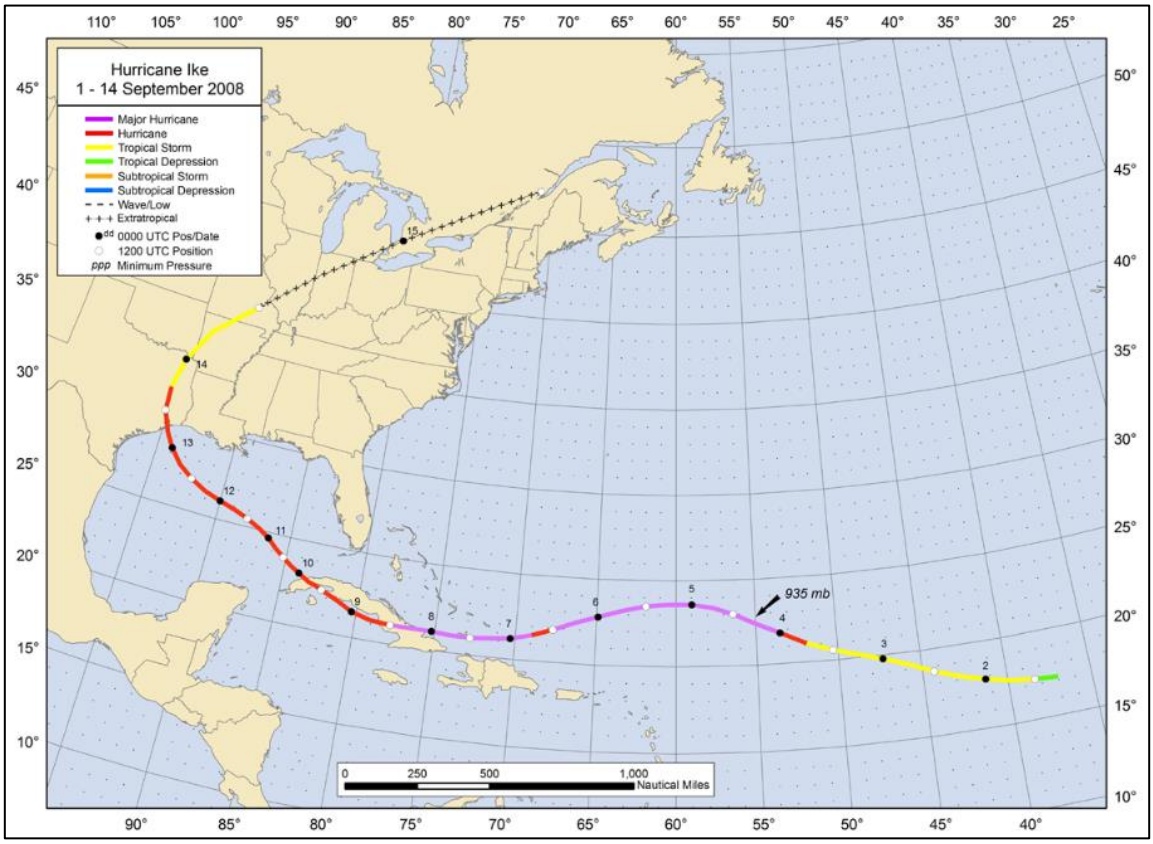

Figure 1.5: Hurricane Ike storm track [2].

Storm surge at FI reached a peak elevation of 2.6 m NAVD88, or 2.5 m MLLW (relevant tidal datums are outlined in Table 2.2). This peak was preceded by a forerunner surge of about 1 m beginning approximately 18 hours before landfall, after which the water level steadily rose to 2.2 m NAVD88 over the next 12 hours. This forerunner surge has been attributed to Ekman setup on the wide and shallow Louisiana-Texas (LATEX) shelf [18]. To the east of landfall, the forerunner appeared to be primarily a forced Ekman setup response, while west of landfall the forerunner was resultant of a freely propagating non-dispersive shelf wave traveling westward along the LATEX coast at a speed of approximately 5-6 m/s with an amplitude exceeding 1 meter. This phenomenon has been observed on the LATEX coast during other historical hurricanes including the 1900 and 1915 Galveston Hurricanes and is characteristic of slow moving storms with large wind fields over a wide and shallow continental shelf.

The forerunner surge flooded Christmas Bay and the back barrier region well before Ike made landfall. Waves offshore of FI exceeded 4.5 m significant wave height at 16 second peak period. After landfall, the water level quickly dropped to 2 m NAVD88 over the course of 12 hours. The amount of inland flooding from both the forerunner and the peak surge resulted in a strong ebb flow that scoured large channels in FI as the water dragged sediment out to the Gulf.

FI was breached in over 75 places by Ike, resulting in major damage and severe changes to the island morphology (See Figure 1.6 and Figure 1.7). In a few areas, historical inlets and channels visible in early aerial imagery were reactivated during the storm (Figure 1.8).

Figure 1.6: Damage to east end of Follett's Island from Hurricane Ike [7]. Arrow indicates reference point for comparing pre- and post-storm images.

Figure 1.7: Damage to west end of Follett's Island from Hurricane Ike [7]. Arrow indicates reference point for comparing pre- and post-storm images.

Figure 1.8: Aerial imagery from 1944 (left column), pre-Ike 2008 (center column), and post-Ike 2008 (right column) showing the reactivation of a historical flood delta (top row) and of the Cold Pass (bottom row) after Hurricane Ike.

Morton et al. (1995) studied the impact of storms on the subaerial sand distribution and associated shoreline migration for southwestern Galveston Island and northeastern Follett's Island, separated by the San Luis Pass [30]. The goal of the study was to analyze the post-storm erosion and deposition patterns, evaluate the efficiency of sand bypassing of the San Luis Pass, and to relate the post-storm beach recovery process to historical trends and changes in sediment supply. It was found that sand eroded from Galveston Island (the updrift barrier), was deposited in a sand flat at the end of the island, while sand accreted at Follett's Island (the downdrift barrier) was derived from the ebb-tidal delta of the San Luis Pass [30]. Thus, sand bypassing of the San Luis Pass

is episodic, event-driven and inefficient as sand is retained in the ebb-tidal delta until sufficiently large storm occurs to mobilize the delta, depositing some of the sediment on Follett's Island. Thus hurricanes are of critical importance to the sediment budget of Follett's Island.

2. DATA COLLECTION AND ANALYSIS

One of the greatest challenges of studying FI, is the modicum of available historical data; particularly bathymetric data. A comprehensive set of available physical data relevant to the morphological history of FI was compiled in this study. These data arise from scouring online data archives from organizations like the National Oceanographic and Atmospheric Administration (NOAA), The United States Geological Survey (USGS), and the Texas Natural Resources Information System (TNRIS) as well as from direct correspondence with the Texas General Land Office (GLO). An overview of available data is shown in Figure 2.1.

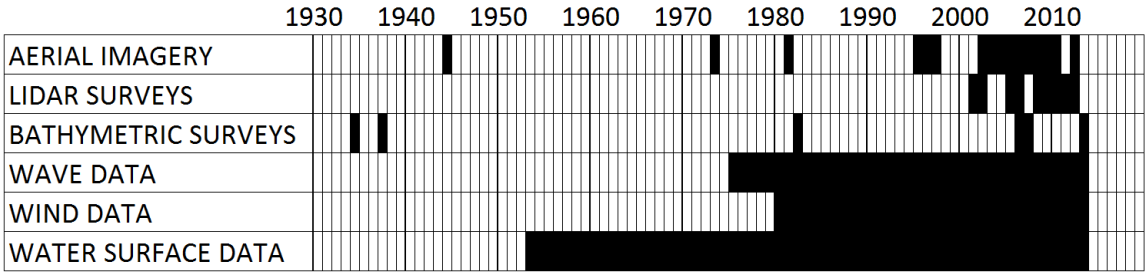

Figure 2.1: Overview of available historical data for Follett's Island. Black fields indicate availability.

The commercial computer program Surface-water Modeling Software (SMS) by Aquaveo was used to manage surface data (such as bathymetric, topographic, and LiDAR surveys), aerial imagery, and numerical modeling setup and analysis. This program was specifically designed for building and executing surface water models, and has built-in utilities for creating, triangulating and modifying elevation scattersets, creating unstructured meshes and rectilinear grids, managing spatial coordinates and datums, setting up common numerical models, and visualizing model results.

2.1. Metocean Data

Historical metocean data were collected from available gauges nearby FI. Analyses were performed on these data to characterize the metocean climate. A map outlining the recording stations for these data is provided in Figure 2.2, and the stations are outlined in Table 2.1.

Figure 2.2: Locations of relevant metocean data stations near Follett's Island.

Table 2.1: Station information for relevant metocean stations.

Station Name	Source	Data Type	Data Range
Freeport 8772440	CO-OPS	water levels	1954 - 2008
NDBC 42035	NDBC	wind & wave	1993 - 2014
NDBC 42019	NDBC	Wind & wave	1990 - 2014
USGS ike_SSS-TX-GAL-015	USGS	water levels	Sep. 10-19, 2008
Kennedy Gauge W	Kennedy [16]	wave	Sep. 5-25, 2008

2.1.1. Water Levels

Tidal datums in the Freeport channel were extracted using the NOAA software tool VDatum, and were related to the vertical control datum NAVD88 [34]. These tidal datums are summarized in Table 2.2.

Table 2.2: Tidal datums at Follett's Island showing a tidal range of 0.54 m.

Datum	Elevation [m NAVD88]
MHHW	0.40
NAVD88	0.00
MLW	-0.06
MLLW	-0.14

Historical water levels were evaluated at the Center for Operational Oceanographic Products and Services (CO-OPS) tidal station 872440, located on the Freeport channel near the Dow Chemical plant. This station recorded hourly water levels between 1954 and 2008. Extremal analysis was performed on these data by NOAA [47]. The data were first de-trended from a long-term annual rise of the mean sea level (MSL) of 4.35 mm/yr. at this station. The annual maxima were then fit to the Generalized Extreme Value (GEV) probability distribution function, which is the most appropriate distribution for block maxima and minima data.

Table 2.3 shows the return period water levels for Follett's Island and Figure 2.3 shows the data fit to the GEV distribution. Based on these data, high water levels associated with Hurricane Ike exceeded 100 year water levels at Follett's Island.

Table 2.3: Return period water levels at CO-OPS tidal station 872440 corrected for long-term rise in mean sea level.

Return Period [yrs.]	High [m MHHW]	Low [m MLLW]
2	0.60	-0.65
5	0.80	-0.80
10	1.00	-0.85
25	1.10	-0.95
50	1.30	-1.05
100	1.50	-1.15

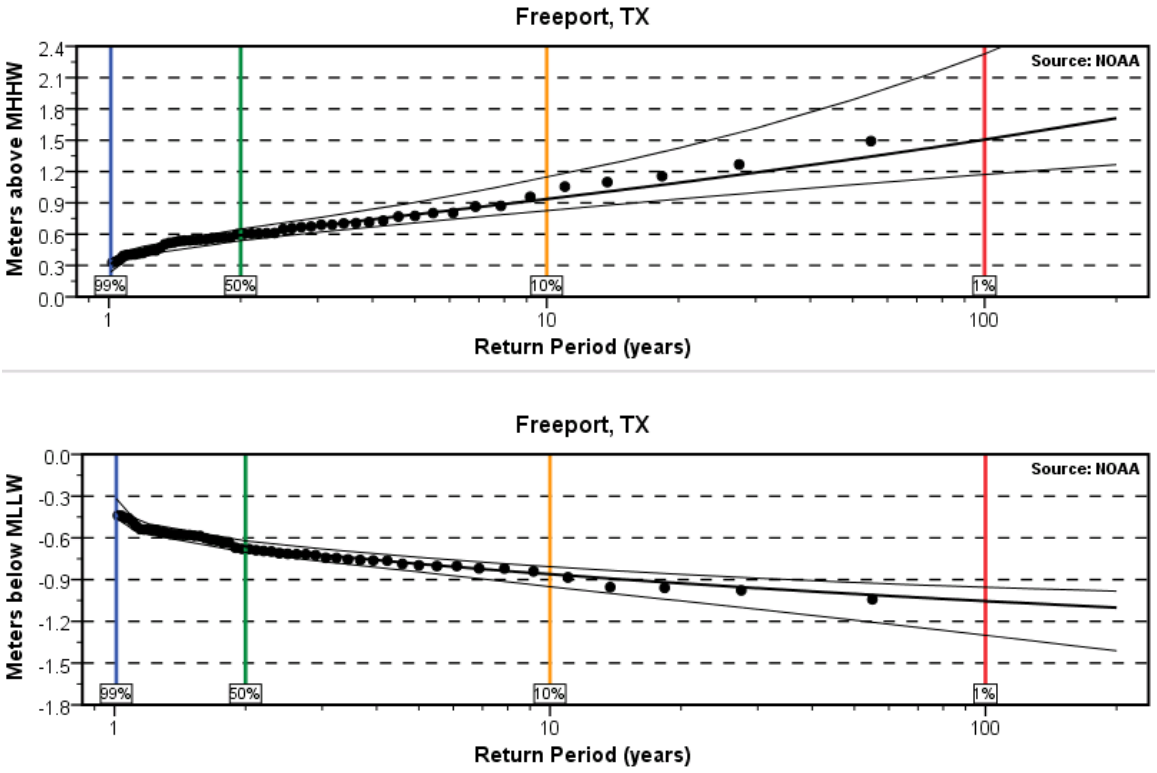

Figure 2.3: Extreme high and low water level data at FI fit to the GEV probability distribution [47].

2.1.2. Long-Term Waves

There are no NDBC stations in the immediate vicinity of FI, but there are two stations close enough to be used for extreme wave analysis. Station 42019 is located directly south of FI approximately 93 km offshore in 83 m water depth. This station has a record of hourly significant wave heights and dominant wave periods between 1990 and 2014, with accompanying mean wave directions after 1997. Station 42035 is located northeast of FI approximately 28 km offshore in 12 m water depth. This station has a record of hourly significant wave heights and dominant wave periods between 1993 and 2014, with accompanying mean wave directions after 1998. Maximum significant wave heights recorded at stations 42019 and 42035 were 6.31 m and 5.95 m at respectively.

For each station, an extremal analysis was performed on the data. Null values were filtered out, and a peak-over-threshold operation was performed on the remaining data [9]. For Station 42019, the threshold significant wave height was 4.0 meters and for Station 42035, the threshold was 3.0 meters. To make sure that multiple peaks were not captured within a single storm, peaks were filtered such that only one peak could be recorded within a 36-hour storm window. These peaks were then ranked in descending order and the sorted data were statistically fitted to a Weibull distribution and Fisher-Tippett types I & II (2.1).

$$\hat{F}_{(m)} = 1 - \frac{m - \alpha}{N_T + \beta}, \;\; m = 1,2, \dots, N \tag{2.1}$$

where N *is* the censored sample size, N_T is the total number of samples, and m represents the order of the variate in the population. In the case of uncensored samples, N and N_T are the same. The constants α and β are defined in Table 2.4.

Table 2.4: Constants associated with Weibull, FT-II, and FT-I distributions.

Distribution	α	β
Weibull	$0.20 + 0.27/\sqrt{k}$	$0.20 + 0.23/\sqrt{k}$
FT-II	$0.44 + 0.52/k$	$0.12 + 0.11/k$
FT-I	0.44	0.12

To determine the most appropriate fit, the least squares method was used by calculating the sample correlation coefficient for each distribution and k-value. The most appropriate distribution for each gauge was that whose sample correlation coefficient had an absolute value closest to 1 [9]. This involved varying shape factor parameters in the Weibull distribution, which was done using discrete values between 0.5 and 2.0 with a tolerance of 0.01. Although the Coastal Engineering Manual recommends not extrapolating beyond three times the available data range for design (in this case 63 years), the extreme values in this context are meant only to characterize the metocean environment of FI. Thus extreme values beyond the 63 year return period in this case should not be used for design [44]. Figure 2.4 and Figure 2.5 show the distribution fit for these data.

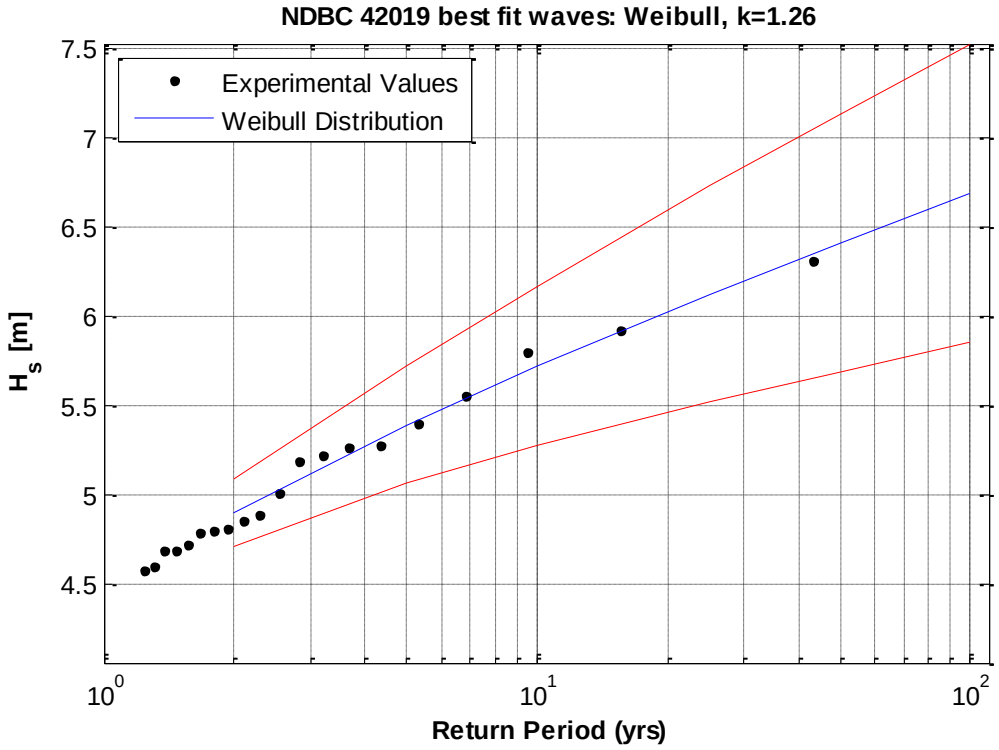

Figure 2.4: Omni-directional return period for significant wave heights at NDBC station 42019. Optimal distribution is Weibull with k-value of 1.26. Red lines signify 90% confidence intervals.

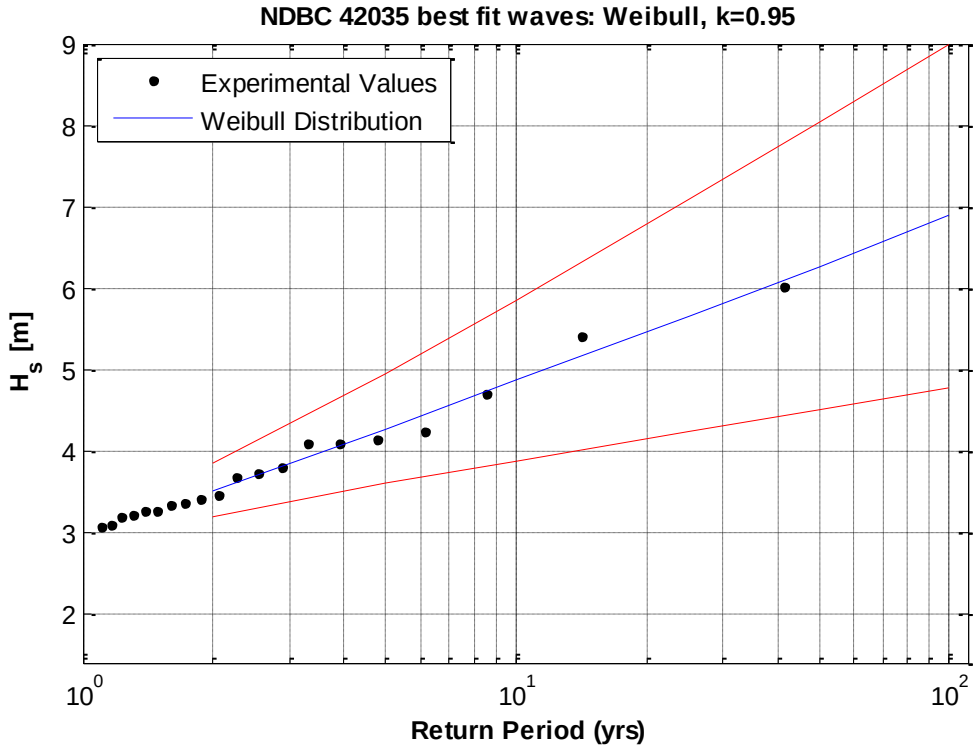

Figure 2.5: Omni-directional return period for significant wave heights at NDBC station 42035. Optimal distribution is Weibull with k-value of 0.95. Red lines signify 90% confidence intervals.

For both samples, the Weibull distribution created a best fit. For Station 42019, the best-fit shape factor value was k=0.95, and for Station 42035 the best fit shape factor value was k=1.26. Table 2.5 summarizes the return periods and associated significant wave heights between 2 year and 100 year return periods. Based on these data, significant wave heights associated with Hurricane Ike correspond to the 40 year return period conditions.

Table 2.5: Return period significant wave heights at NDBC Stations 42019 and 42035.

Return Period [yrs.]	NDBC 42019 [m]	NDBC 42035 [m]
2	4.89	3.52
5	5.39	4.27
10	5.72	4.86
25	6.13	5.66
50	6.42	6.27
100	6.69	6.88

Wave roses comprising the directional distribution of significant wave heights were also developed from NDBC Station data. Figure 2.6 and Figure 2.7 show the wave roses from NDBC Stations 42019 and 42035 respectively. From these it is clear that prevailing wave directions are from SSE and SE, resulting in a dominant westward flow of sediment (also observed by Mason et al., 1981 [24] and Wallace et al., 2010 [45]).

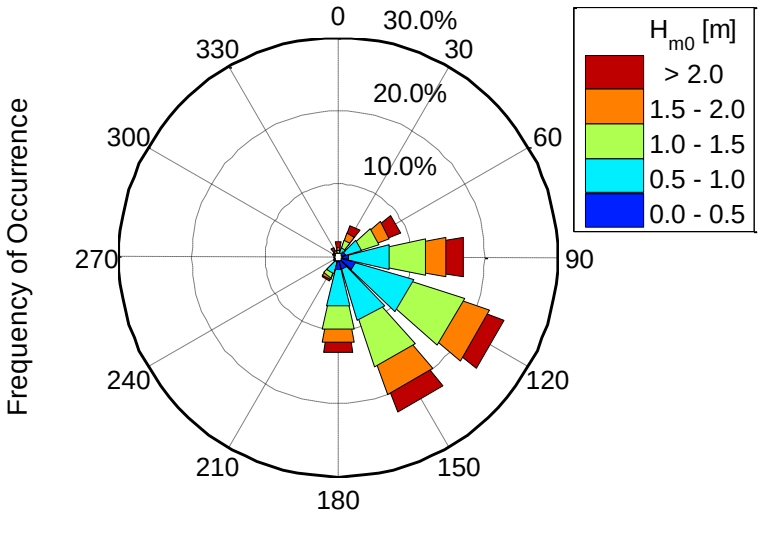

Figure 2.6: Wave rose showing the directional distribution of significant wave height at NDBC Station 42019.

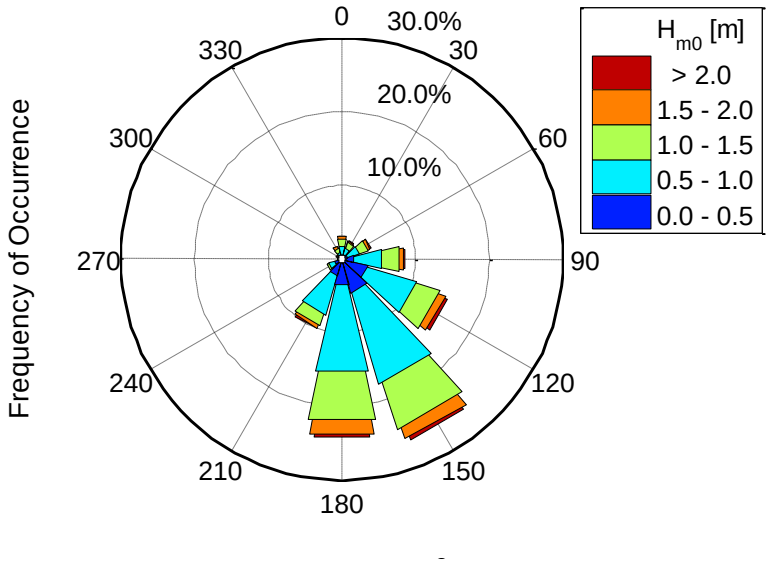

Figure 2.7: Wave rose showing the directional distribution of significant wave height at NDBC Station 42035.

2.1.3. Long-Term Winds

Data NDBC Stations 42019 and 42035 were used to analyze omni-directional extreme winds using the same method as for waves. Figure 2.8 and Figure 2.9 show the results of the extremal wind analysis for NDBC Stations 42019 and 42035 respectively.

For both samples, the Weibull distribution created a best fit. For Station 42019, the best-fit shape factor value was k=0.73, and for Station 42035 the best-fit shape factor value was k=0.66. Table 2.6 summarizes the return period wind speeds between 2 year and 100 year return periods. Maximum wind speeds recorded at stations 42019 and 42035 during Ike were 28.4 m/s and 27.9 m/s respectively. Based on these data, return period significant wave heights associated with Hurricane Ike correspond to between 20 and 35 year wind speeds.

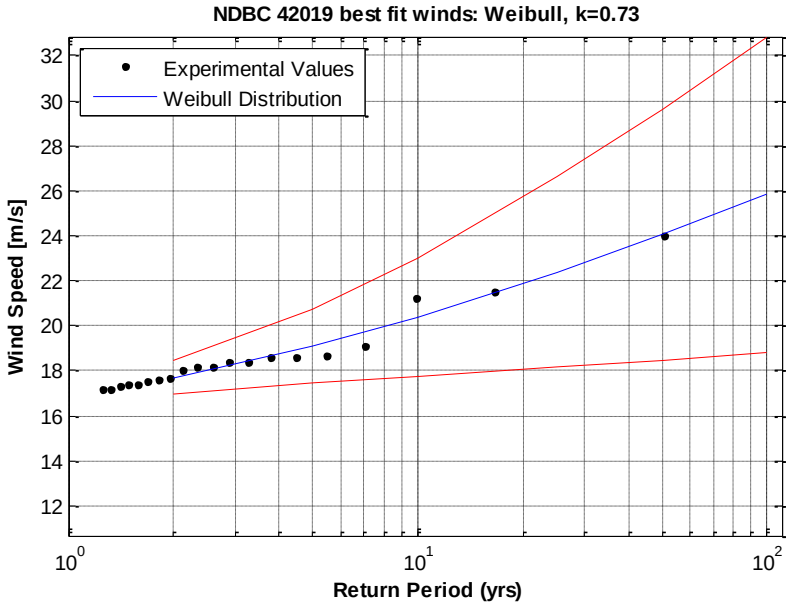

Figure 2.8: Extreme wind speed and corresponding return period at NDBC 42019. Optimal distribution is Weibull with k=0.73. Red lines signify 90% confidence intervals.

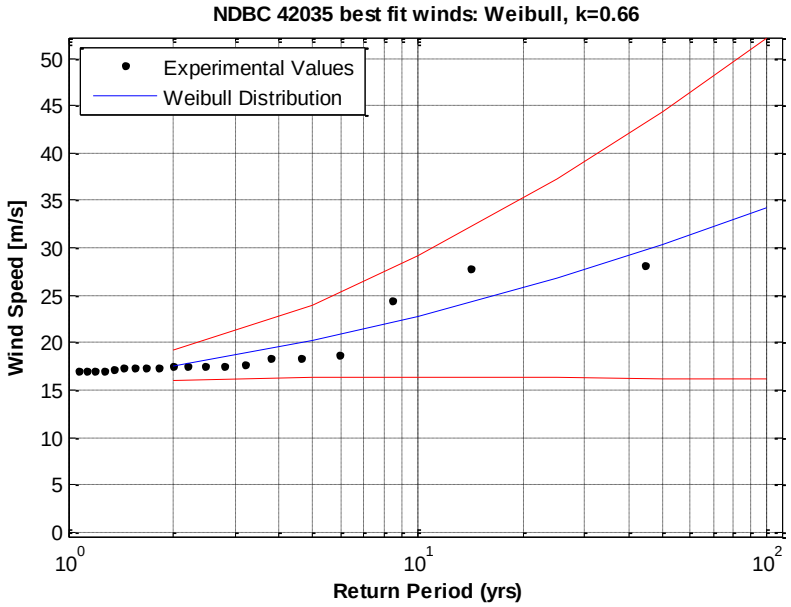

Figure 2.9: Extreme wind speed and associated return period at NDBC 42035. Optimal distribution is Weibull with k= 0.66. Red lines signify 90% confidence intervals.

Table 2.6: Return period wind speeds at NDBC Stations 42019 and 42035.

Return Period [yrs.]	NDBC 42019 [m/s]	NDBC 42035 [m/s]
2	17.71	17.57
5	19.08	20.15
10	20.39	22.73
25	22.37	26.81
50	24.04	30.33
100	25.82	34.20

Wind roses comprising the directional distribution of wind speeds were also developed from NDBC Station data. Figure 2.10 and Figure 2.11 show the wind roses from NDBC Stations 42019 and 42035 respectively. From these it is clear that prevailing wave directions are from SSE and SE.

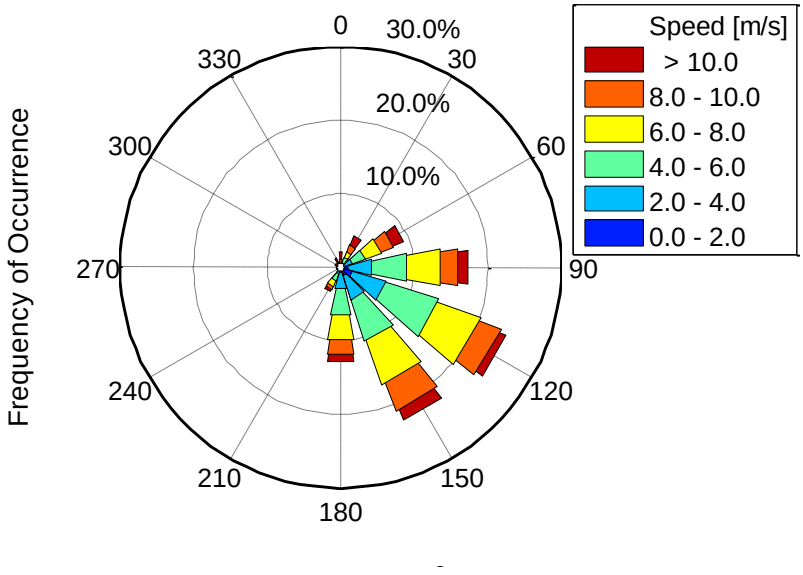

Figure 2.10: Wind rose showing the directional distribution of wind speed at NDBC Station 42019.

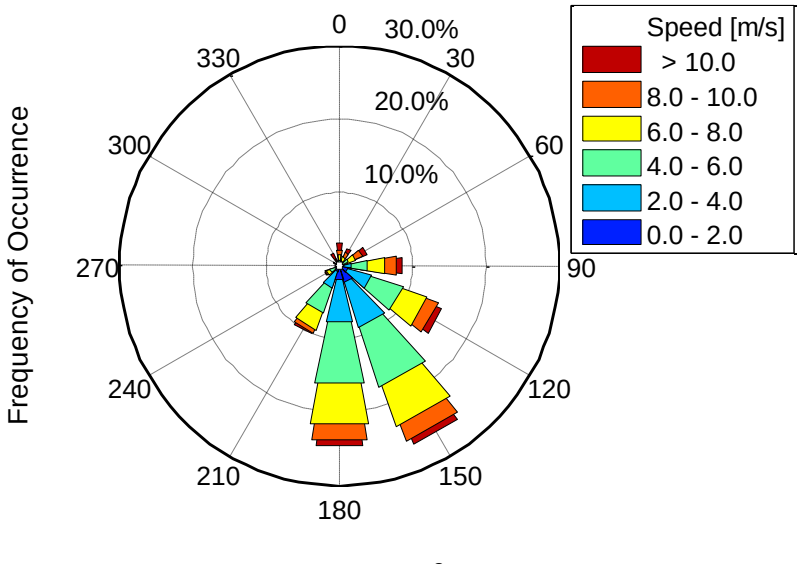

Figure 2.11: Wind rose showing the directional distribution of wind speed at NDBC Station 42035.

Although the winds from SSW and SW occur more frequently, a greater percentage of strong winds (>10 m/s) are from the north, representing frequent cold fronts that annually pass through the area during winter months (Nov – Apr). On average, there are 46 cold fronts per year that pass through the northern Gulf of Mexico [12]. Cold fronts occur at 3-10 day intervals in a given year and are characterized by a pre-frontal phase of high-energy southeasterly winds for 1 to 2 days, followed by a 12 to 24 hour period of strong northwesterly to northeasterly winds following the passage of the front. Along Galveston Bay, including Christmas Bay, water levels in the bay can be lowered by as much as 1.5 m during the passage of a severe cold front and typically are lowered by at least 0.5 m. These cold fronts play a critical role in the recovery of barrier islands after a storm by directing aeolian transport of washover sediments back towards the beach and foredune system. This bay-to-beach directed transport can help create an elevated backbeach that ultimately nourishes new dune system [29]. For back bays of significant size, such as Christmas Bay, cold fronts can also cause erosion of the bayside beach from locally generated northerly waves [42].

2.1.4. Short-Term Metocean

A temporary monitoring network of pressure transducers was deployed by the USGS at 65 locations on the Gulf Coast [8]. One of these instruments, SSS-TX-GAL-015 was positioned at the San Luis Pass and provided a time series of surge elevation and barometric pressure near FI. Kennedy et al. (2011) deployed temporary wave gauges in nine locations off of the Texas coast in 8-16 m water depth to record wave data during Ike [17]. Gauges W and V, positioned at the eastern and western ends of FI respectively, provide time series of significant wave height, peak period and mean water level offshore of FI during the storm. Figure 2.12 shows time series of WSEL (SSS-TX-GAL-015), H_s, and T_p (Kennedy gauge W).

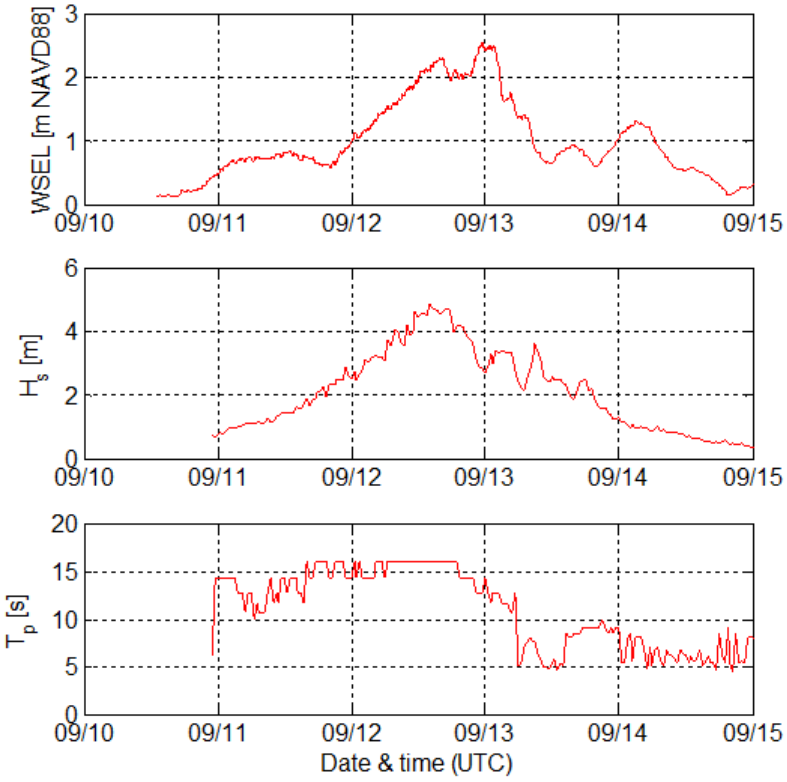

Figure 2.12: Time series of WSEL (top), H_s (middle), and T_p (bottom) from Sept. 10-18, 2008 showing Hurricane Ike as it makes landfall.

2.2. Bathymetric Surveys

Bathymetric surveys in the vicinity of Follett's Island dating back to 1934 were collected. Surveys differ in coverage area and resolution.

Table 2.7: List of publicly available bathymetric data in the vicinity of Follett's Island.

Year	Source	Type	Resolution [m]
1934	DoC[1]	H-Surv[2]	50 - 200
1937	DoC	H-Surv	300 - 600
1982	DoC	H-Surv	50 - 200
2007	TerraSond	Transects	Cross-shore: 1 m Long-shore: 1000 m
2013	TAMU[3]	Transects	Cross-shore: 1 m Long-shore: 1000 m

[1]Department of Commerce
[2]Hydrographic Survey
[3]Texas A&M University

Unfortunately, very few surveys were available, most of which were single beam surveys prior to 1982. The DoC hydrographic survey from 1934 was the only survey that covered the bay side of FI. Luckily, the two surveys from 2007 and 2013 offer profile elevations along the same cross-shore transects one year before and five years after Hurricane Ike. The survey from 2013 also includes a subaerial extension of the transects from the shoreline to highway CR-257, which runs landward of the foredune along the entire length of the island.

2.3. LiDAR Surveys

LiDAR surveys dating back to 2006 that cover all or part of Follett's Island were collected. A list of these surveys is provided in Table 2.8. Note that the Apr. 2006 survey was based on the first return signal while the other surveys were based on the second

return signal. In this coastal setting, the first return signal includes buildings and dense foliage while the second return signal records only ground elevation with buildings and dense foliage filtered out. This must be regarded when comparing any of the post-Ike surveys with the 2006 pre-Ike survey.

Table 2.8: List of publicly available LiDAR data covering all or part of Follett's Island. Return refers to the LiDAR return signal for filtering features.

Date	Source	Type	Resolution [m]	Return
Apr. 2006	TWDB	point cloud	1.4	1
Dec. 2008	UT-BEG	raster	1	2
Feb. 2009	USACE	point cloud	0.7	2
Apr. 2010	UT-BEG	raster	1	2
Apr. 2011	UT-BEG	raster	1	2
Feb. 2012	UT-BEG	raster	1	2

To analyze the subaerial response of Follett's Island to Hurricane Ike, LiDAR surveys were compared for pre- and post-Ike conditions as well as for an approximately five year recovery period. Data were processed using SMS in the working coordinate system of UTM zone 15 relative to NAD83. The vertical units and datum for this analysis was meters relative to NAVD88.

2.3.1. April 2006 Survey

The 2006 LiDAR survey was ordered by the Texas Water Development Board in early 2006, and was carried out by Sandborn Mapping Company, Inc. between April 9, 2006 and May 13, 2006. Data were delivered as a point cloud with resolution of approximately two to three meters. The data were provided in geographic coordinates with vertical units of feet relative to NAVD88. Coordinates were re-projected to the working coordinate system and vertical units were converted to meters.

2.3.2. December 2008 Survey

The Post Ike 2008 survey was performed by the University of Texas Bureau of Economic Geology (UT-BEG) in December 2008, approximately three months after Hurricane Ike made landfall. An approximately 300 meter wide strip of the Upper Texas Coast was surveyed. Data were provided as a 1m resolution Digital Elevation Model (DEM) Raster in the UTM zone 15 coordinate system with elevation in meters relative to NAVD88. Elevations from the LiDAR second return, representing ground elevations, were used to develop the DEM. LiDAR elevations were compared with ground survey points (estimated vertical accuracy of 1-5 centimeters). Mean elevation differences between the LiDAR and ground elevations were used to estimate and remove an elevation bias from the LiDAR. The elevation bias generally ranged between -0.17m and 0.11m, with a root mean square (RMS) error of 0.058 for the second return values.

2.3.3. February 2009 Survey

The 2009 survey was ordered by the USACE Joint Airborne LiDAR Bathymetry Technical Center of Expertize (JALBTCX). Second return LiDAR data were provided as a point cloud in the geographic coordinate system with elevations in feet relative to NAVD88. The data were re-projected to UTM zone 15 coordinates and elevations were converted to meters.

The LiDAR survey was performed by 3001 International Inc. between February 3, 2009 and April 23, 2009. Accuracy was ensured by comparisons with ground control points also established by 3001, Inc. Automated filtering and manual editing was also performed by 3001, Inc. to ensure accuracy.

2.3.4. April 2010 Survey

The 2010 LiDAR survey was performed by the UT-BEG on April 8-9, 2010. An approximately 300-meter-wide strip of the Upper Texas Coast was surveyed as part of the Coastal Impact Assistance Program (CIAP). Data were provided as a 1m resolution DEM Raster in the UTM zone 15 coordinate system with elevation in meters relative to NAVD88. Elevations from the LiDAR second return, representing ground elevations,

were used to develop the DEM. LiDAR elevations were compared with ground survey points (estimated vertical accuracy of 1-5 centimeters). Mean elevation differences between the LiDAR and ground elevations were used to estimate and remove an elevation bias from the LiDAR. The elevation bias generally ranged between -0.08m and -0.11m, with a RMS error of 0.046 for the first return values.

2.3.5. April 2011 Survey

The 2010 LiDAR survey was performed by the UT-BEG on April 12-13, 2011. An approximately 300-meter-wide strip of the Upper Texas Coast was surveyed as part of the Coastal Impact Assistance Program (CIAP). Data were provided as a 1-m-resolution DEM Raster in the UTM zone 15 coordinate system with elevation in meters relative to NAVD88. Elevations from the LiDAR second return, representing ground elevations, were used to develop the DEM. LiDAR elevations were compared with ground survey points (estimated vertical accuracy of 1-5 centimeters). Mean elevation differences between the LiDAR and ground elevations were used to estimate and remove an elevation bias from the LiDAR. The elevation bias generally ranged between -0.13m and -0.17m, with a RMS error of 0.045 for the first return values.

2.3.6. February 2012 Survey

The 2010 LiDAR survey was performed by the UT-BEG on February 14-15, 2012. An approximately 300-meter-wide strip of the Upper Texas Coast was surveyed as part of the Coastal Impact Assistance Program (CIAP). Data were provided as a 1-m-resolution DEM Raster in the UTM zone 15 coordinate system with elevation in meters relative to NAVD88. Elevations from the LiDAR second return, representing ground elevations, were used to develop the DEM. LiDAR elevations were compared with ground survey points (estimated vertical accuracy of 1-5 centimeters). Mean elevation differences between the LiDAR and ground elevations were used to estimate and remove an elevation bias from the LiDAR. The elevation bias generally ranged between -0.07m and -0.14m, with a RMS error of 0.049 for the first return values.

2.3.7. Data Processing

Although four of the surveys were provided in raster format, all surveys were loaded into SMS as scatter data to simplify interpolation and data processing. For each survey, all sub-files were loaded simultaneously and automatically merged in SMS. Upon loading each scatterset, SMS automatically triangulated a surface. Since some of the boundary triangles represented large coverage areas where no data is present (e.g. at a concave boundary), these boundary triangles were selected and deleted. This was achieved by processing boundary triangles based on aspect ratio, and deleting all boundary triangles with an aspect ratio greater than five. In some cases, individual triangles had to be manually deleted when the aspect ratio filter did not adequately process the boundary triangles.

For analysis, SMS was used to linearly interpolate LiDAR surveys from different years onto one another and then subtract the elevations to determine the difference in the land surface between the two years. Since each LiDAR survey had a different coverage area, analysis was performed on only the overlapping area between surveys. This was achieved in SMS by setting the extrapolation option to a single value of -999 during the interpolation process. After interpolation, all points less than -998 were selected and deleted to remove the coverage with no overlapping values.

2.4. Aerial Imagery

Georeferenced aerial imagery showing all or part of Follett's Island was acquired from online data servers and personal correspondence with the Texas General Land Office (GLO). Although aerial imagery of FI is available as far back as 1944, the bulk of this imagery is available after 1995. These images have resolutions between 15 cm and 2 m. Table 2.9 outlines the gathered aerial imagery:

Table 2.9: List of publicly available aerial imagery covering all or part of Follett's Island.

Date	Source	Format	Resolution [m]
Apr. 1944	TxDAPA[1]	TIF	1.00
Sep. 1974	Google Earth	-	1.50
Jul.1982	Google Earth	-	1.50
Jan. 1995	USGS	TIF	1.00
2004	NAIP	JPG	2.00
Nov. 2005	NAIP	JPG	2.00
2006	NAIP	JPG	2.00
Sep. 2007	GLO	TIF	0.30
2008	NAIP	JPG	2.00
Sep. 2008[2]	GLO	TIF	0.15
Sep. 2008[3]	NOAA	JPG	0.35
2009	GLO	TIF	0.15
2010	NAIP	JPG	1.00
2012	NAIP	JPG	1.00

[1]Texas Digital Aerial Photo Archive [4]

Aerial Imagery was primarily used in support of topographic LiDAR data, particularly for analyzing the island pre- and post-Ike conditions and the island recovery after Ike. An attempt was made to use these aerial images to extract historical shoreline position based on the high water mark. However, this analysis proved inaccurate since multiple wet/dry boundaries with differing contrasts were visible along the beach in many cases. Despite the low tidal range, sometimes these boundaries were spaced more than 40 meters apart (Figure 2.13a). Some wet/dry boundaries were not continuous along the entire length of beach, and in tracing one boundary from east to west, that boundary might slowly fade away. Furthermore, colonies of Sargassum, a genus of seaweed

frequently making landfall on the Gulf Coast in summer months, often distorted the exact location of the wet/dry boundary and prevented swash from reaching its natural terminus (Figure 2.13b).

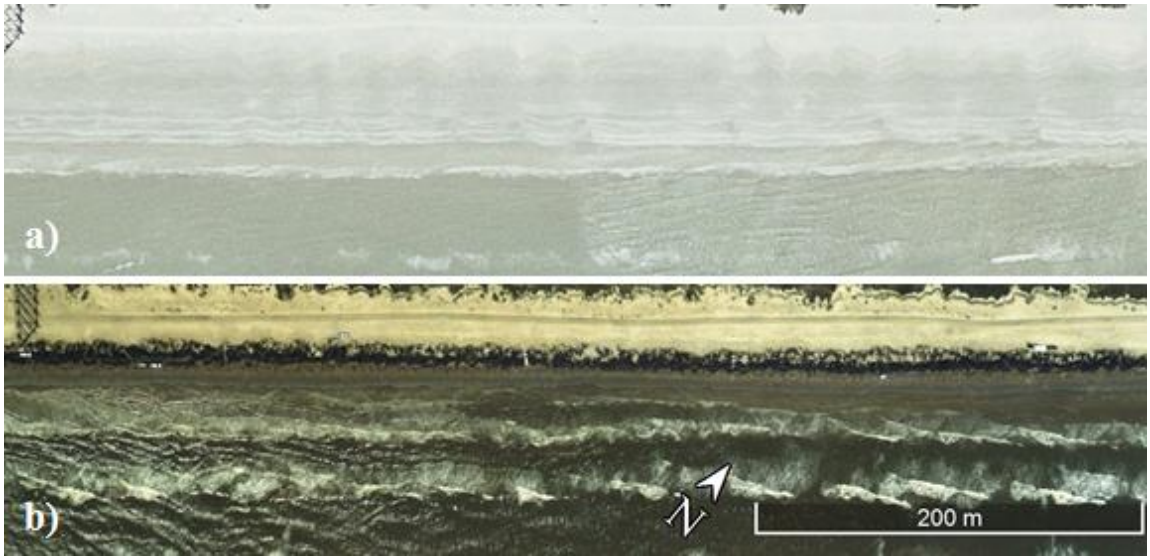

Figure 2.13: a) 500 m stretch of FI beach displaying multiple potential high-water lines. b) 500 m stretch of FI beach displaying mounds of Sargassum interfering with swash and distorting the high-water line.

Pajak and Leatherman (2002) studied the short-term variability of the high water line in Duck, North Carolina. They found that variations in day to day high water line can be significant on gently sloping beaches, as is the case on Follett's Island [33]. These variations are exacerbated by variations in wave climate and water level, and with the high frequency of winter cold fronts and summer storms in the area it is clear that the high water line is an inaccurate means of discerning shoreline in this area.

2.5. Analysis of Hurricane Ike on Follett's Island

Pre- and post-Ike LiDAR surveys were compared to identify patterns of erosion and deposition (Figure 2.14). It is clear from this figure that the foredune along the entire island was eroded by between 0.4 m and 1.5 m. There are two large back-barrier washover deposits on the east end of the island where the bed elevation was raised by approximately 0.5 m. Interestingly, these deposits are not observed at the middle of the island, despite similar erosion to the foredune.

This phenomenon could be related to the critical island width theory posed by Leatherman (1979) and discussed in the introduction [21]. The middle of the island is narrower than the east end, thus allowing washover sediments to reach the back bay rather than being deposited in the back barrier. This would effectively result in partial rollover of the island, where the center of the island migrates landward faster than the ends, causing the island to curve inward, a trend that is clearly observed from historical aerial imagery.

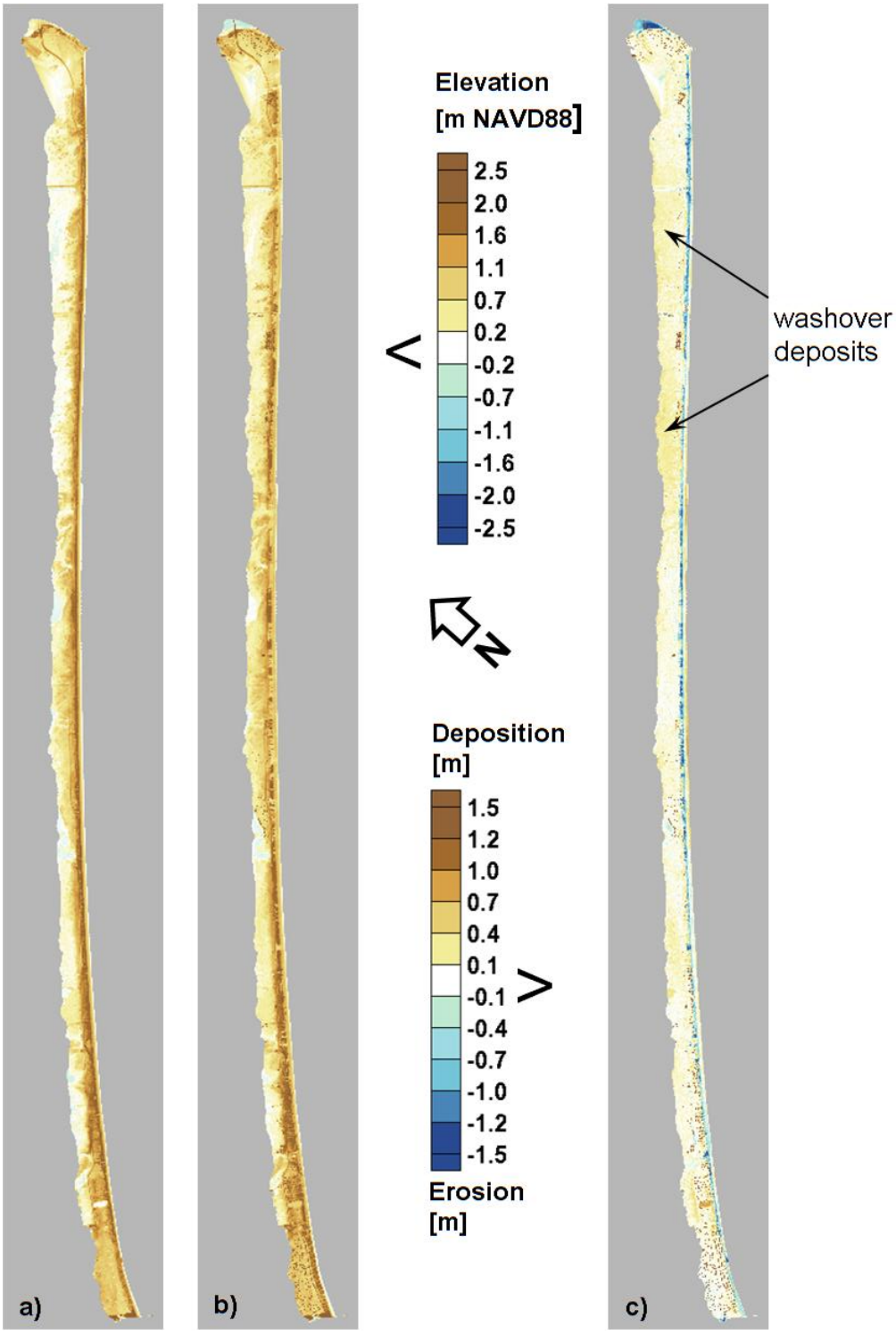

Figure 2.14: LiDAR measured bed elevation for pre-Ike conditions (a), for post-Ike conditions (b), and erosion-deposition plot based on these surveys (c).

To better observe the evolution of the subaerial dune and forebeach, land elevations derived from LiDAR surveys in 2006 and 2010 – 2012 were interpolated onto 8 cross-shore transects (Figure 2.15). These transects are spaced between 2 and 5 km along the length of FI and are aligned with single beam bathymetric profiles from surveys conducted in 2007 and 2013.

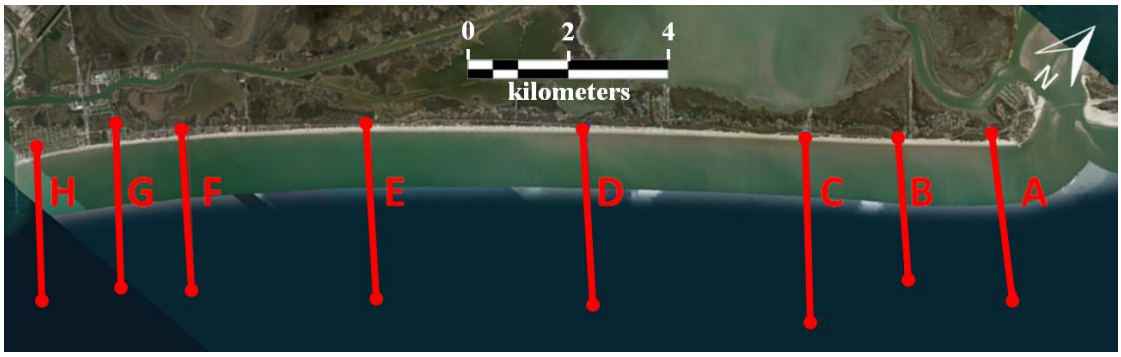

Figure 2.15: Cross-shore transects for analysis of island topography and bathymetry.

After Ike, the more densely populated west side of FI underwent a series of construction projects including a revetment construction and beach nourishment project. Thus, Sections F - H were excluded from this analysis as they do not reflect the island's natural recovery. The elevations from the combined 2006 LiDAR survey and 2007 bathymetric survey are assumed to represent the pre-Ike conditions. There was one smaller hurricane (Hurricane Humberto) that made landfall about 100 km east of FI in 2007, but the short life of this hurricane resulted in minimal impacts to the coast [3].

Figure 2.16 and Figure 2.17 show the profiles of the foredune and beach for Sections A and D respectively from the pre-storm conditions and for approximately five years of recovery after Ike. These are only partial profiles, which cover the beach and foredune from the shoreline to CR-257; they do not extend to the bay. These sections most clearly represent the post-storm morphology trends of the east end of the island (Sections A-C) and the center of the island (Sections D-E) respectively. Profiles from all sections are

provided in Appendix C. It is clear from these surveys that the original foredune was demolished by Ike, depositing sediment both in the back barrier during overwash and on the forebeach/offshore during return flow. This deposition on the forebeach acted to flatten the beach slope and extend the shoreline slightly seaward. Initial beach slopes range from 25H:1V to 50H:1V, while the post-Ike beach slope was universally around 55H:1V.

The first five months of recovery of the FI foredune and beach system are characterized by rapid accretion of the forebeach followed by backbeach aggradation (where a backbeach exists). By April 2010, the new foredune system had begun to form, and between 2010 and August 2013, the dunes increased in volume while the beach steepened slightly. This recovery process parallels that observed by Morton (1994) and can mainly be attributed to accumulation of aeolian sediment transport [29].

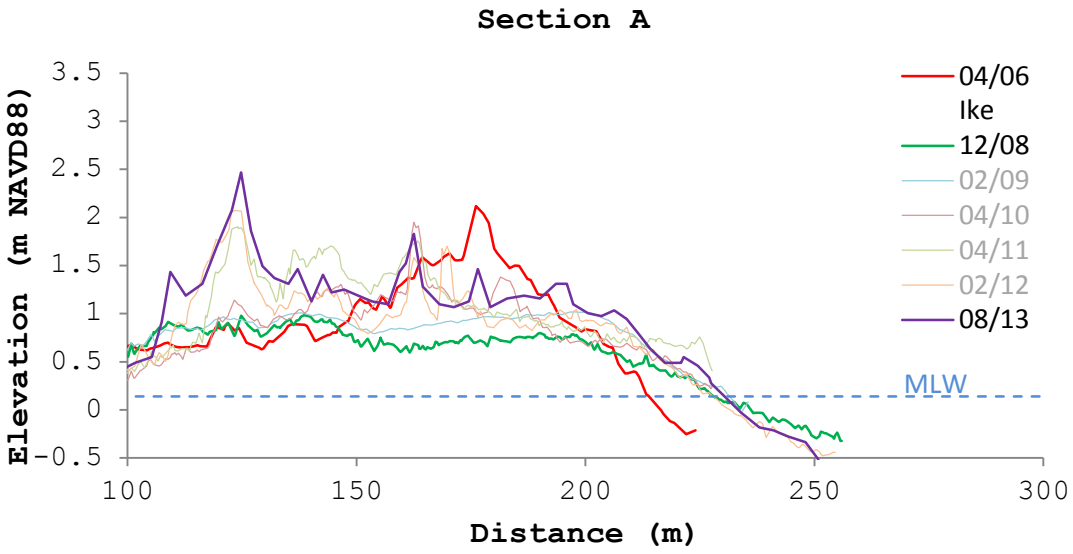

Figure 2.16: Elevation profiles documenting the impact of Hurricane Ike to the foredune and beach as well as the subsequent recovery period at Section A. Cross-shore distance is positive offshore with zero at CR-257.

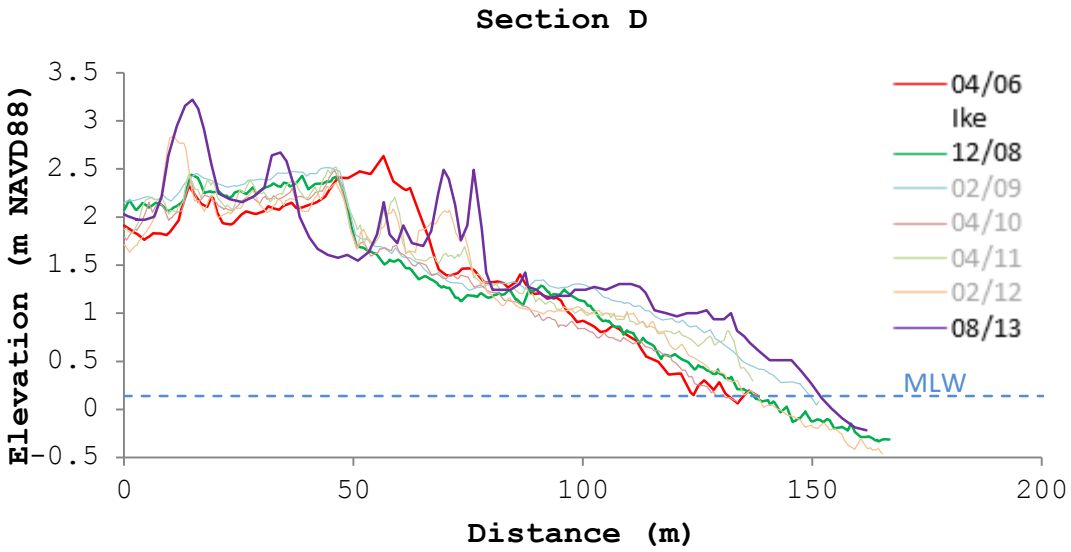

Figure 2.17: Elevation profiles documenting the impact of Hurricane Ike to the foredune and beach as well as the subsequent recovery period at Section D. Cross-shore distance is positive offshore with zero at CR-257.

On the eastern end of the island, the new dune developed landward of the original dune, while in the center of the island the new dune developed at the same location or seaward of the original dune. All profiles showed an advancing of the shoreline from the original shoreline position. For each profile, the volume of sand between the back of the foredune and the shoreline above Mean Low Water (MLW) was calculated. These values are shown in Table 2.10 as a percentage of the pre-Ike volume for each survey date. With the exception of Section C, all sections showed a net gain in sediment volume (up to 25%) after five years of recovery. Each section had a volume recovery of 20-30% from the post-Ike profile. However, on the east end of the island, Sections B & C experienced an initial volume loss of 20-30% so that they only recovered to approximately the same volume as the pre-Ike profile.

Alternatively, in the middle of the island, the sediment volume remained roughly the same immediately after Ike and subsequently increased over the recovery period. The

large initial volume loss at Sections B & C is likely caused by the storm surge ebb being more severe at these sections due to their lower elevation.

Table 2.10: Volume of sediment in the beach and dune system above MLW as a percentage of the pre-storm volume.

Year	Section E	Section D	Section C	Section B	Section A
2008	2.0%	3.0%	-21.0%	-33.3%	-5.0%
2009	10.2%	11.0%	-19.5%	-19.3%	1.6%
2010	-2.8%	-5.8%	-23.9%	-28.4%	1.6%
2011	5.9%	3.7%	-15.3%	-18.6%	14.9%
2012	7.4%	9.6%	-16.3%	-18.6%	13.1%
2013	22.9%	18.2%	-2.1%	4.3%	25.7%

There were no bathymetric surveys conducted near FI immediately after the passing of Ike, so it is difficult to determine how the nearshore bathymetry changed during the storm. The topographic/bathymetric survey conducted in 2013 was used to evaluate the shoreface elevation after five years of recovery. Figure 2.18 and Figure 2.19 show the offshore profiles from pre-storm and post-recovery scenarios on representative Sections A and D, respectively.

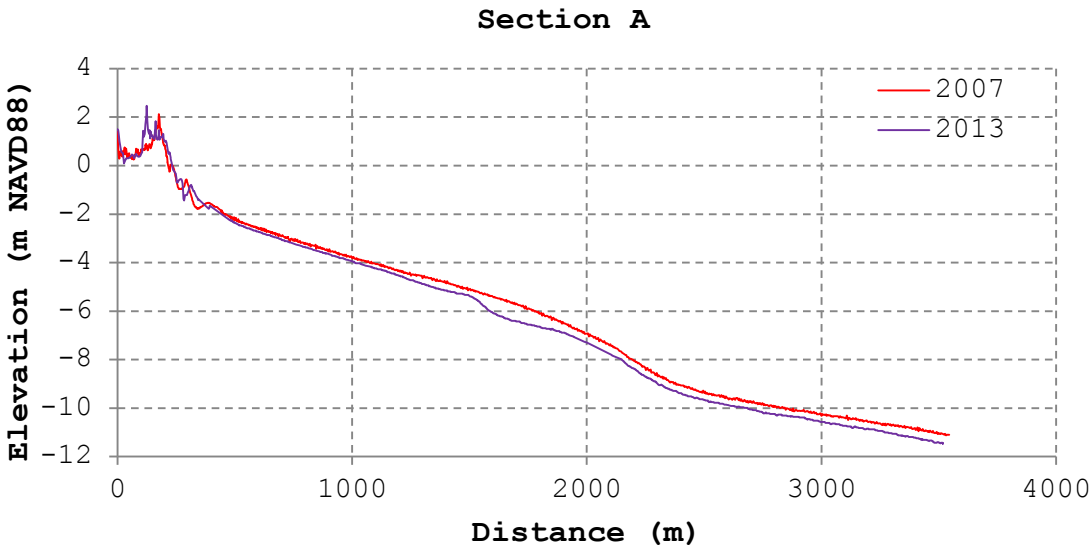

Figure 2.18: Offshore profiles for pre-Ike and post-recovery conditions at Section A.

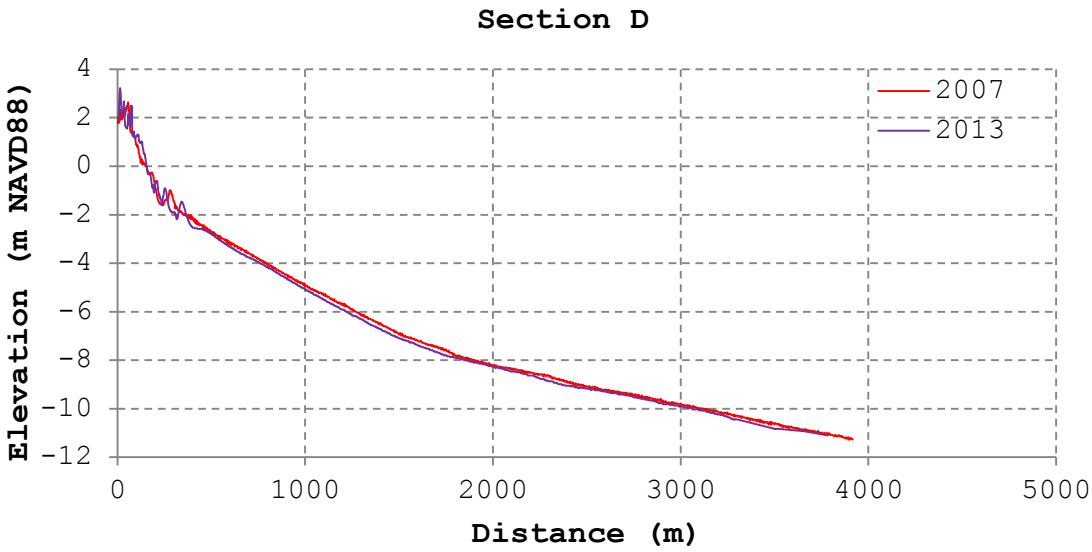

Figure 2.19: Offshore profiles for pre-Ike and post-recovery conditions at Section D.

It is clear from Figure 2.18 that at the east end of the island near the San Luis Pass, the subaqueous shoreface has retreated by up to 180 m despite the advancing subaerial shoreline. This loss in sediment continues offshore to well below a conservative estimate of the depth of closure of -8 m [44], and thus it is likely that the bulk of this loss occurred during the hurricane, depositing sediment along the inner shelf, seaward of our profile data and within the back barrier regions, including the fringing marshes and the open bay. Conversely, Figure 2.19 shows that towards the middle of the island, the subaqueous shoreface retreats by only 50 m. This is likely due to the ebb velocity after the storm being much higher near the SLP inlet than at the center of the island. It should be noted that the net volume gain to the subaerial beach and foredune represent less than 5% of the net sediment loss to the subaqueous shoreface.

3. NUMERICAL MODELING

Numerical modeling has made an extreme impact in the fields of science and engineering over the past few decades. Due to the rapidly increasing memory and processing power of modern computers, numerical modeling has surpassed physical modeling for most engineering applications. The goal of numerical modeling is to use equations derived from physics (either analytical or empirical), and to solve these equations at discrete grid points in a model domain based on prescribed boundary conditions and initial conditions. In engineering the goal of numerical modeling is often to test the performance of a proposed design. However, in this case, the goal of numerical modeling is to show a real-time response of Follett's Island to Ike during all regimes of the storms passing, and to identify the major hydrodynamic driving forces. If the model simulations show validated accuracy, they could then be used in the future to test the performance of proposed coastal protection designs.

For modeling the impact of Hurricane Ike on Follett's Island, two common coastal response models, XBeach and CSHORE, were tested and utilized. These models both include hydrodynamic routines for calculating the propagation of wave energy and water surface elevation as well as morphodynamic routines for calculating sediment suspension and transport and bed level updating.

To develop a reliable model simulation, not only do the governing equations need to be appropriate for the specific scenario (i.e. all assumptions made in the model scheme must be applicable), but the model domain and boundary conditions must also be accurate and appropriately resolved. In this case, an accurate model domain was developed by merging survey data from multiple sources. Since there were no recording stations near the model boundaries, the model boundary conditions had to be extracted from a parent model that simulated the propagation of Hurricane Ike through the entire Gulf of Mexico.

3.1. Model Relief Development

The model domain relief was developed by merging data from four existing sources into an appropriate DEM surface. Table 3.1 identifies each source, as well as its resolution and priority. Figure 3.1 shows the coverage area for each data source. SMS was used to manage and merge these data sets. The working coordinate system for this process was UTM coordinates, zone 15N relative to NAD83. The vertical units and datum for this integration was meters relative to NAVD88. The priority of each data source was based firstly on its survey date (surveys closer to the pre-Ike date having higher priority), secondly on spatial resolution (higher resolution having higher priority), and lastly on data confidence (merged, interpolated, and filtered data having lower priority than raw data).

Table 3.1: Model relief development sources and priorities.

Priority	Source	Data Type	Resolution [m]
1	2006 LiDAR - Brazoria TX	LiDAR point cloud	2-3
2	2007 TerraSond single beam	single beam cross-shore transects	cross-shore: 1 alongshore: 150-1500
3	SL18TX33 ADCIRC Mesh	Unstructured mesh grid	100-600
4	2007 NGDC Galveston DEM	DEM Raster	9-10

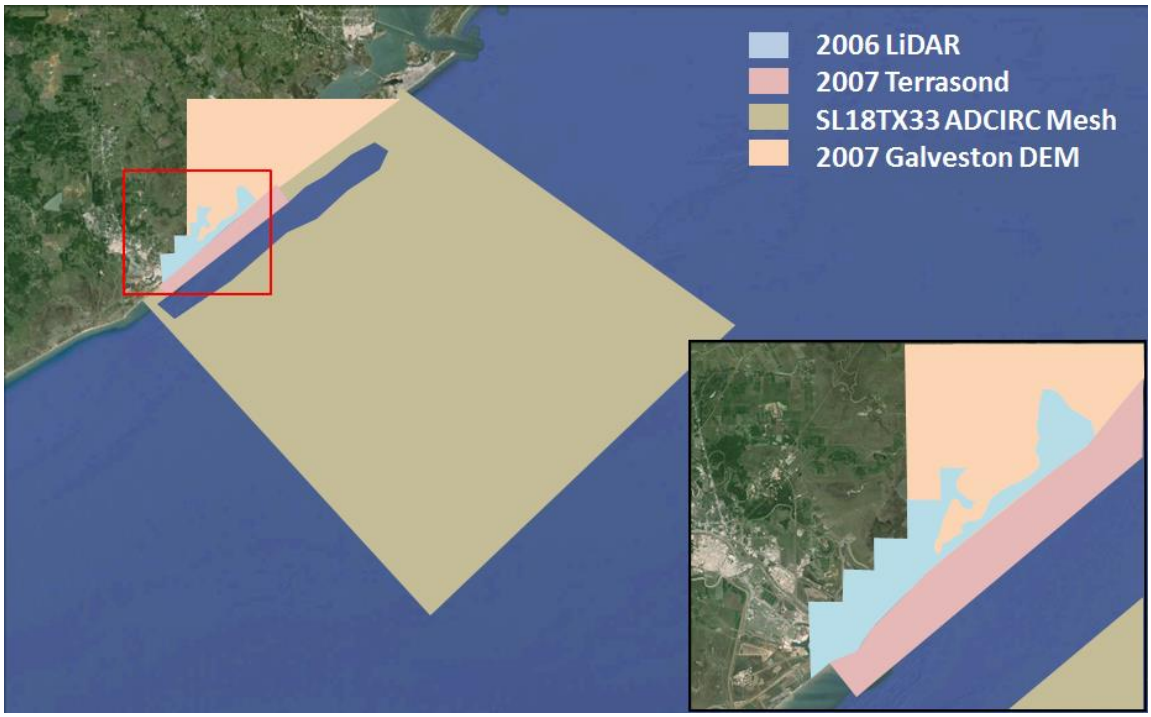

Figure 3.1: Coverage area of each relief source for DEM surface development.

3.1.1. 2006 LiDAR

The 2006 LiDAR survey was ordered by the Texas Water Development Board in early 2006, and was carried out by Sandborn Mapping Company, Inc. between April 9, 2006 and May 13, 2006. Data were delivered as a point cloud with resolution of approximately two meters. The data were provided in geographic coordinates with vertical units of feet relative to NAVD88. Coordinates were re-projected to the working coordinate system and vertical units were converted to meters.

3.1.2. 2007 TerraSond Single Beam

The 2007 TerraSond survey was conducted as part of a study of Surfside Beach and the San Luis Pass for the Texas General Land Office (GLO). The survey was performed by TerraSond Limited in June 2011 with a single-beam cross-shore profiler. The survey had a consistent cross-shore resolution of one meter, and profiles were spaced

alongshore between 1,500 meters (in the middle of Follett's Island) and 150 meters (at the San Luis Pass and Surfside Beach). The survey was delivered in text delimited XYZ format in the working coordinate system. Depths were recorded in feet relative to NAVD88, and were converted to meters in SMS.

3.1.3. SL18TX33 ADCIRC Mesh

The SL18TX33 ADCIRC Mesh was developed by Hope et al. (2013), for modeling the propagation of Hurricane Ike across the Gulf of Mexico [13]. The full domain contains the western North Atlantic Ocean, Caribbean Sea, Gulf of Mexico, and coastal floodplains of Alabama, Mississippi, Louisiana, and Texas. This mesh was cropped in SMS, to include only the area from the Brazos River inlet to the entrance to Galveston Bay and from the shoreline to approximately 70 kilometers offshore. In this region, resolution varies between 600 meters (offshore) to 100 meters at the shoreline. The mesh was delivered in geographic coordinates with depths in meters relative to MSL. Coordinates were re-projected to the working coordinate system in SMS, and depths were converted to NAVD88 using the NOAA software tool VDatum [34].

3.1.4. 2007 Galveston DEM

Although the 2007 NGDC Galveston DEM has a higher resolution than SL18TX33, it is given a lower priority as its source data is much older than SL18TX33. The DEM was developed in 2007 by the National Geophysical Data Center (NGDC) for tsunami inundation modeling as part of the Short-term Inundation Forecasting for Tsunamis (SIFT) program [43]. Data were provided in geographic coordinates with elevations in meters relative to Mean High Water (MHW). The DEM was re-projected to the working coordinate system in SMS and elevations were converted to NAVD88 using VDatum [34].

The DEM covers only the east end of FI, from about 10 km east of the Freeport jetties to the San Luis Pass. In this region, the DEM comprises source data primarily from hydrographic sheets h05521, h10021, and h05488. H05521 and h05488 were both developed in 1934 and are consistent with one another. However, h10021 was developed

in 1982 and is clearly inconsistent with the other two. Since the 2007 DEM was given the lowest priority, this inconsistency is ultimately removed as the higher priority SL18TX33 shares a coverage area with h10021.

3.1.5. Merging the Data

Initially, merging the data sets showed an inconsistency at the boundary between the TerraSond 2007 survey and the SL18TX33 Mesh, where the TerraSond elevation at the boundary was approximately -12.1 meters NAVD88 and the SL18TX22 elevation at the boundary was -10.7 m NAVD88. Since the TerraSond survey was of a higher priority, this inconsistency was corrected by deleting SL18TX33 data points between the TerraSond boundary and the -15 meter NAVD88 contour. The data hole created by this deletion extended in the alongshore direction from 13 km west of the Freeport jetties to 22 km east of the SLP, and in the cross-shore direction from approximately 3.5 km offshore to 12.5 km offshore. Contour lines were then manually drawn in SMS to fill in the data hole. This was done by drawing contours at 1 m intervals from the edge of the data hole at SL18TX33, following the general orientation of the shoreline to the edge of the data hole at the TerraSond survey; making sure that the two surveys transitioned smoothly. The vertices of these contours were then redistributed to approximately 500 m spacing and were converted to scatter points. These new contour scatter points were then merged with the original scatter to fill the data hole, and elevations were linearly interpolated between them to complete the relief surface.

Figure 3.2 shows the scatter points of the merged surface, and Figure 3.3 shows the elevation contours of the surface. Ordinarily, elevations would be converted to MSL using VDatum for modeling purposes. However, the parent model providing the storm surge WSEL is also relative to NAVD88, so it is was not necessary to convert the elevations to MSL. The resulting topography was a data scatterset of varying resolution. This scatterset was later interpolated onto the model grids for XBeach and CSHORE.

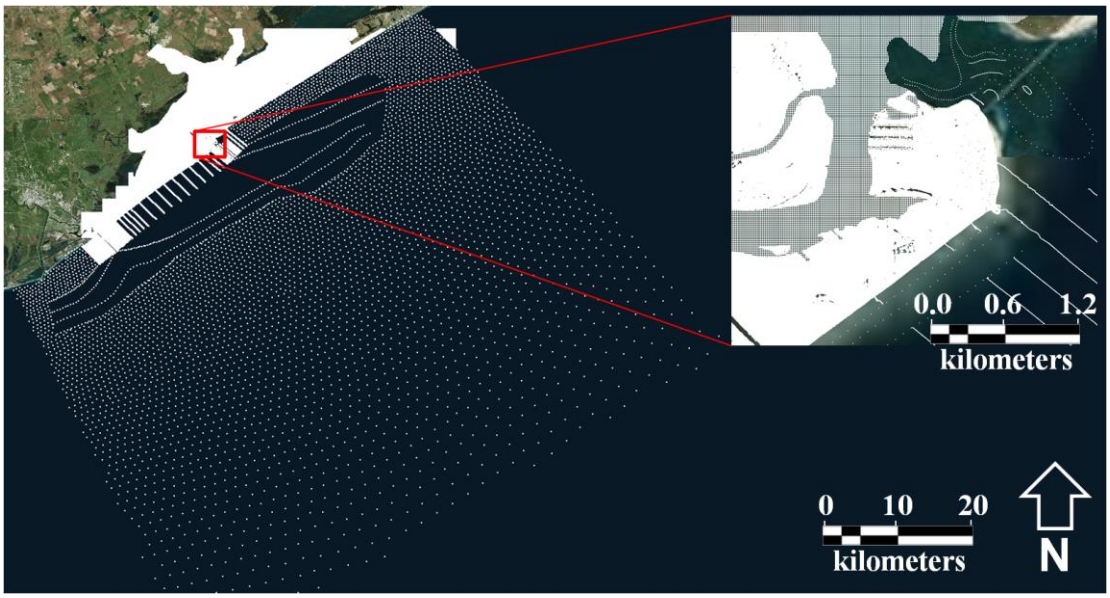

Figure 3.2: Scatter points of merged relief surface. Upper right hand image showing zoomed in view of SLP and the differing resolution of the 2006 LiDAR survey and the 2007 Galveston DEM.

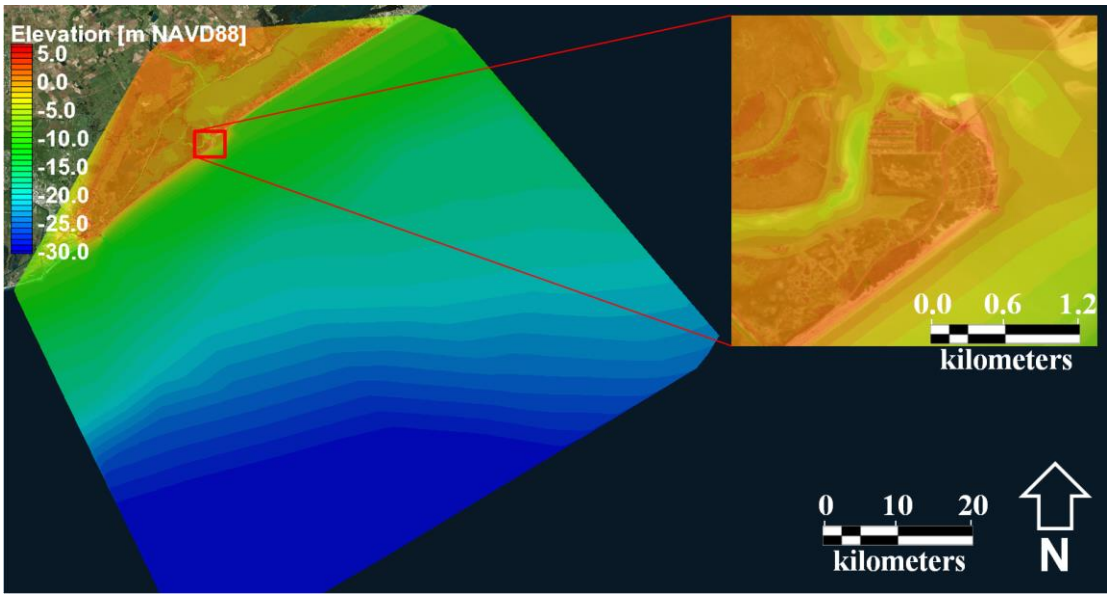

Figure 3.3: Elevation contours of merged DEM surface in meters relative to NAVD88. Upper right hand image showing zoomed in view of SLP.

3.2. Validation of Parent Model

To ensure accurate hydrodynamic forcing conditions for the numerical models XBeach and CSHORE, continuous time series of wave and water level parameters are required at or near the model boundary. Since recorded data in the vicinity of Follett's Island are limited, the continuous boundary conditions must be extracted from large scale numerical modeling results that simulate the hydrodynamics of Hurricane Ike. For this, two potential parent simulations were considered: (1) Coastal Storm Modeling System (CSTORM) model results produced by the USACE Engineer Research and Development Center (ERDC), and (2) ADCIRC+SWAN model results provided by Dr. Casey Dietrich of North Carolina State University [13]. Seven data recording stations from four different sources were used to validate each model. A list of these stations is shown in Table 3.2.

Table 3.2: Measurement stations for validating parent model.

Source	Gauge	Location	Validation Parameters
Andrew Kennedy	V	Nearshore	H_s, T_p, WSEL
Andrew Kennedy	W	Nearshore	H_s, T_p, WSEL
USGS	SSS-TX-BRA-009	Inland	WSEL
USGS	SSS-TX-GAL-015	Shoreline	WSEL
USGS	08117300	Inland	WSEL
USCG	8772447	Shoreline	WSEL

These validation stations are deliberately chosen to represent a variety of hydrodynamic environments in the vicinity of Follett's Island including nearshore, shoreline, and inland. A map showing the locations of these stations is shown in Figure 3.4.

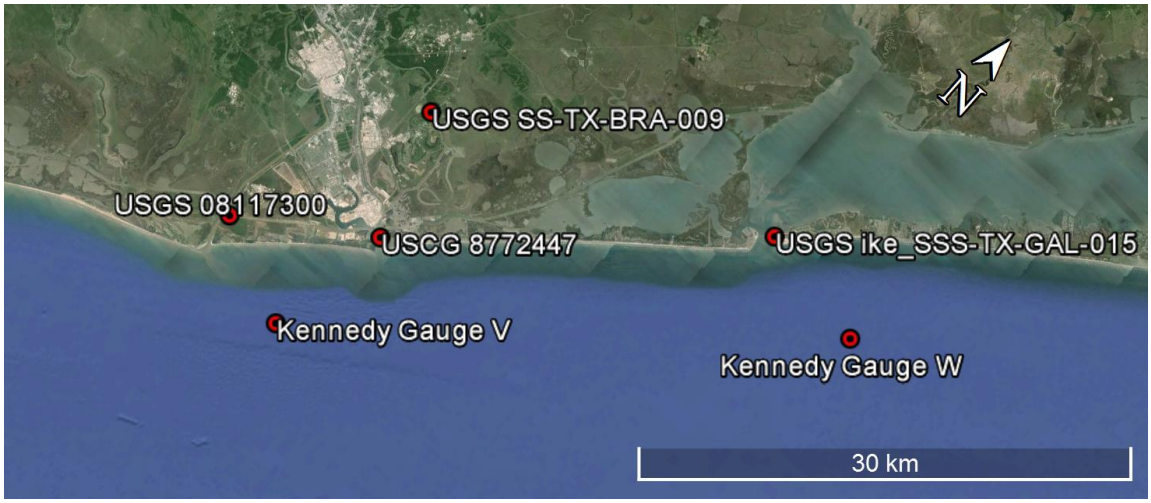

Figure 3.4: Map of parent model validation stations.

3.2.1. ERDC CSTORM

The Coastal Storm Modeling System (CSTORM) was developed by the Engineer Research and Development Center (ERDC). The model applies modern, high-resolution numerical models in a tightly integrated system for simulating the propagation of storms. This modeling suite couples a number of existing models including a tropical planetary boundary layer model (MORPHOS-PBL) for generating cyclone pressure and wind fields, a 2D free surface circulation and transport model (ADCIRC) for generating storm surge and flooding conditions, and both regional and nested nearshore wave models (WAM and STWAVE respectively) for generating wave fields. Water surface elevation and current velocities from ADCIRC are used in STWAVE to calculate wave transformation and breaking, and radiation stresses from STWAVE are used to drive currents in ADCIRC.

3.2.2. SWAN+ADCIRC

Through personal correspondence with Dr. Casey Dietrich of North Carolina State University, Hurricane Ike simulation results using the numerical model SWAN+ADCIRC were acquired. This simulation closely parallels that performed in

Hope (2013), which Dr. Dietrich co-authored [13]. SWAN+ADCIRC uses Best Track files developed by the National Hurricane Center's revised Atlantic Hurricane Database project (HURDAT2) to force the model with a time-varying pressure and wind field. Coupling the unstructured version of SWAN with ADCIRC also allows for accurate and efficient computation as resolution can be increased in areas with large spatial gradients and a global unstructured sub-mesh can be used for both models simultaneously without requiring any expensive interpolation.

This simulation was performed on an over 3-million-node unstructured grid with nearshore resolution as small as 30 m. The model was forced with a storm track that was reconstructed from the real time integrated tropical cyclone observing system, H*Wind [35]. This storm track was then merged into a larger scale wind field generated from additional temporary observation stations [18]. The simulation was run for a model time of 28 days, allowing the storm to propagate and grow across the Caribbean and Gulf of Mexico.

3.2.3. Validation

The time series of water surface elevation in the nearshore region of FI is characterized by two peaks occurring roughly 11 hours apart. The first peak, which occurs on the evening of Sep-12, is resultant of the forerunner surge. The second peak, which occurs on the morning of Sep-13, is resultant of the hurricane storm surge. In the nearshore region, the storm surge peak is of greater magnitude than the forerunner surge. Both models slightly overestimate the storm surge peak WSEL by 0.2-0.4 m in the nearshore region, but underestimate the forerunner surge by up to one meter (Figure 3.5). Additionally, there is a resurgence wave of smaller magnitude occurring one day after the initial surge that was underestimated by about 1 m in both models. The timing of surge onset and retreat is accurately captured in the nearshore environment. In the nearshore, the ADCIRC+SWAN model does a slightly better job of simulating the forerunner surge, but the CSTORM model more accurately predicts the peak WSEL.

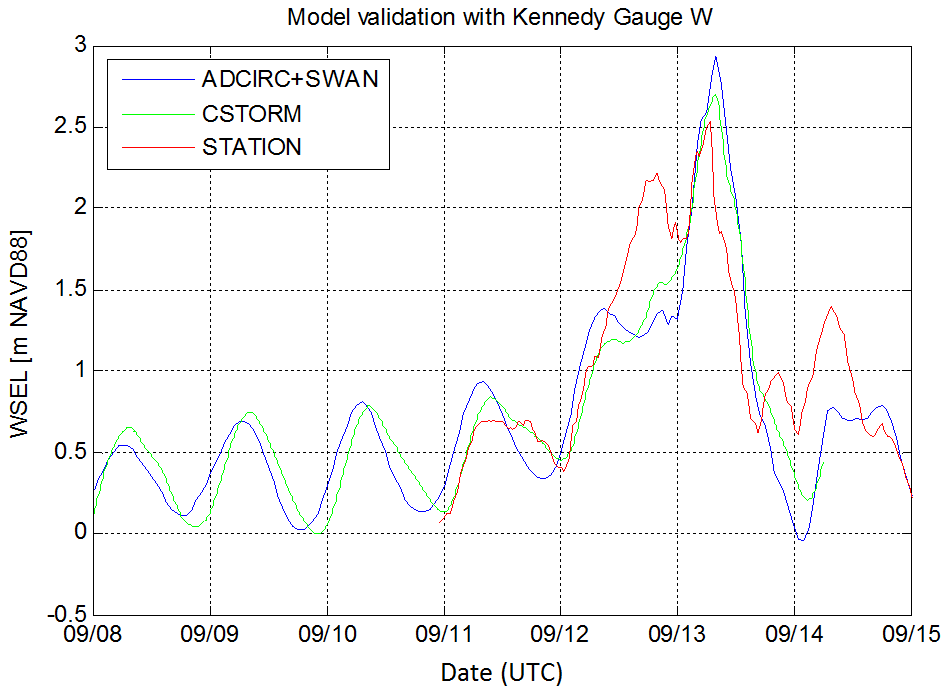

Figure 3.5: Validation of modeled WSEL at a nearshore location: Kennedy Gauge W.

The forerunner surge, which can be attributed to Ekman setup, can be calculated from alongshore momentum equations on the Gulf shelf:

$$\eta_E = \int \frac{fV}{g} dx \tag{3.1}$$

where η_E is the Ekman setup at the coastline, f is the Coriolis parameter, V is the depth-averaged alongshore velocity on the Gulf shelf and x is directed positive onshore [18]. From this equation, it is clear that the magnitude of Ekman setup at the coastline is directly dependent on the alongshore depth averaged velocity and the width of the shelf. One reason that numerical models often fail to accurately capture Ekman setup is that the depth averaged alongshore velocity is very sensitive to bottom friction coefficients,

which are typically assumed to be a global constant value. With better calibration of friction coefficients on the Gulf shelf, it is likely that models would be able to accurately capture the forerunner surge associated with Ekman setup [18].

Interestingly, the storm surge peak seen in Figure 3.5 is greatly reduced in relative magnitude at the shoreline (Figure 3.6). Here the measured forerunner peak is of greater magnitude than the storm surge peak. Both models fail to capture this phenomenon, incorrectly showing the storm surge peak to still be of greater magnitude than the forerunner peak. At the shoreline, both models accurately capture the maximum WSEL, although this peak is lagged by about 12 hours. This could also be due to unrealistic bottom friction factors on the Gulf shelf; particularly in very shallow regions. Both models again fail to capture the resurgence wave occurring on Sep-14.

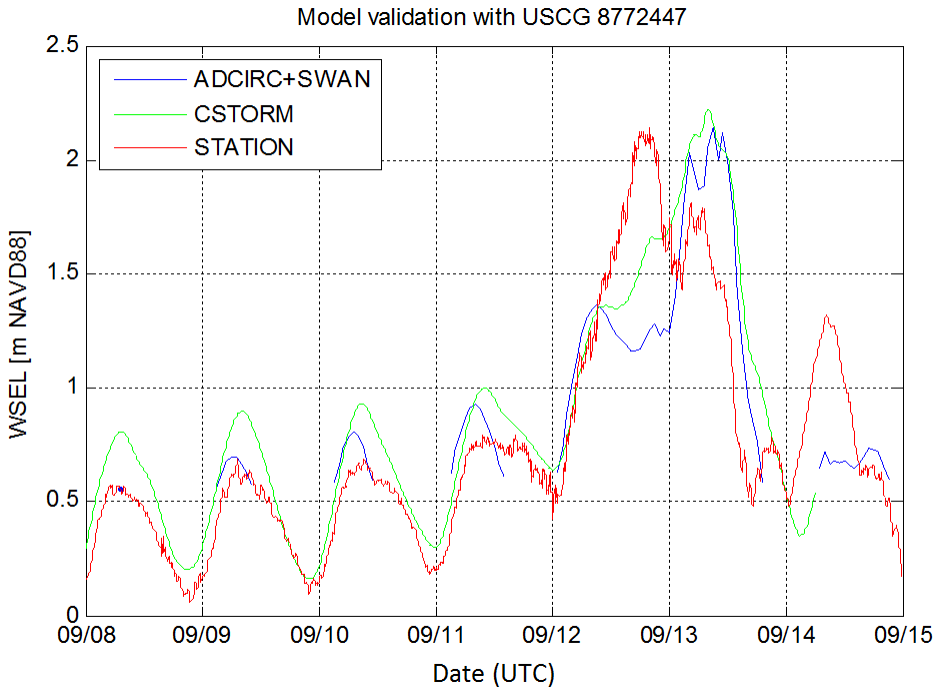

Figure 3.6: Validation of modeled WSEL at a location near the shoreline: USCG Gauge 8772447. The discontinuity in the ADCIRC+SWAN time series is likely due to the gauge location being resolved as a land element that is intermittently wetted and dried.

Figure 3.7 shows the WSEL validation at an inland location for station USGS SSS-TX-BRA-009. Similar to the shoreline validation, both models incorrectly predict the storm surge peak to be of greater magnitude than the forerunner surge peak. In reality the storm surge peak is not observed at this gauge at all. The CSTORM model slightly overestimates the maximum WSEL and the ADCIRC+SWAN model slightly underestimates the maximum WSEL. However, similar to the shoreline location, these maxima have a lag of approximately 12 hours. Also similar to the other validation stations, both models fail to capture the resurgence wave on Sep-14. It is conceivable that the flood and ebb associated with storm surge occurs over a shorter time duration than that associated with the forerunner, and thus the storm surge is not able to propagate as far inland. This is likely not captured in the parent models because they do not have built in routines specifically for overtopping and inundation of barrier islands.

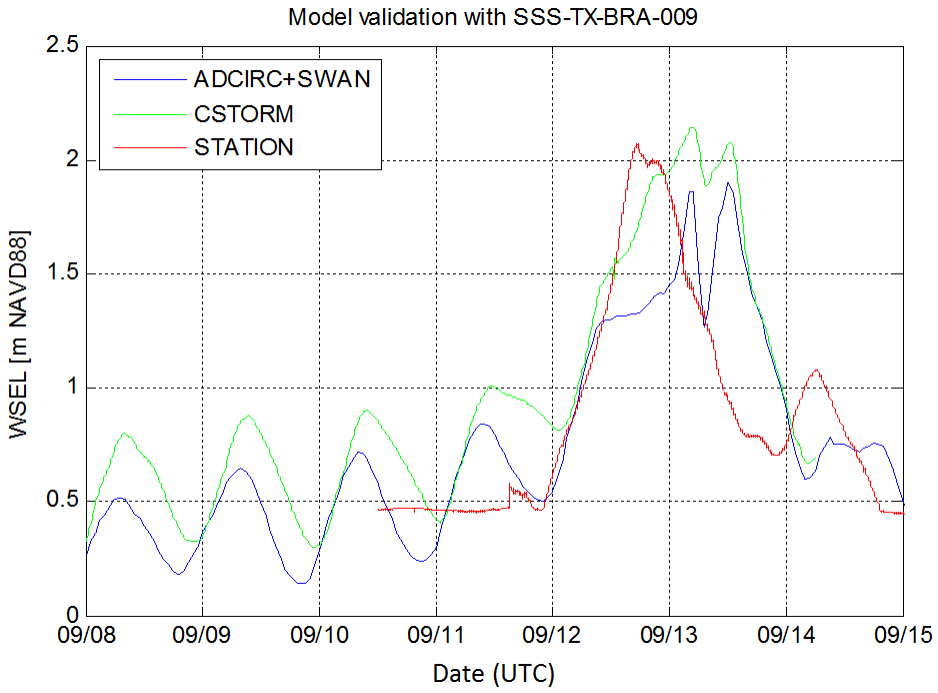

Figure 3.7: Validation of modeled WSEL at an inland location: USGS Gauge SSS-TX-BRA-009.

Figure 3.8 shows the validation of significant wave height and peak period at a nearshore location from Kennedy Gauge W. This validation was limited to the ADCIRC+SWAN parent model, as complications arose in transferring wave modeling results from ERDC. In the nearshore, maximum wave heights were accurately captured to within 0.3 m. The timing of wave onset matched recorded data, however the time of maximum wave height lagged behind observations by approximately 15 hours. The wave height time series was characterized by two peaks of roughly equal magnitude. In the early stages of wave growth on Sep-11, model results match the observed data well. However, after the first 20 hours, the modeled wave heights shoulder off while observed wave heights continue growing to the first peak. The modeled wave heights then grow rapidly to peak at approximately the time of the storm surge peak. Model wave heights also appear to recede more slowly than observed wave heights.

Peak periods are accurately represented by model results. The onset of long wave periods is also very precisely timed, although the decline of long periods lags behind observations by about five hours. Wave periods are slightly overestimated during the two days after landfall. It is likely that wave heights during the forerunner surge peak were not accurately modeled because the forerunner surge itself was not accurately modeled. Lower water levels in the nearshore during that time resulted in an underestimation of wave heights, while the wave period remained unaffected.

In summary, both models are able to accurately capture maximum wave and water level conditions. However, significant wave heights and water levels tend to lag by 12-15 hours. In the absence of a better alternative, either one of these models are acceptable for providing boundary conditions to the coastal response models, especially since the time lag was relatively consistent for both water surface and wave parameters. Since simulation results from both models were fairly consistent, the ADCIRC+SWAN simulation was chosen as the parent model because these data were more accessible than the CSTORM data.

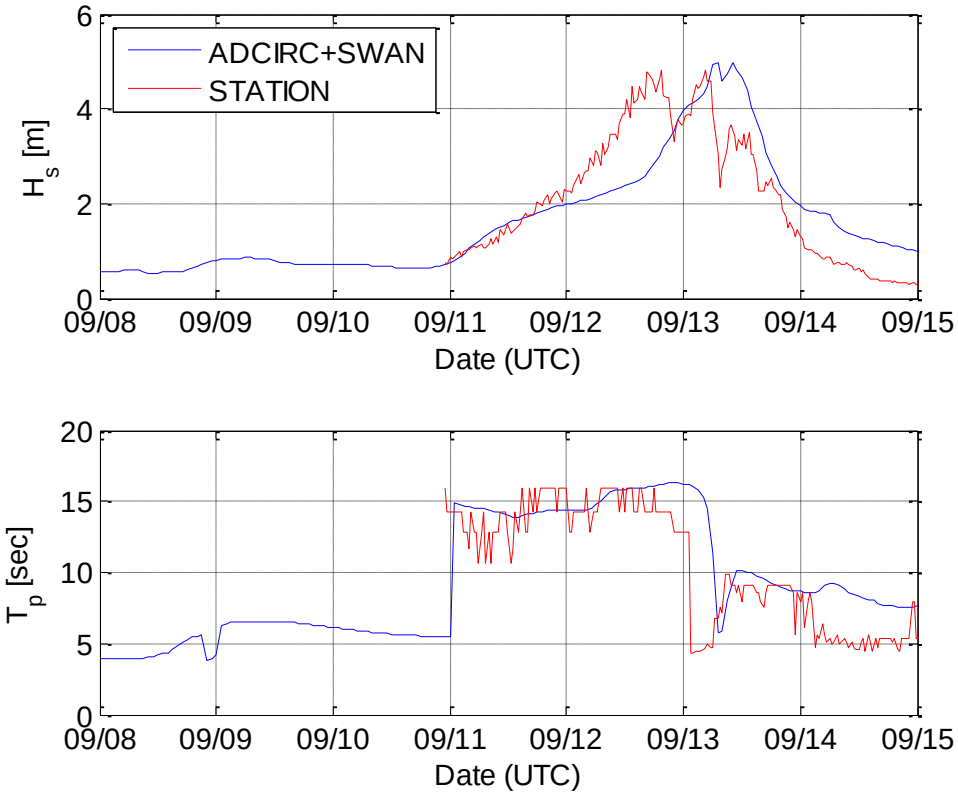

Figure 3.8: Validation of modeled H_s and T_p at a nearshore location: Kennedy Gauge W.

3.3. XBeach

3.3.1. Model Description

XBeach is a powerful numerical modeling tool developed for modeling the coastal response of sandy beach systems to time-varying storm conditions [36]. The model can be run in either 2-D depth averaged mode, solving both alongshore and cross-shore transport, or in 1-D depth averaged mode which assumes alongshore uniformity and calculates only cross-shore transport. The model was built to simulate physical processes within different regimes of a storm as defined by Sallenger (2000): (1) swash regime, (2) collision regime, (3) overwash regime, (4) inundation regime [39]. For resolving swash

dynamics, the model incorporates a 2DH description of wave groups from the time-varying wave action balance. This wave-group forcing drives Infragravity (IG) motions, including both longshore and cross-shore currents. In the collision regime, an avalanching model is used to transport sediment from the dune face (dry) to the swash zone (wet), incorporating the fact that saturated sand moves more readily than dry sand. This is achieved by identifying a critical slope for both wet and dry conditions. For the overwash regime, wave group forcing of low frequency motions are applied with a robust momentum-conserving drying/flooding formulation and sediment transport formulation. Finally, the inundation regime includes a semi-empirical model for breach evolution based on a schematic uniform cross-section.

XBeach includes routines for short-wave envelope propagation (refraction and shoaling), non-stationary shallow water equations, undertow, and non-cohesive sediment transport and bed update, including avalanching, dune erosion, overwash, and breaching. The model includes a time-dependent wave action balance solver, eliminating the need for a separate wave model and allowing different wave groups to travel in different directions. Here the wave action balance is defined as:

$$\frac{\partial A}{\partial t} + \frac{\partial c_x A}{\partial x} + \frac{\partial c_y A}{\partial y} + \frac{\partial c_\theta A}{\partial \theta} = -\frac{D_w}{\sigma} \tag{3.2}$$

where the wave action, A, is defined by:

$$A(x, y, t, \theta) = \frac{S_w(x, y, t, \theta)}{\sigma(x, y, t)} \tag{3.3}$$

and where S_w represents the wave energy density in each directional bin, θ represents the angle of incidence with respect to the x-axis, σ represents the intrinsic wave frequency,

D_w represents the wave energy dissipation, and c_x, c_y, and c_θ represent the wave action propagation speeds in x-, y-, and θ- space respectively.

The roller energy balance is coupled to the wave action balance based on the wave energy dissipation, D_w, and is defined as:

$$\frac{\partial S_r}{\partial t} + \frac{\partial c_x S_r}{\partial x} + \frac{\partial c_y S_r}{\partial y} + \frac{\partial c_\theta S_r}{\partial \theta} = -D_r + D_w \tag{3.4}$$

where $S_r(x,y,t,\theta)$ represents the roller energy in each directional bin, and D_r represents the total roller energy. Radiation stresses from the roller energy balance and the wave action balance are added together to calculate the radiation stress tensor used in the shallow water equation solver. For low frequency and mean flows, the shallow water equations are built into a depth-averaged Generalized Lagrangian Mean (GLM) formulation. These equations are based on the Lagrangian velocity, which in this context is equivalent to the Eulerian velocity plus the Stokes drift. The equations are summarized as:

$$\frac{\partial u^L}{\partial t} + u^L \frac{\partial u^L}{\partial x} + v^L \frac{\partial u^L}{\partial y} - f v^L - v_h \left(\frac{\partial^2 u^L}{\partial x^2} + \frac{\partial^2 u^L}{\partial y^2} \right) = \frac{\tau_{sx}}{\rho h} - \frac{\tau_{bx}^E}{\rho h} - g \frac{\partial \eta}{\partial x} + \frac{F_x}{\rho h} \tag{3.5}$$

$$\frac{\partial v^L}{\partial t} + u^L \frac{\partial v^L}{\partial x} + v^L \frac{\partial v^L}{\partial y} - f u^L - v_h \left(\frac{\partial^2 v^L}{\partial x^2} + \frac{\partial^2 v^L}{\partial y^2} \right) = \frac{\tau_{sy}}{\rho h} - \frac{\tau_{by}^E}{\rho h} - g \frac{\partial \eta}{\partial y} + \frac{F_x}{\rho h} \tag{3.6}$$

$$\frac{\partial \eta}{\partial t} + \frac{\partial h u^L}{\partial x} + \frac{\partial h v^L}{\partial y} = 0 \tag{3.7}$$

where u^L, v^L are Lagrangian velocities, f is the Coriolis coefficient, v_h is the horizontal eddy viscosity, h is the local water depth, τ^E_{bx}, τ^E_{by} are the Eulerian bed shear stresses, η

is the water level, and F_x, F_y are the radiation stress tensors (from wave action balance and roller energy balance).

XBeach solves the depth averaged 2DH advection-diffusion equation to produce transport vectors that are then used to update the bathymetry:

$$\frac{\partial hC}{\partial t} + \frac{\partial hCu^E}{\partial x} + \frac{\partial hCv^E}{\partial y} + \frac{\partial}{\partial x}\left[D_h h \frac{\partial C}{\partial x}\right] + \frac{\partial}{\partial y}\left[D_h h \frac{\partial C}{\partial y}\right] = \frac{hC_{eq} - hC}{T_s} \tag{3.8}$$

where C represents the depth averaged sediment concentration, u^E, v^E are Eulerian mean velocities, D_d is the sediment diffusion coefficient, and T_s is a modified time scale based on sediment fall velocity and local water depth. These formulations rely on the non-hydrostatic calculation of the wave group envelope and accompanying IG waves (including bound, free and trapped longwaves). Infragravity waves make a significant contribution to shoreline erosion during storms, since a large portion of the offshore suspended sediment transport occurs at IG frequencies [25].

In (3.9) and (3.10), the equilibrium sediment concentration C_{eq} is calculated using the Soulsby-Van Rijn transport formulation [41]:

$$C_{eq} = \frac{A_{sb} + A_{ss}}{h}\left(\sqrt{u^2_{stirring}} - u_{cr}\right)^{2.4}(1 - \alpha_b m) \tag{3.9}$$

$$u_{stirring} = \sqrt{(u^E)^2 + (v^E)^2} + 0.018\frac{u^2_{rms}}{C_d} \tag{3.10}$$

where A_{sb} and A_{ss} are bed and suspended load coefficients respectively, $u_{stirring}$ is the Soulsby-Van Rijn stirring velocity, u^E, v^E are Eulerian velocities, u_{rms} is the RMS bottom orbital velocity from wave action, C_d is the drag coefficient, u_{cr} is the threshold current

speed (from Van Rijn method), α_b is a calibration factor and m is the bed slope (Soulsby, 1997). Here A_{sb} and A_{ss} are functions of the median sediment grain size (D_{50}), the ratio of densities of sediment grains to water, and the water depth. Furthermore, u_{cr} is a function of D_{50}, the 90th percentile grain size D_{90}, and the local water depth.

Finally, the bed level is updated based on gradients in sediment transport rates:

$$\frac{\partial z_b}{\partial t} + \frac{f_{mor}}{(1-p)}\left(\frac{\partial q_x}{\partial x} + \frac{\partial q_y}{\partial y}\right) = 0 \tag{3.11}$$

where z_b is the bed level, f_{mor} is a morphological acceleration factor, p is the sediment porosity, and q_x and q_y are sediment transport rates in the cross-shore and alongshore directions respectively.

3.3.2. Grid Generation

XBeach uses a 2D-rectilinear grid with variable grid spacing in both x- and y-directions. The model grid is oriented with the positive x-direction onshore and positive y-direction alongshore, with the grid origin at the lower left corner at the offshore boundary. This orientation allows the variable x-resolution to efficiently resolve cross-shore features like the foredune.

The model grid for XBeach simulations was generated using both SMS and the XBeach MATLAB Toolbox. A high resolution regular grid was created using the CMS-Wave module in SMS with the offshore boundary oriented at 128° TN (the approximate orientation of the shoreline). The grid was then manually transformed to a zero-origin and vertical orientation. No vertical datum shift was required since WSEL from the parent model was also provided relative to NAVD88.

The XBeach MATLAB toolbox, available through the OpenEarth tools subversion network, was then used to re-interpolate the high resolution regular grid onto a rectilinear grid. Using the toolbox, the variable cross-shore resolution can be calculated

automatically using a specified Courant condition of 0.7 [5] with the maximum offshore boundary resolution calculated based on a minimum mean period and a user defined minimum dry land resolution. This method created an unreasonably small cross-shore resolution in the back bay (where wave action is expected to be minimal). Thus, the cross-shore resolution of the back bay was adjusted to 20 m to minimize computational expense. The final cross-shore resolution varied between 20 m at the offshore and back bay boundaries and 5 m at the shoreline. The longshore resolution was defined as a constant value of 25 m. Since waves during Ike approach predominantly from the east and southeast, the bottom boundary would create a significant wave shadow zone on the area of interest. To deal with the shadow zone the grid was extended to the northeast to include the western end of Galveston Island.

The final grid encompassed all of Follett's Island from approximately 2.5 km offshore to half way through Christmas Bay (Figure 3.9). The lateral extent was from the west end of Galveston Island to the Freeport Jetties. After some testing, it was concluded that the land elevation of the area north of the Gulf Intracoastal Waterway had to be lowered to -0.5 m NAVD88 to ensure accurate surge forcing along the back boundary. This region originally had an average elevation of 2 m NAVD88. Similarly, land elevations on the back, top and bottom boundaries were also lowered to ensure accurate surge forcing. Figure 3.10 compares the original resolution of topographic features on FI to the gridded resolution. Although some of the smaller features have been smoothed over, the defining features of the island are still accurately portrayed.

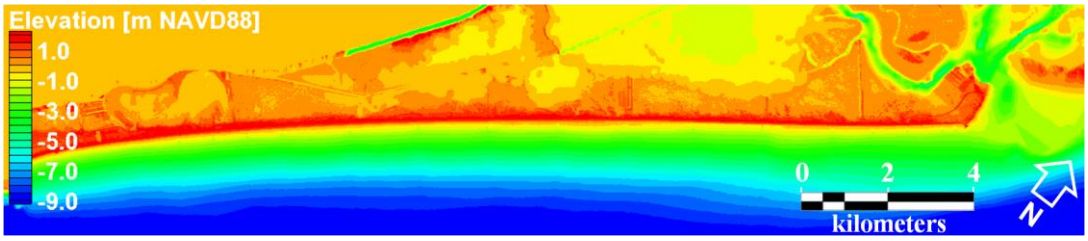

Figure 3.9: Bounds and relief of the XBeach model grid.

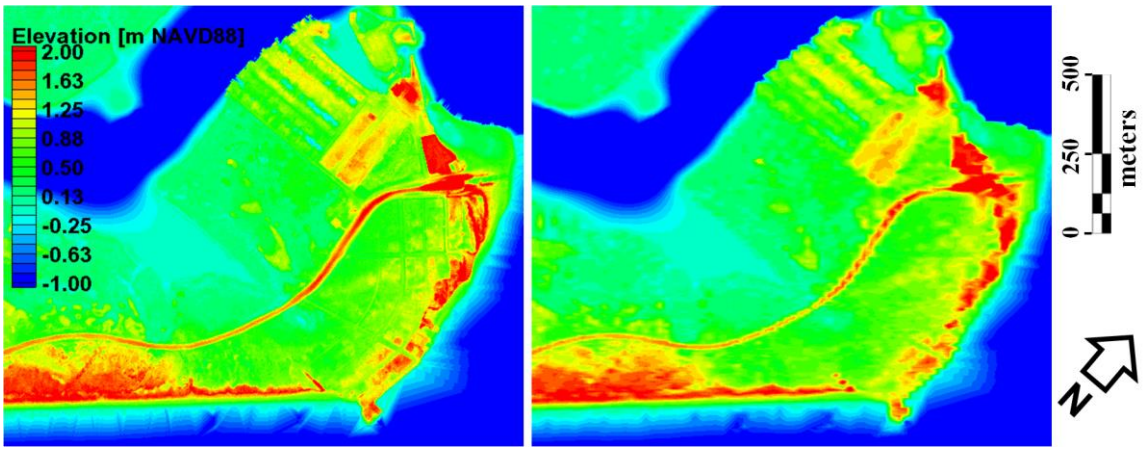

Figure 3.10: Comparison of San Luis Island resolution between the original relief model (left) and the XBeach model grid (right).

3.3.3. Model Setup

Time histories of water surface elevations from the parent model SWAN+ADCIRC were extracted at the four corners of the XBeach model domain. The model was run for a total model time of 96 hours beginning Sep-10, 2008 15:00 GMT. Time histories from the parent model were zeroed to this start time and were used as water surface boundary conditions for the XBeach model. Water surface boundary conditions are applied at the corners of the model domain and are interpolated spatially along the boundary edges. The time steps of the water surface boundary conditions are also linearly interpolated onto the model time step, meaning that the input temporal resolution of water surface can be large as long as it accurately resolves storm surge.

Time histories of significant wave height, peak wave period and mean wave direction were extracted from the parent model at eleven locations on the offshore boundary of the XBeach grid. Since the wave parameter time histories were very similar at these locations, the time history from the center of the offshore boundary was applied to the entire boundary for a more efficient computation. Although the JONSWAP spectrum was not intended for hurricane conditions, spectra within eight times the radius

from a hurricane center to the point of maximum wind speed behave similarly to fetch limited spectra, and are accurately approximated by the parametric JONSWAP spectrum [46]. The time steps of wave parameters are linearly interpolated onto the model time step. Thus, the input wave parameter time step needs to be only small enough to resolve the bound long waves.

XBeach is a computationally intensive model, and as an option to reduce the run time, a morphological acceleration (morfac) scheme was built into the code (Eq. 3.10). This allows the possibility of artificially reducing the total model time by accelerating hydrodynamic forcing and compounding sediment transport rates by some factor. In other words, the morphological time scale is sped up by some prescribed factor relative to the hydrodynamic time scale. For example, running a simulation with a morfac value of 10 means that the hydrodynamics are only run for 6 minutes each hour, and the bottom changes per time step are multiplied by a factor of ten. A sensitivity analysis was conducted comparing bed changes with morfac values of 1, 2, 5 and 10. For the sensitivity test, the 1-D version of XBeach was used to speed up the process by simulating the coastal response along cross-shore Section A. Figure 3.11 compares the final bed elevation with morfac values from 1 to 10. A summary of these results is shown in Table 3.3.

The results of this sensitivity test show that using morphological acceleration results in nearly zero change in the final bed level, despite a significant reduction in computation time. This confirms the findings of Lindemer et al. (2010), who studied the impact of Hurricane Katrina on the Chandeleur Islands, Louisiana. Lindemer et al. (2010) found that varying the morfac parameter between 1 and 20 resulted in less than a 2% difference in bed level change [23]. When analyzing an animation of these results, it is clear that storm surge ebb and dune inundation are the two largest contributors to the coastal response of FI to Hurricane Ike. These two regimes are associated with high velocities and high equilibrium sediment concentrations caused by sheet flow, which results from a cross-shore gradient in water level specifically over the dune crest. Thus it is clear that sheet flow is the primary contributor to the final erosion pattern.

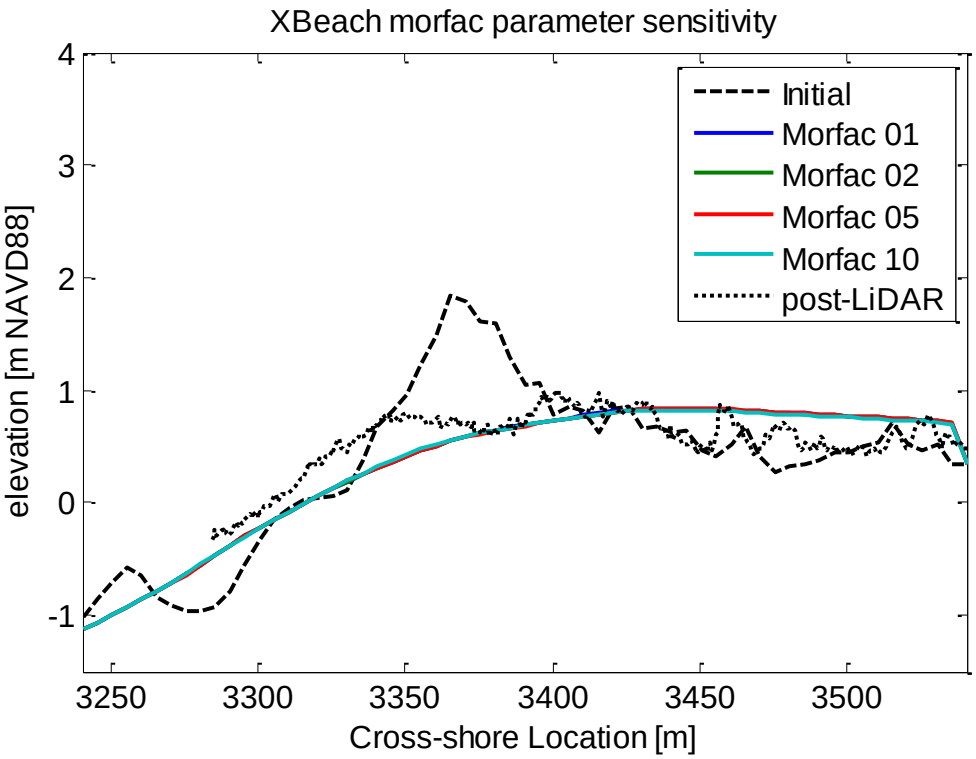

Figure 3.11: Final land surface elevation comparison from XBeach model with varying morfac values. The simulation was run in 1-D mode on cross-shore Section A.

Table 3.3: Xbeach morfac sensitivity testing on Section A. Total eroded and accreted sediment volume in XBeach with varying morfac values.

Morfac	Computation time [min.]	Total Volume Accreted [m^3/m]	Total Volume Eroded [m^3/m]
10	2.9	10.32	-12.87
5	5.0	10.62	-13.03
2	11.4	10.59	-13.00
1	25.0	10.63	-12.93

McCall et al. (2008) determined that XBeach will tend to over predict the morphological change associated with sheet flow, such as during the inundation regime

[26]. Thus, XBeach has a built-in trigger to artificially limit the maximum Shields number to a constant value, with recommended values between 0.8 and 1.2 (Eq. 3.12).

$$u_{stirring}^2 = \min\left(u_{stirring}^2, \theta_{sf}\frac{gD_{50}\Delta}{c_f}\right) \tag{3.12}$$

where $u_{stirring}$ is the Soulsby-Van Rijn stirring velocity during sheet flow (Eq. 3.10), θ_{sf} is the threshold Shields parameter for the start of sheet flow (denoted as smax in the XBeach model input), D_{50} is the median sediment grain size, and Δ is the relative density of the sediment. This method assumes that during sheet flow, higher velocities correspond to higher transport rates, but not to higher equilibrium sediment concentrations (Eq. 3.9).

Another sensitivity test was conducted on the smax factor to test how varying this parameter affects the final bed elevation Figure 3.12 compares the final bed elevation with smax values from 0.8 to 1.2. A summary of the eroded and accreted volumes from these results is shown in Table 3.3. It is clear that specifying a higher maximum Shields number leads to a greater magnitude of bed level change. Figure 3.12 shows that using a smax value of 0.8 results in the most accurate bed level at Section-A. Thus, this value was chosen for the base simulation. Similarly, since applying a morphological acceleration factor increased computational efficiency without affecting the final results, a morfac value of 10 was chosen for the base XBeach simulation.

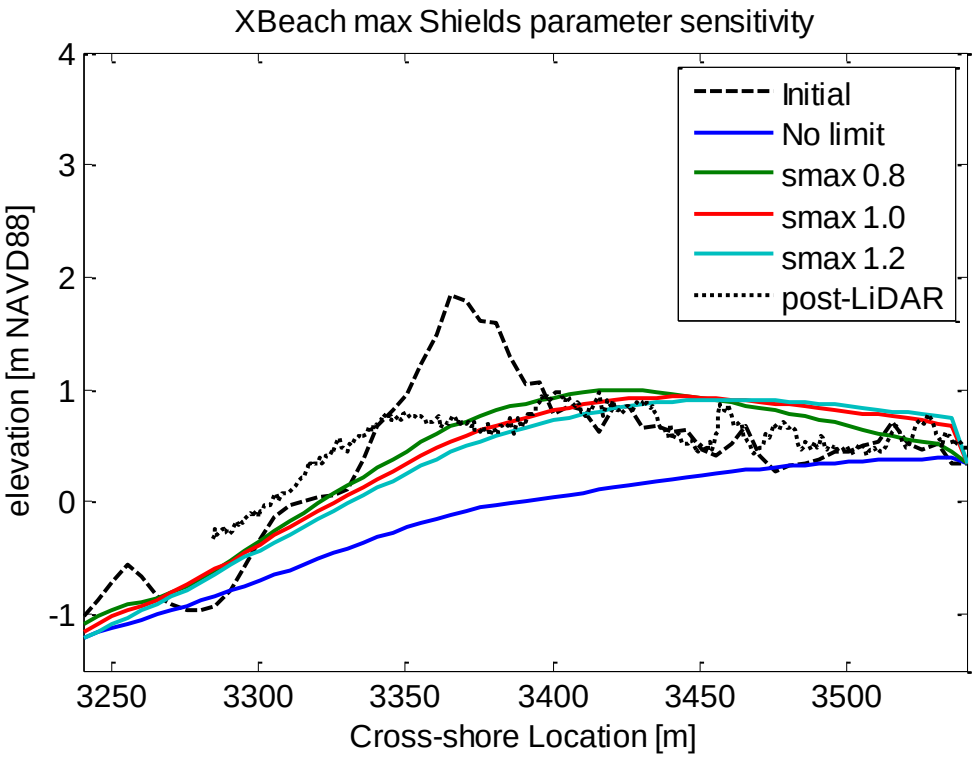

Figure 3.12: Final land surface elevation comparison from XBeach model with varying smax values. Simulation was run in 1-D mode on cross-shore Section A.

Table 3.4: Xbeach smax sensitivity testing on Section A. Total eroded and accreted sediment volume in XBeach with varying smax values.

smax	Computation time [min.]	Total Volume Accreted [m^3/m]	Total Volume Eroded [m^3/m]
No Limit	4.9	3.10	-35.87
1.2	5.0	10.58	-17.02
1.0	4.8	10.44	-14.17
0.8	4.8	9.14	-11.26

The additional free parameters contained in XBeach which govern model numerical schemes, breaker parameters, critical avalanching slopes, etc. were all left at their default

values. The model parameters (params.txt), wave forcing (waves.txt), and tidal forcing (tide.txt) input files are copied in Appendix A. The model was run for a total model time of 96 hours, outputting global water level, significant wave height, depth averaged velocity, roller energy and suspended sediment concentration every 15 minutes.

3.4. CSHORE

3.4.1. Model Description

CSHORE is a very efficient 1D cross-shore coastal response model. The model includes a time-averaged and depth-averaged combined wave and cross-shore current model, a time-averaged sediment transport model, a probabilistic model for an intermittently wet and dry zone, as well as empirical formulas for irregular wave runup [14][19]. A more robust 2D version of the model, C2SHORE, is currently under development, and the following model formulations include longshore gradients that are neglected in the applied version of CSHORE.

The wave and current model is based on the time-averaged continuity and momentum (Eqs. 3.13-3.15), the wave action (Eq.3.16), and the roller energy (Eq. 3.17).

$$\frac{\partial}{\partial x}(Q_x) + \frac{\partial}{\partial y}(Q_x) = 0 \tag{3.13}$$

$$\frac{\partial}{\partial x}\left(\frac{{Q_x}^2}{\bar{h}}\right) + \frac{\partial}{\partial y}\left(\frac{Q_x Q_y}{\bar{h}}\right) + g\bar{h}\frac{\partial \bar{\eta}}{\partial x} + \frac{\tau_{bx}}{\rho} = \tau_{wx} + \frac{\tau_{sx}}{\rho} \tag{3.14}$$

$$\frac{\partial}{\partial x}\left(\frac{Q_x Q_y}{\bar{h}}\right) + \frac{\partial}{\partial y}\left(\frac{{Q_y}^2}{\bar{h}}\right) + g\bar{h}\frac{\partial \bar{\eta}}{\partial y} + \frac{\tau_{by}}{\rho} = \tau_{wy} + \frac{\tau_{sy}}{\rho} \tag{3.15}$$

where Q_x, Q_y are time-averaged volume fluxes, $\bar{h}$ is the mean water depth, $\bar{\eta}$ is the wave setup, τ_{bx}, τ_{by} are bottom shear stresses, τ_{sx}, τ_{sy} are wind shear stresses on the water

surface, and τ_{wx}, τ_{wy} are wave-induced shear stresses (estimated from the gradient in wave induced fluxes and radiation stresses). The wave action equation is expressed as:

$$\frac{\partial}{\partial x}\left[\frac{E}{\omega}\left(C_g \cos\theta + \frac{Q_x}{\bar{h}}\right)\right] + \frac{\partial}{\partial y}\left[\frac{E}{\omega}\left(C_g \sin\theta + \frac{Q_y}{\bar{h}}\right)\right] = -\frac{D_B - D_f}{\omega} \tag{3.16}$$

where E is the wave energy, ω is the intrinsic angular frequency, C_g is the group velocity, θ is the incident wave angle, and D_B, D_f are dissipation rates due to wave breaking and bottom friction respectively. The roller volume flux, q_r, is computed using the roller energy equation:

$$\frac{\partial}{\partial x}(\rho C^2 q_r \cos\theta) + \frac{\partial}{\partial y}(\rho C^2 q_r \sin\theta) = D_B - D_r \tag{3.17}$$

where C is the phase velocity, q_r is the roller volume flux, and D_r is the roller dissipation rate.

This model calculates cross-shore variations of the mean and standard deviation of the free surface elevation as well as the depth-averaged cross-shore and longshore velocities. Since CSHORE is a 1D time-averaged model, it cannot accurately model areas with large alongshore bathymetric gradients; thus it is most effective when applied to a profile where bathymetric contours are parallel.

The sediment transport model incorporates the hydrodynamic forcing into a depth-averaged suspended sediment load and bed load. Suspended sediment volume is related to sediment fall velocity and the energy dissipation rates (Eqs. 3.16 and 3.17), and the suspended sediment transport rate is related to the undertow current and the horizontal cross-shore velocity. Bed load transport rate depends on the standard deviation of the depth-averaged horizontal velocity. Incipient mobilization of sediment is calculated

using a critical Shields parameter (Ψ_c) of 0.05. The net cross-shore sediment transport rate is the sum of the net bed load and suspended sediment transport rates.

This model is limited to globally uniform sediment parameters characterized by the median diameter (D_{50}), the fall velocity (w_f), and the specific gravity (s). The probabilistic model for the wet and dry zone was calibrated and verified by the developers using small-scale lab tests. This model is used to predict wave overwash and structural damage progression. One weakness of CSHORE is that in its current state it cannot calculate offshore sediment transport due to storm surge ebb, which is a major contributor to the response of FI to Hurricane Ike. However, it is expected that the initial morphodynamic response to the storm can be computed.

3.4.2. Model Setup

Time histories of water surface elevation, significant wave height, peak wave period, and mean wave direction were extracted from the parent model SWAN+ADCIRC at the offshore boundary of each profile. Wave incident angles at the offshore boundary were converted relative to shore-normal.

The 1D bathymetry file is oriented positive shoreward with the origin at the offshore boundary. These profiles were extracted along the eight survey transects from TerraSond (2007) and TAMUG (2013) so that bed level changes could be compared with actual surveys. The model domain was truncated at CR-257 to maintain consistency with the analysis of LiDAR data. CSHORE requires that the prescribed surge level never exceed the highest bed level in the domain. To ensure stability of the simulation, the model domain was artificially extended 20 meters landward at the elevation of the last point in the domain, and an artificial non-erodible vertical wall was defined at the final landward point. The simulations were run for a total of 96 hours of model time beginning Sep-10, 2008 15:00 GMT. Each simulation had a run time of approximately one minute. Global outputs of root-mean-square wave height (H_{rms}), water levels, bed levels, velocities and suspended sediment loads were recorded hourly. An example model setup using the MATLAB toolbox is provided in Appendix B.

4. MODEL ANALYSIS AND RESULTS

4.1. XBeach Simulation

The XBeach simulation was run in parallel on 8 cores, and had total run time of 43 hours. The simulation clearly captures processes involved in the collision, overwash, and inundation regimes outlined by Sallenger (2000) [39]. In addition to these regimes, it is clear that storm surge ebb also plays a large role in transporting sediment offshore, a phenomenon also recognized by Goff et al. (2008) and Hayes (1967) [10][11]. Figure 4.1 shows snapshot images from an approximately 2 km long by 1 km wide portion of the model domain during the collision regime, overtopping regime, inundation regime, and during storm surge ebb.

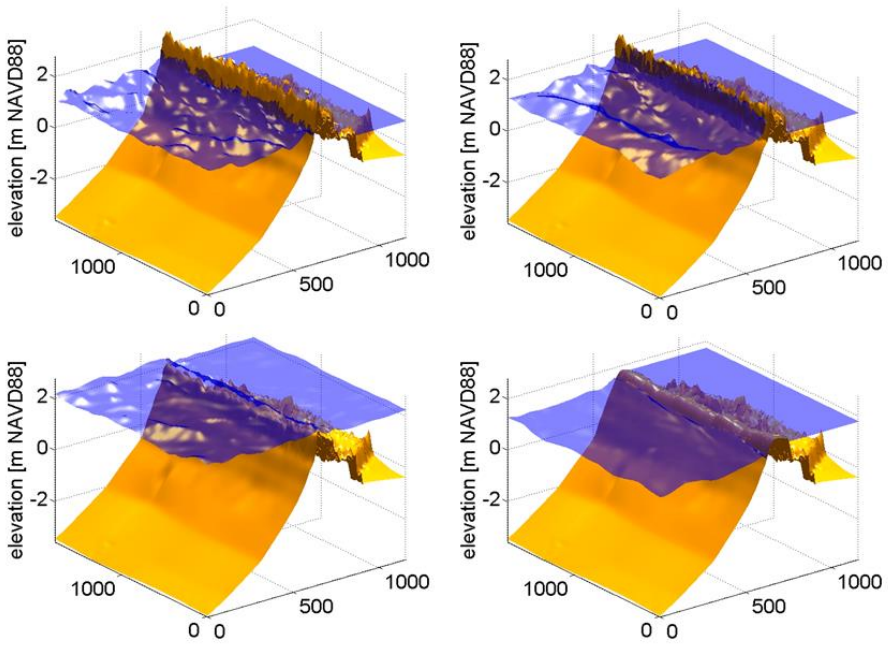

Figure 4.1: Snapshot of water surface (long waves only) and bed level during the collision regime (top-left), during the overtopping regime (top-right), during the inundation regime (bottom-left), and during storm surge ebb (bottom-right).

From hours 32 to 52, the island was in the overtopping regime, during which time the foredune crest elevation was lowered slightly in some areas as wave runup washed sediment from the lower elevation dunes to the back barrier. During this regime, the morphological response was mostly limited to the dune and immediate back-barrier where dune overwash sediments were deposited just landward of the foredune. Beach erosion during this regime was minimal.

From hours 52 to 62, FI experienced massive erosion of the foredune during the inundation regime. In the hours leading up to landfall, the storm surge spiked rapidly and the foredune, which had already been lowered slightly during the overwash regime, were uniformly inundated causing a large volume of sediment to be transported from the foredune to the back barrier and back bay. During this regime, wave action was minimal and the sheet flow from the surge gradient dominated the sediment transport process.

From hours 62 to 73, high velocities from the ebbing storm surge pulled large volumes of sediment offshore, further flattening and lowering the beach and steepening the subaqueous shoreface. After the storm surge ebb, the island also experienced a resurgence wave; however this wave was not large enough to overtop the island a second time. This resurgence wave had minimal impact on the shoreface, but did raise the forebeach elevation slightly.

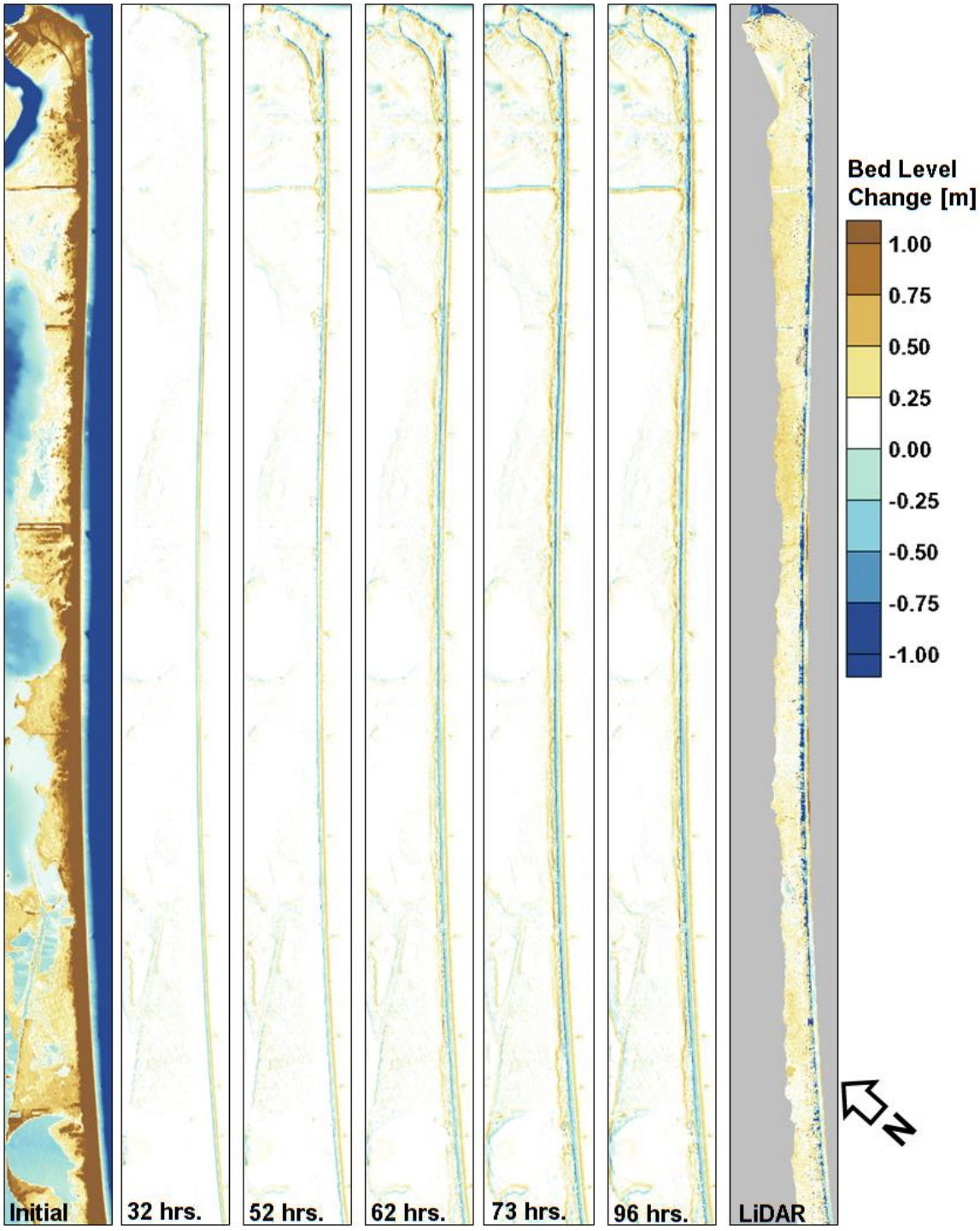

Figure 4.2: Initial bed level of FI (left panel). Simulated erosion and deposition patterns at the end of the collision, overwash, and inundation regimes and at the end of the simulation (center four panels). Measured difference from LiDAR (right panel).

The volume changes associated with Figure 4.2 are shown in Table 4.1. It is clear from this table that the total accreted and eroded sediment volume increased by nearly 60% during the 10 hour inundation regime. During this time the accretion and erosion rates were 50 - 100% higher than during any other regime. During the 11 hours storm surge ebb regime, the rates of erosion and accretion were about half those during the inundation regime but still about 50% higher than during the other regimes.

Table 4.1: XBeach simulated volume of subaerial accretion and erosion at the end of the collision regime (32 hrs.), the overwash regime (52 hrs.), the inundation regime (62 hrs.), the storm surge ebb (73 hrs.), and at the end of the model (96 hrs.).

	Volume accreted [m^3]	Accretion rate [m^3/hr]	Volume eroded [m^3]	Erosion rate [m^3/hr]	Net volume change [m^3]
		+11,226		-10,175	
32 hrs.	+359,252		-325,601		+33,651
		+11,957		-9,709	
52 hrs.	+598,407		-519,788		+78,618
		+31,589		-30,065	
62 hrs.	+914,301		-820,441		+93,860
		+17,214		-21,390	
73 hrs.	+1,103,664		-1,055,741		+47,923
		+3,388		-4,003	
96 hrs.	+1,181,603		-1,147,824		+33,779
LiDAR	+1,430,593		-833,440		+597,153

Simulated post-storm bed level profiles were compared with post-storm LiDAR profiles along Sections A-H (Figure 2.15). Sample profiles from Section A and Section D are shown in Figure 4.3 and Figure 4.4 respectively. Figures from all cross sections are included in Appendix D. It is clear from these figures that the overwash regime had a much more significant impact on Section A than on Section D. This is likely due to the fact that the initial dune crest elevation at Section A was approximately 50 cm lower

than at Section D. Furthermore, due to the lower elevation on the east end of the island, the resurgence wave had a much greater impact on Section A than any of the other sections. Here the shoreline was extended farther offshore between hours 73 and 96, where the other areas experienced little impact.

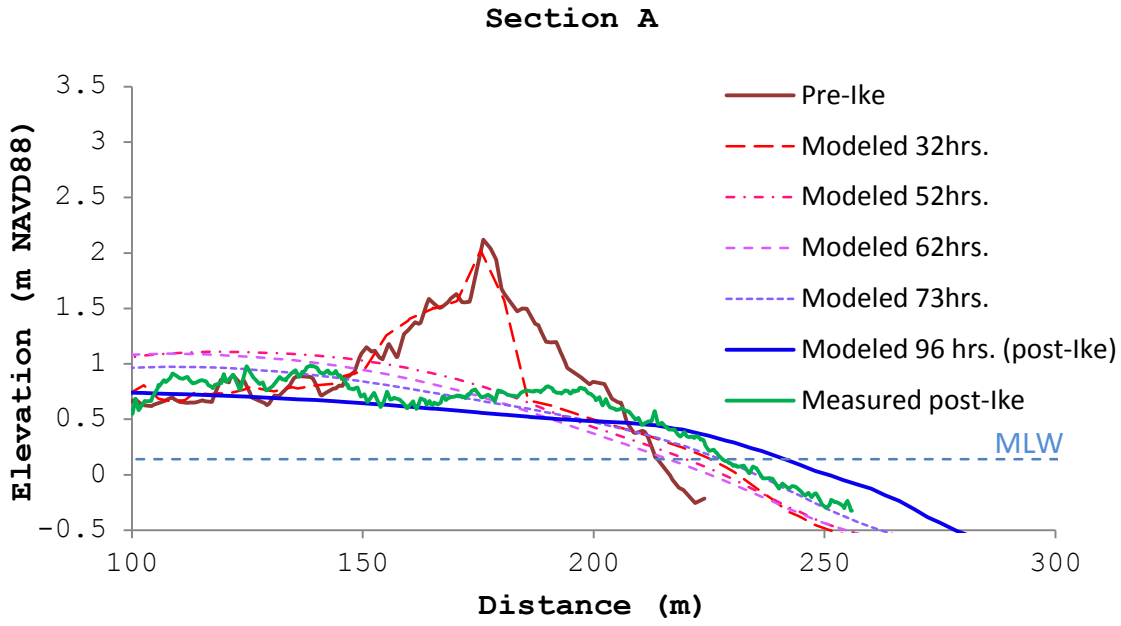

Figure 4.3: XBeach simulated bed level evolution compared to pre- and post-storm bed level extracted from LiDAR data at Section A (the west end of FI).

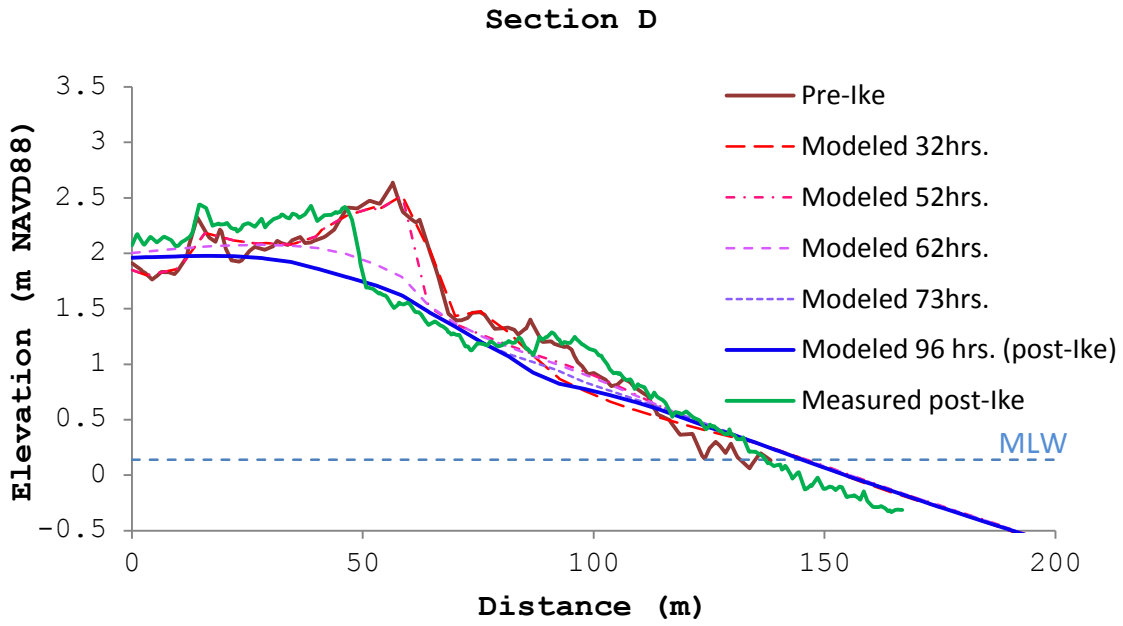

Figure 4.4: XBeach simulated bed level evolution compared to pre- and post-storm bed level extracted from LiDAR data at Section D (near the center of FI).

The Xbeach simulation was able to capture the large scale 2D erosional patterns of the island. The locations of two significant breaches (identified in Figure 1.8), were accurately reproduced with Xbeach (Figure 4.5). Both of these locations initially had a relatively low and narrow foredune, and thus were particularly susceptible to breaching. Although the large-scale erosion trends are accurately simulated in Xbeach, it is clear that the small-scale erosion patterns (such as the specific ebb channels) are not accurately reproduced. This is likely due to the influence of structures, vegetation, and spatially variable geology that are not included in the Xbeach model.

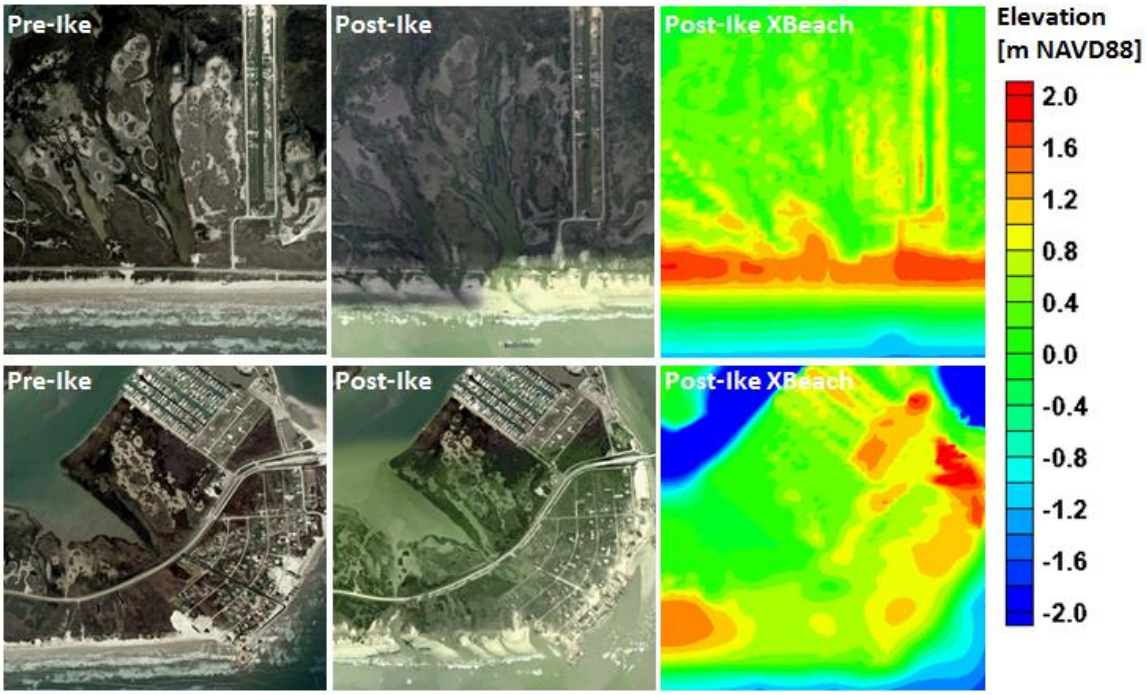

Figure 4.5: XBeach simulated erosion trends compared with LiDAR observations.

One way to quantify the accuracy of a model is to compare the error in modeled bed level change to the variance of the observed bed level change from LiDAR data. This can only be accurately calculated at points where the coverage of all data sources overlap. Thus the calculation of model skill is limited to the subaerial beach where LiDAR surveys are available. The bed level change observed from LiDAR surveys was interpolated onto the model grid, and all grid points lying outside the LiDAR coverage area were removed. Furthermore, since the first return was used in the pre-Ike LiDAR survey, and the second return was used in the post-Ike survey (Table 2.8), there were some areas of inconsistency in the LiDAR surveys. For example, the pre-Ike survey was based on the first LiDAR return signal, which included buildings, trees, and large groups of foliage while the post-Ike survey included only ground elevations from the second LiDAR return signal. To remedy this, the data were also filtered to exclude points where the elevation difference between LiDAR surveys was greater than +2 m (i.e. greater than

2 m accretion). The remaining points were used to calculate the model skill based on McCall et al. (2010) [27].

$$Skill = 1 - \frac{\sum_{i=1}^{N}\left(dz_{b_{LIDAR,i}} - dz_{b_{Model,i}}\right)^2}{\sum_{i=1}^{N}\left(dz_{b_{LIDAR,i}}\right)^2} \tag{4.1}$$

where N is the total number of grid points in the overlapping coverage area, $dz_{bModel,i}$ is the measured bed level change at point i, and $dz_{bLiDAR,i}$ is the modeled bed level change at point i. If the skill is equal to one, then the simulation perfectly predicts the bed level change. If the skill is zero, then the simulation is no more accurate than predicting zero bed level change. If the skill is less than zero, then the simulation is less accurate than predicting zero bed level change.

In addition to the model skill, it is also important to calculate the simulation bias to determine whether the simulation errors are due to random differences in bed elevation or due to a general trend. The simulation bias is calculated simply using the mean error, as shown in Equation 4.2.

$$Bias = \frac{1}{N}\sum_{i=1}^{N}\left(z_{b_{post-storm,Model,i}} - z_{b_{post-storm,LIDAR,i}}\right) \tag{4.2}$$

The bias represents the average difference in post-Ike bed elevations between the simulation and the LiDAR survey. A positive bias means the model has predicted a higher post-storm bed elevation than is observed, and a negative bias means the model has predicted a lower post-storm bed elevation.

Based on Equations 4.1 and 4.2 the skill of this XBeach simulation is 0.35 with an overall bias of -0.06. This is considerably lower than the skill of 0.74 from a similar study by McCall et al. (2010) [27]. There are a number of factors that could contribute to

this. Where the study by McCall et al. (2010) focused on a mostly unvegetated stretch of island, the back barrier of Follett's Island is abundantly covered with grass, which cannot be included in the current build of XBeach. Also, there are likely errors in the computed difference in the LiDAR surveys from the filtering of buildings and foliage.

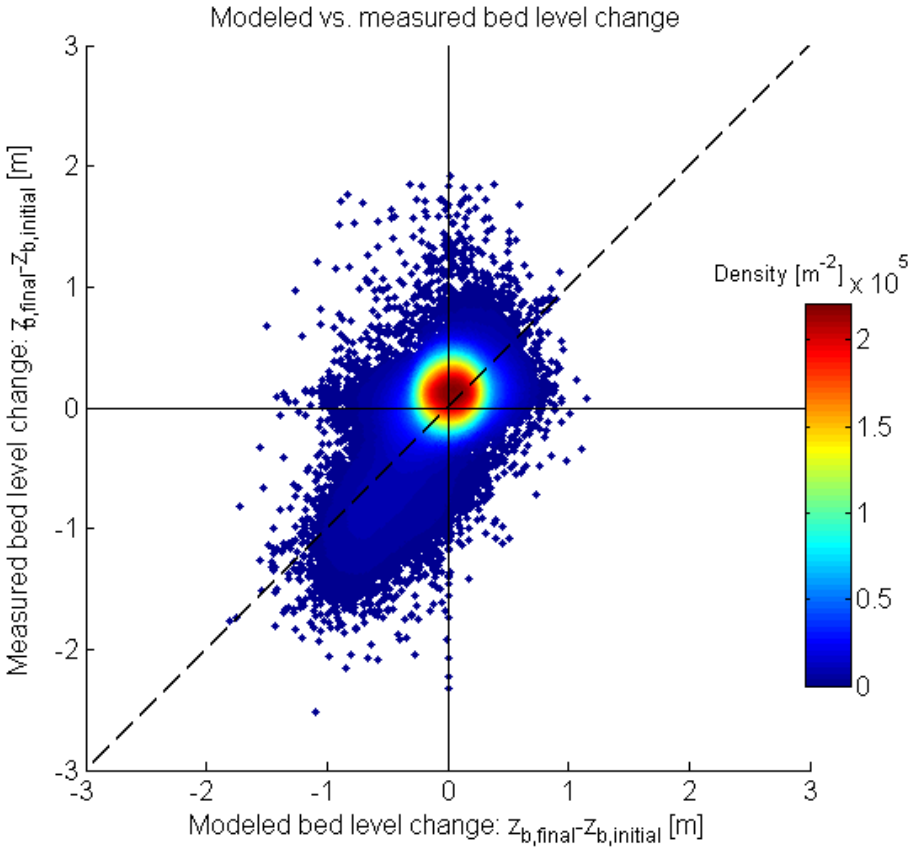

Figure 4.6: Measured bed level change vs. modeled bed level change for all grid points in overlapping coverage area. The dashed line represents a perfect 1:1 relation. Color scale indicates point density in points per square meter. Positive values represent accretion and negative values represent erosion.

The skill of this simulation is shown graphically in Figure 4.6, where the measured bed level change is plotted relative to the modeled bed level change. In this plot, each point represents one grid point in the overlapping coverage area. The color scale in this plot represents the point density in points per square meter, which in this context represents the density of points within one linear meter of both observed and modeled bed level change. It is clear from Figure 4.6 that the greatest density of measured bed change was between -5 cm and +30cm. Based on this figure, Xbeach also had a tendency to underestimate both accretional and erosional bed level change. There is also a cluster of points of measured bed level change greater than 1 m that were significantly underestimated by Xbeach. It is likely that these points are associated with the difference in LiDAR returns between the pre- and post-Ike surveys that were not filtered out.

4.2. CSHORE Simulation

CSHORE was run separately for the eight different bed profiles associated with Sections A-H. Run times for each profile were around 60 seconds. The model times associated with each regime closely matched those from the XBeach model, although they tended to vary for each section by up to five hours. For the sake of consistency in the analysis, the model times associated with each regime were the same as for the XBeach model: Collision regime for the first 32 hours, overwash regime from hour 32 to 52, inundation regime from hour 52 to 62, storm surge ebb from hour 62 to hour 73, and resurgence wave from hour 73 to hour 96. Figure 4.7 shows the bed level of Section D at the end of each regime. During the collision regime, minimal bed level change is experienced to the foredune, beach, and foreshore. During the overwash regime, the wave runup exceeds the dune crest causing washover of dune sediments and slight lowering of the dune crest (0.1 – 0.6 m). During the inundation regime, the beach is flattened and the shoreline is extended seaward while the dune is drastically lowered in elevation and pushed landward. There is very little bed level change associated with storm surge ebb and the resurgence wave since CSHORE does not model offshore directed return flow in its current build and the resurgence wave is not large enough to cause major morphological changes.

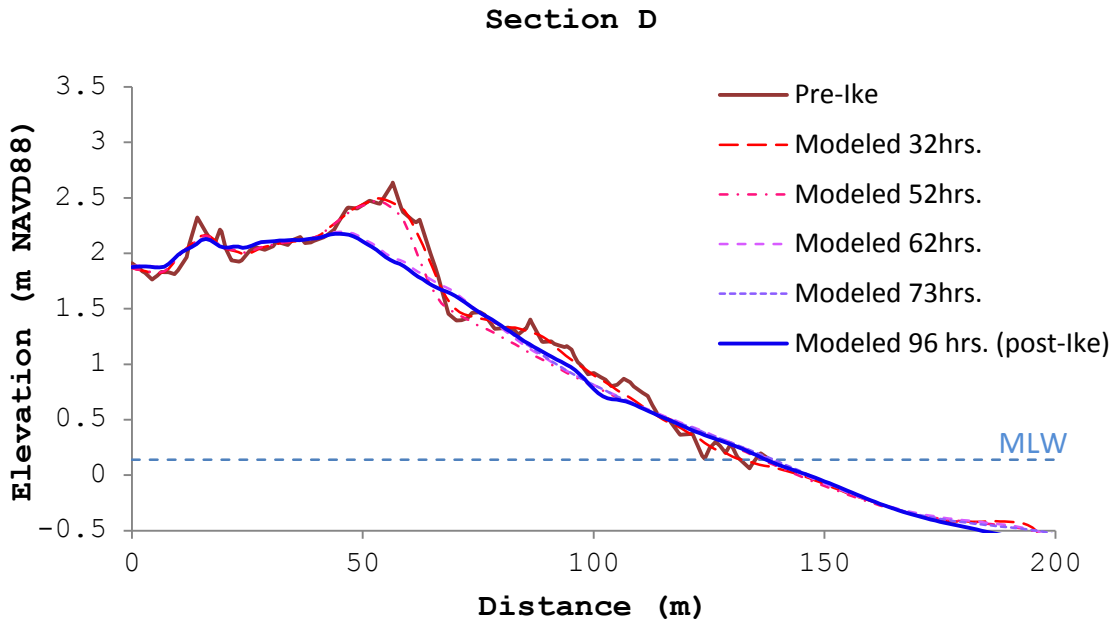

Figure 4.7: CSHORE simulated erosion and deposition at the end of the collision, overwash, and inundation regimes and at the end of the simulation.

Table 4.2 summarizes the volume accreted and eroded at the end of each regime. The bulk of the bed level change is associated with the overwash and inundation regimes. Erosion rates during the inundation regime are still higher than any other regime, but not proportionally as high as in the Xbeach model. Also unlike the XBeach model, the storm surge ebb regime does not have a significant impact on the total bed level change. This is understandable as the hydrodynamics associated with the ebbing storm surge are not built into the time-averaged CSHORE model.

Table 4.2: CSHORE simulated volume of accretion and erosion at Section-D at the end of the collision regime (32 hrs.), the overwash regime (52 hrs.), the inundation regime (62 hrs.), the storm surge ebb (73 hrs.), and at the end of the model (96 hrs.).

	Volume accreted [m^3/m]	Accretion rate [m^3/m-hr]	Volume eroded [m^3/m]	Erosion rate [m^3/m-hr]	Net volume change [m^3/m]
		+0.23		-0.23	
32 hrs.	+7.5		-7.3		+0.1
		+0.56		-0.54	
52 hrs.	+18.6		-18.1		+0.6
		+0.73		-0.59	
62 hrs.	+25.9		-24.0		+2.0
		+0.14		-0.12	
73 hrs.	+27.5		-25.3		+2.3
		+0.04		-0.03	
96 hrs.	+28.5		-26.1		+2.4

Simulated post-storm bed level profiles were compared with post-storm LiDAR profiles along Sections A-H (Figure 2.15). Sample profiles from Section A and Section D are shown in Figure 4.8 and Figure 4.9, respectively. Figures from all cross sections are included in Appendix E. Based on these figures it is clear that CSHORE very accurately predicts the post-storm beach slope and shoreline. However, CSHORE is less effective at predicting the morphology of the foredune. This is likely due to the fact that the dune morphodynamics is largely driven by sheet flow associated with surge overtopping and inundation; a physical process that is not included in the CSHORE model.

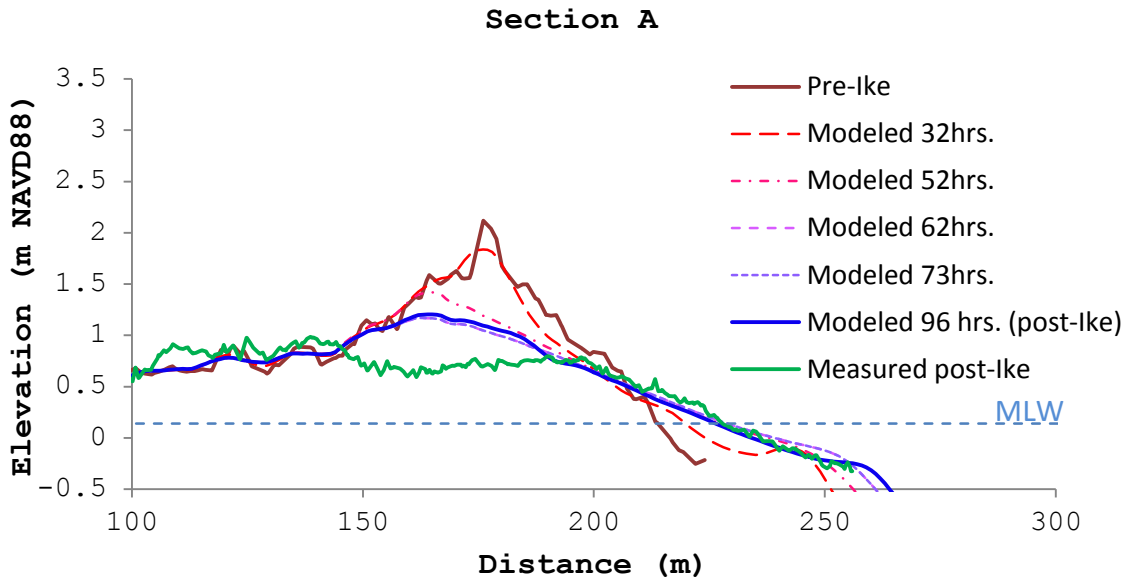

Figure 4.8: CSHORE simulated bed level evolution compared to pre- and post-storm bed level extracted from LiDAR data at Section A (the west end of FI).

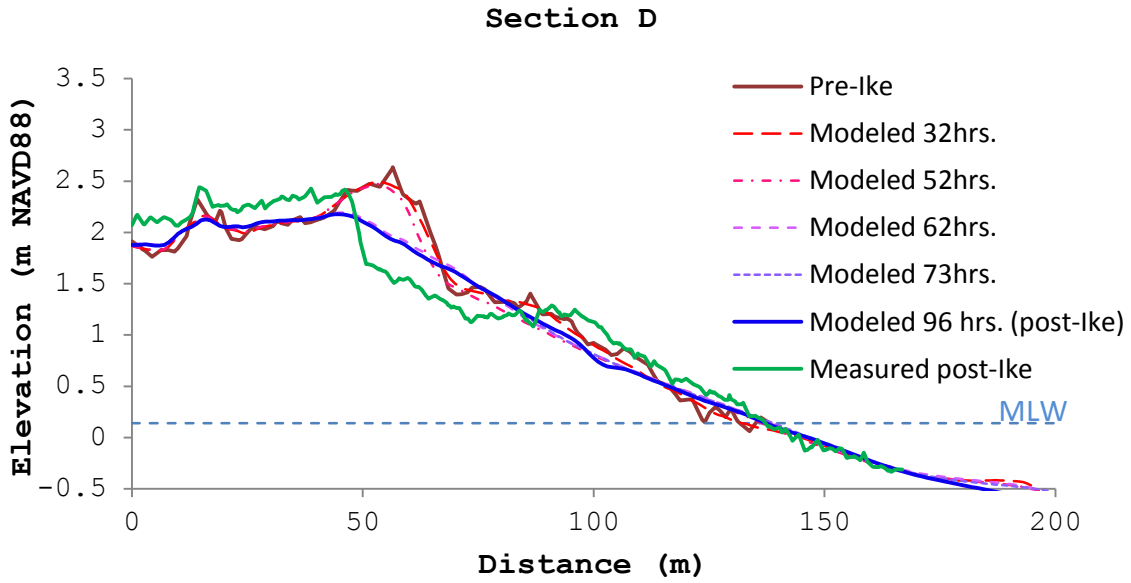

Figure 4.9: CSHORE simulated bed level evolution compared to pre- and post-storm bed level extracted from LiDAR data at Section D (near the center of FI).

The skill and bias of the CSHORE simulations (Equations 4.1 and 4.2) were calculated for each profile. This calculation is limited to the subaerial portion of the island where LiDAR data are available. Since Sections F-H are located on the more developed west end of the island, it is likely that anthropogenic influences contribute to the lower skill for these sections. Excluding Sections F-H, the skill becomes 0.408 and the bias 0.737. Sections B and C display a clear positive bias that is likely due to truncation of the domain at CR-257

Table 4.3: Skill and bias of CSHORE simulation for Sections A-H.

	Skill	Bias [m]
Section A	0.629	0.007
Section B	0.388	0.655
Section C	0.283	0.380
Section D	0.496	-0.051
Section E	0.413	-0.005
Section F	0.382	-0.038
Section G	0.087	-0.164
Section H	-0.109	-0.055
Total	0.345	0.170

To compare the skill of CSHORE directly with that of XBeach, the skill of each model must be calculated over the same coverage area. Since the CSHORE calculation is limited to cross-shore transects, the skill of XBeach on those same transects was calculated. Table 4.4, shows the skill and bias for the XBeach simulation on Sections A-H, for direct comparison with CSHORE results.

Table 4.4: Skill and bias of XBeach simulation for Sections A-H.

	Skill	Bias [m]
Section A	0.789	0.016
Section B	0.811	0.100
Section C	0.670	-0.069
Section D	0.326	-0.041
Section E	-0.109	-0.026
Section F	-0.374	-0.049
Section G	-0.040	-0.125
Section H	0.000	0.075
Total	0.491	0.002

The total skill of the CSHORE simulations was 0.35, approximately the same as the total skill of the Xbeach simulation. However, when evaluating the skill only on cross-shore Sections A-H, the skill of CSHORE was approximately 30% lower than Xbeach. In fact, on the east end of the island (Sections A & B), Xbeach showed skill as high as 0.81. However, near the center and east end of the island, CSHORE had a higher skill than XBeach. This is likely due to the fact that the resilient vegetation in that region prevented the dune from being completely eroded. Thus, the fact that CSHORE inherently underpredicts the lowering of the dune during the inundation regime coincidentally results in a better skill score at Sections D-F.

5. DISCUSSION AND CONCLUSIONS

In this study, the morphodynamics of the subaerial portion of Follett's Island, a low-lying, sediment-starved barrier island on the Upper Texas Coast, were examined in response to hydrodynamic forcing conditions from Hurricane Ike. In addition, five years of subaerial dune and beach recovery were analyzed using available topographic data. To summarize the contents of this study, first Section 1 provides an introduction to barrier islands as well as the setting specific to Follett's Island. Section 1 also provides some background information on Hurricane Ike. Section 2 describes the collection and analysis of existing data. This section includes the characterization of the metocean climate and analysis of LiDAR surveys along beach transects from pre- and post-storm conditions as well as for a 5 year recovery period. In Section 3, the coastal response models XBeach and CSHORE are introduced. This section includes an introduction to the model equations, development of the model domain, determination of the model forcing parameters and some sensitivity testing. Section 4 provides an analysis of simulation results from both coastal response models. This includes qualitative and quantitative analysis of bed level change during each storm impact regime and the calculation of model skill. The goal of this study is to address the following three research questions:

1) How did Hurricane Ike affect the sediment volume on the subaerial beach and foredune of Follett's Island?
2) What was the driving mechanism behind the recovery of the subaerial island following the hurricane?
3) What hydrodynamic processes were most significant to the morphological response of Follett's Island during the hurricane?

Hurricane Ike was one of the most destructive storms to ever hit the UTC. Although FI was on the western side of Ike's eye at landfall and thus subject to predominantly offshore directed winds, the resulting storm surge overtopped and inundated the island. During this process, complex hydrodynamic forcing associated with ocean-to-bay

directed overwash sheet flow and subsequent bay-to-ocean directed ebb sheet flow modified the morphology of FI drastically. In subsequent years, no overtopping events occurred and the subaerial portion of the island continued to recover.

Regarding the first research question, it is clear that Follett's Island ultimately benefitted from Hurricane Ike in terms of sediment supply and shoreline position. LiDAR surveys show that the storm resulted in a 25-30% net gain of sediment volume in the foredune and subaerial beach after five years of recovery. This is an unexpected finding since large storms typically result in a net loss in sediment volume. There was a net loss of sediment in the subaqueous shoreface; however limited bathymetric data restrict what can be concluded about the direct impact of Hurricane Ike on the shoreface. Although the dunes grew in volume and the shoreline advanced, this growth represents retention of less than 5% of the total sand lost from the subaqueous shoreface.

This appears to be a bit of a paradox; however it can be explained conceptually. The 12/2008 LIDAR survey shows that the foredunes were largely destroyed by Ike and that most of the subaerial portion was flattened. The LiDAR data also show washover deposits on the back barrier landward of the original foredune immediately after Ike. Based on an average of 46 cold fronts a year, there were between 200-250 cold fronts of varying intensities that passed through the area in the five years between Ike and the 2013 LIDAR survey. The washover deposits on the back-barrier would receive the brunt of the northern winds when the fronts pass, resulting in significant bay-towards-beach aeolian transport of sand.

Barrier islands along the northern Gulf of Mexico are oriented generally in an east-west to northeast-southwest orientation. As a result, the back bay areas are significantly impacted by northern fronts. Bay-to-barrier island transport, as part of the recovery of barrier islands from hurricane overwash, is rarely considered. This study demonstrates that bay-to-beach transport of sand during the recovery phase can not only build the foredunes back to pre-hurricane conditions, but can also build them up to larger than pre-hurricane conditions in spite of significant erosion of the shoreface.

In addition to this bay-towards-beach aeolian transport, large waves and onshore directed surge current during the hurricane could have transported sediment from the shoreface below the depth of closure into the foreshore, where seasonal waves could have then drawn this sediment ashore during the recovery phase. This could be concluded based on the observed retreat of the subaqueous shoreface. Perhaps equally likely is that strong wave action and storm surge currents in the San Luis Pass released sediment trapped in the tidal shoals back into the littoral system where seasonal waves and net westward sediment transport nourished the island over the subsequent recovery period. This was also suggested by Morton et al. (1994) [29]. Realistically, the answer to the second research question regarding the mechanism behind the subaerial island recovery is likely a combination of the bay-towards-beach aeolian transport and the release of sediment from the San Luis Pass tidal shoals.

Based on the model results shown in Section 4, it is clear that both Xbeach and CSHORE were able to reproduce the morphological response of Follett's Island to Hurricane Ike with varying degrees of skill. XBeach was more accurate at simulating the coastal response to the foredune and beach system, and was also able to capture 2D effects such as the locations of breaches. It also included model routines for calculating hydrodynamics and transport due to sheet flow; something that proved to be a major contributor to the overall response of the island. However, XBeach required a significantly longer run time than CSHORE, making it an impractical model choice for simulating large numbers of storms or design scenarios in future projects.

CSHORE was able to accurately calculate the post-storm slope and shoreline, however was less effective at simulating the response of the foredune. Furthermore, it does not include routines for sheet flow, making it an impractical model choice for scenarios where sheet flow is likely to be a major driver of the coastal response. CSHORE has further limitations on the model domain. In its current build, CSHORE is unable to simulate transport across a full cross-section of the island, from offshore to the back bay, and cannot capture 2D alongshore transport trends. Despite these limitations, CSHORE was able to simulate the response of FI with a skill as high as 0.61.

Finally, regarding the third research question regarding which hydrodynamic processes were most significant to the island's morphological response, both models show that the greatest change in bed level of Follett's Island was associated with the inundation regime of Hurricane Ike, which lasted only about 10 hours. During this regime, bed level change rates were up to three times greater than during the collision and overwash regimes. XBeach was also able to capture significant bed level change associated with storm surge ebb; something that had not been addressed in Sallenger's impact regimes [39].

These conclusions have significant implications for barrier island management. It is clear that sediment-starved barrier islands like Follett's Island require fundamentally different coastal management practices than other coastal systems. Follett's Island might not have experienced the same degree of recovery had a seawall been constructed; although the immediate impact to the island might have been mitigated. Perhaps, rather than creating elevated structures, such as seawalls and dikes to prevent overtopping, the dune system should be left in its natural state, as dune overtopping could be critical to the subaerial sediment supply of the island. Additionally, perhaps rather than awaiting a hurricane to replenish a barrier island's sediment supply, nourishment projects should be considered for the back barrier or for nearshore berms.

The fact that both XBeach and CSHORE were able to reasonably simulate the coastal response of FI to Hurricane Ike means that we now have powerful tools at our disposal for developing these coastal management strategies. It is clear that the morphology of barrier islands is fundamentally linked to storms, and these models can be used to simulate the impact of synthetic storms on the island. As part of future studies, these tools can be used to simulate smaller storms for which no dune overtopping occurs to determine the direct contribution of dune overwash to the overall morphology of the island. These models can also be used to test the efficacy of proposed designs such as seawalls, revetments, or nourishment projects. In any case, it is clear from this study that coastal management strategies for Follett's Island, and similar

sediment-starved barrier islands, must be carefully considered as traditional strategies have the potential to interfere with the island's natural nourishment system.

REFERENCES

[1] Anderson, John B. "The formation and future of the upper Texas coast." *College Station: Texas A&M Press, 163p* (2007).

[2] Berg, Robbie. "Tropical cyclone report: Hurricane Ike (AL092008), 1-14 September 2008." *National Hurricane Center* (2009).

[3] Blake, Eric S. "Tropical cyclone report: Hurricane Humberto (AL092007), 12-14 September 2007." *National Hurricane Center* (2007).

[4] Brown Jr, Thomas W., and Anwar Slitine. "Texas digital aerial photo archive project (TxDAPA)." *Texas Natural Resources Information Systems* (2003).

[5] Courant, Richard, Kurt Friedrichs, and Hans Lewy. "On the partial difference equations of mathematical physics." *IBM Journal of Research and Development* 11.2 (1967): 215-234.

[6] Dalrymple, Robert A. *Coastal processes with engineering applications*. Cambridge University Press, 2004.

[7] Doran, Kara S., et al. "Hurricane Ike: observations and analysis of coastal change." *U. S. Geological Survey* (2009).

[8] East, Jeffery W., Michael J. Turco, and Robert R. Mason. "Monitoring inland storm surge and flooding from Hurricane Ike in Texas and Louisiana, September 2008." *U. S. Geological Survey* (2008).

[9] Goda, Yoshimi. *Random seas and design of maritime structures*. World Scientific, 2010.

[10] Goff, John A., Mead A. Allison, and Sean PS Gulick. "Offshore transport of sediment during cyclonic storms: Hurricane Ike (2008), Texas Gulf Coast, USA." *Geology* 38.4 (2010): 351-354.

[11] Hayes, Miles O. "Hurricanes as geological agents, south Texas coast: geological notes." *AAPG Bulletin* 51.6 (1967): 937-942.

[12] Henry, W. K. "Some aspects of the fate of cold fronts in the Gulf of Mexico." *Monthly Weather Review* 107.8 (1979): 1078-1082.

[13] Hope, Mark E., et al. "Hindcast and validation of Hurricane Ike (2008) waves, forerunner, and storm surge." *Journal of Geophysical Research: Oceans* 118.9 (2013): 4424-4460.

[14] Johnson, Bradley D., Nobuhisa Kobayashi, and Mark B. Gravens. *Cross-Shore numerical model CSHORE for waves, currents, sediment transport and beach profile evolution*. No. ERDC/CHL-TR-12-22. Engineer Research and Development Center. Vicksburg, MS, 2012.

[15] Krammer, John C. "Largest rivers in the United States." *United States Geological Survey* (1990)

[16] Kennedy, Andrew B., Uriah Gravois, and Brian Zachry. "Observations of landfalling wave spectra during Hurricane Ike." *Journal of Waterway, Port, Coastal, and Ocean Engineering* 137.3 (2010): 142-145.

[17] Kennedy, Andrew B., et al. "Rapidly installed temporary gauging for hurricane waves and surge, and application to Hurricane Gustav." *Continental Shelf Research* 30.16 (2010): 1743-1752.

[18] Kennedy, Andrew B., et al. "Origin of the Hurricane Ike forerunner surge." *Geophysical Research Letters* 38.8 (2011).

[19] Kobayashi, Nobuhisa, Francisco J. de los Santos, and Peter G. Kearney. "Time-averaged probabilistic model for irregular wave runup on permeable slopes." *Journal of Waterway, Port, Coastal, and Ocean Engineering* 134.2 (2008): 88-96.

[20] Komar, Paul D. *Beach processes and sedimentation*. Prentice Hall, 1998.

[21] Leatherman, Stephen P. "Migration of Assateague Island, Maryland, by inlet and overwash processes." *Geology* 7.2 (1979): 104-107.

[22] Leatherman, Stephen P., Michael R. Rampino, and John E. Sanders. "Barrier island evolution in response to sea level rise; discussion and reply." *Journal of Sedimentary Research* 53.3 (1983): 1026-1033.

[23] Lindemer, C. A., et al. "Numerical simulation of a low-lying barrier island's morphological response to Hurricane Katrina." *Coastal Engineering* 57.11 (2010): 985-995.

[24] Mason, Curtis. *Hydraulics and stability of five Texas inlets*. No. CERC-MR-81-1. Coastal Engineering Research Center. Fort Belvoir, VA, 1981.

[25] Masselink, Gerhard. "Group bound long waves as a source of infragravity energy in the surf zone." *Continental Shelf Research* 15.13 (1995): 1525-1547.

[26] McCall, Robert T. “The longshore dimension in dune overwash modelling: development, verification and validation of XBeach.” Diss. TU Delft, Delft University of Technology, 2008.

[27] McCall, Robert T., et al. "Two-dimensional time dependent hurricane overwash and erosion modeling at Santa Rosa Island." *Coastal Engineering* 57.7 (2010): 668-683.

[28] Morton, Robert A., and Mary J. Pieper. "Shoreline changes in the vicinity of the Brazos River delta." *University of Texas, Bureau of Economic Geology, Geol Circ* (1975).

[29] Morton, Robert A., Jeffrey G. Paine, and James C. Gibeaut. "Stages and durations of post-storm beach recovery, southeastern Texas coast, USA." *Journal of Coastal Research* (1994): 884-908.

[30] Morton, Robert A., James C. Gibeaut, and Jeffrey G. Paine. "Meso-scale transfer of sand during and after storms: implications for prediction of shoreline movement." *Marine Geology* 126.1 (1995): 161-179.

[31] Paine, Jeffrey G., Sojan Mathew, and Tiffany Caudle. *Texas Gulf Shoreline Change Rates through 2007*. No. 10-041-000-3737. Bureau of Economic Geology. Austin, TX, 2011.

[32] Paine, Jeffrey G., Sojan Mathew, and Tiffany Caudle. "Historical shoreline change through 2007, Texas Gulf Coast: rates, contributing causes, and Holocene context." *Gulf Coast Association of Geological Societies Journal* 1 (2012): 13-26.

[33] Pajak, Mary Jean, and Stephen P. Leatherman. "The high water line as shoreline indicator." *Journal of Coastal Research* (2002): 329-337.

[34] Parker, Bruce, et al. "National VDatum–The implementation of a national vertical datum transformation database." *Proceeding from the US Hydro 2003 Conference*. 2003.

[35] Powell, Mark D., et al. "The HRD real-time hurricane wind analysis system." *Journal of Wind Engineering and Industrial Aerodynamics* 77 (1998): 53-64.

[36] Roelvink, Dano, et al. "Modelling storm impacts on beaches, dunes and barrier islands." *Coastal Engineering* 56.11 (2009): 1133-1152.

[37] Rosati, Julie Dean, and Gregory W. Stone. "Geomorphologic evolution of barrier islands along the northern US Gulf of Mexico and implications for engineering design in barrier restoration." *Journal of Coastal Research* (2009): 8-22.

[38] Roth, David. "Texas hurricane history." *National Weather Service, Camp Springs* (2010).

[39] Sallenger Jr, Asbury H. "Storm impact scale for barrier islands." *Journal of Coastal Research* (2000): 890-895.

[40] Seelig, William N., and Robert M. Sorensen. "Investigation of shoreline changes at Sargent Beach, Texas." *Texas A & M University, Coastal and Ocean Engineering Division* (1973).

[41] Soulsby, Richard. *Dynamics of marine sands: a manual for practical applications*. Thomas Telford, 1997.

[42] Stone, Gregory W., et al. "The importance of extratropical and tropical cyclones on the short-term evolution of barrier islands along the northern Gulf of Mexico, USA." *Marine Geology* 210.1 (2004): 63-78.

[43] Taylor, Lisa A., Barry W. Eakins, Kelly S. Carignan, Robin R. Warnken, Tatiana Sazonova, and David C. Schoolcraft. *Digital elevation model of Galveston, Texas: procedures, data sources and analysis*. No. NESDIS NGDC-12. National Geophysical Data Center. Boulder, CO, 2008.

[44] U.S. Army Corps of Engineers. *Coastal Engineering Manual. Engineer Manual 1110-2-1100*. U.S. Army Corps of Engineers, Washington, D.C., 2002 (in 6 volumes).

[45] Wallace, Davin J., John B. Anderson, and Rodrigo A. Fernández. "Transgressive ravinement versus depth of closure: a geological perspective from the upper Texas coast." *Journal of Coastal Research* 26.6 (2010): 1057-1067.

[46] Young, I. R. "Observations of the spectra of hurricane generated waves." *Ocean Engineering* 25.4 (1998): 261-276.

[47] Zervas, C. *Extreme water levels of the United States 1893–2010.* No. NOS CO-OPS 067. National Oceanographic and Atmospheric Administration. Silver Spring, MD, 2013.

[48] Zhang, Keqi, Bruce Douglas, and Stephen Leatherman. "Do Storms Cause Long-Term Beach Erosion along the US East Barrier Coast?" *Geology* 110.4 (2002): 493-502.

APPENDIX A

XBEACH FILES

Params.txt

```
%%%%%%%%%%%%%%%%%%%%%%%%%%%%%%%%%%%%%%%%%%%%%%%%%%%%%%%%%%%%%%%%%%%%%%%%%%%%%%%%
%%% XBeach parameter settings input file                                     %%%
%%%                                                                          %%%
%%% date:     10-Feb-2015 10:34:06                                           %%%
%%% function: xb_write_params                                                %%%
%%%%%%%%%%%%%%%%%%%%%%%%%%%%%%%%%%%%%%%%%%%%%%%%%%%%%%%%%%%%%%%%%%%%%%%%%%%%%%%%

%%% General %%%%%%%%%%%%%%%%%%%%%%%%%%%%%%%%%%%%%%%%%%%%%%%%%%%%%%%%%%%%%%%%%%%%


%%% Bed composition parameters %%%%%%%%%%%%%%%%%%%%%%%%%%%%%%%%%%%%%%%%%%%%%%%%%

rhos       = 2650
por        = 0.400000
D50        = 0.000151
D90        = 0.000187
sedcal     = 1

%%% Flow boundary condition parameters %%%%%%%%%%%%%%%%%%%%%%%%%%%%%%%%%%%%%%%%%

left       = 0
right      = 0
ARC        = 1
order      = 2

%%% Grid parameters %%%%%%%%%%%%%%%%%%%%%%%%%%%%%%%%%%%%%%%%%%%%%%%%%%%%%%%%%%%%

depfile      = bed.dep
posdwn       = -1
nx           = 400
ny           = 1013
alfa         = 0
vardx        = 1
xfile        = x.grd
yfile        = y.grd
xori         = 297034.03774591
yori         = 3217350.127388
thetamin     = -90
thetamax     = 90
dtheta       = 20

%%% Model time %%%%%%%%%%%%%%%%%%%%%%%%%%%%%%%%%%%%%%%%%%%%%%%%%%%%%%%%%%%%%%%%%

tstop        = 345600

%%% Morphology parameters %%%%%%%%%%%%%%%%%%%%%%%%%%%%%%%%%%%%%%%%%%%%%%%%%%%%%%

morfac       = 1
morstart     = 100
smax         = 1.5
struct       = 1
ne_layer     = nebed.dep

%%% Tide boundary conditions %%%%%%%%%%%%%%%%%%%%%%%%%%%%%%%%%%%%%%%%%%%%%%%%%%%

zsinitfile   = ini.dep
```

```
zs0file      = tide.txt
tideloc      = 4

%%% Wave boundary condition parameters %%%%%%%%%%%%%%%%%%%%%%%%%%%%%%%%%%%%%%%%%%%%

instat       = 41

%%% Wave-spectrum boundary condition parameters %%%%%%%%%%%%%%%%%%%%%%%%%%%%%%%%%%%%

bcfile       = waves.txt

%%% Output variables %%%%%%%%%%%%%%%%%%%%%%%%%%%%%%%%%%%%%%%%%%%%%%%%%%%%%%%%%%%%%%

tintm      = 3600
tintp      = 900
tintg      = 900
tstart     = 0

nglobalvar = 9
zs
zb
H
R
ue
ve
u
v
ccg

nmeanvar   = 0
```

waves.txt

```
0.6435 5.5628 244.1800      3.3000 10.00003600.0000     1.0000
0.6486 5.5443 243.8300      3.3000 10.00003600.0000     1.0000
0.6574 5.5273 243.5700      3.3000 10.00003600.0000     1.0000
0.6719 5.5109 243.3400      3.3000 10.00003600.0000     1.0000
0.6937 5.4934 243.2200      3.3000 10.00003600.0000     1.0000
0.7251 5.4709 243.2900      3.3000 10.00003600.0000     1.0000
0.7699 5.4205 243.5800      3.3000 10.00003600.0000     1.0000
0.8277 5.3337 244.1200      3.3000 10.00003600.0000     1.0000
0.8965 14.7580244.8800      3.3000 10.00003600.0000     1.0000
0.9741 14.7190245.8000      3.3000 10.00003600.0000     1.0000
1.0580 14.6860246.8800      3.3000 10.00003600.0000     1.0000
1.1455 14.6430248.0200      3.3000 10.00003600.0000     1.0000
1.2308 14.5940249.0500      3.3000 10.00003600.0000     1.0000
1.3087 14.5380250.0000      3.3000 10.00003600.0000     1.0000
1.3763 14.4750250.7800      3.3000 10.00003600.0000     1.0000
1.4343 14.4030251.4000      3.3000 10.00003600.0000     1.0000
1.4815 14.3280251.9700      3.3000 10.00003600.0000     1.0000
1.5222 14.2540252.4500      3.3000 10.00003600.0000     1.0000
1.5597 14.1970252.8400      3.3000 10.00003600.0000     1.0000
```

```
1.5960 14.1690253.2500      3.3000 10.00003600.0000     1.0000
1.6331 14.1770253.6700      3.3000 10.00003600.0000     1.0000
1.6703 14.2060254.1400      3.3000 10.00003600.0000     1.0000
1.7095 14.2430254.6200      3.3000 10.00003600.0000     1.0000
1.7495 14.2780255.1000      3.3000 10.00003600.0000     1.0000
1.7893 14.3150255.5900      3.3000 10.00003600.0000     1.0000
1.8287 14.3580256.1000      3.3000 10.00003600.0000     1.0000
1.8664 14.4090256.5900      3.3000 10.00003600.0000     1.0000
1.9039 14.4490257.0300      3.3000 10.00003600.0000     1.0000
1.9379 14.4770257.4200      3.3000 10.00003600.0000     1.0000
1.9689 14.4760257.7600      3.3000 10.00003600.0000     1.0000
1.9977 14.4550258.0300      3.3000 10.00003600.0000     1.0000
2.0224 14.4250258.2600      3.3000 10.00003600.0000     1.0000
2.0459 14.4040258.4100      3.3000 10.00003600.0000     1.0000
2.0694 14.4000258.5800      3.3000 10.00003600.0000     1.0000
2.0934 14.4390258.7800      3.3000 10.00003600.0000     1.0000
2.1196 14.5350259.0500      3.3000 10.00003600.0000     1.0000
2.1513 14.7080259.3500      3.3000 10.00003600.0000     1.0000
2.1882 14.9610259.6700      3.3000 10.00003600.0000     1.0000
2.2261 15.2700260.0300      3.3000 10.00003600.0000     1.0000
2.2627 15.5720260.3700      3.3000 10.00003600.0000     1.0000
2.2982 15.7020260.6300      3.3000 10.00003600.0000     1.0000
2.3314 15.7710260.8500      3.3000 10.00003600.0000     1.0000
2.3634 15.8160260.9800      3.3000 10.00003600.0000     1.0000
2.3981 15.8430261.0000      3.3000 10.00003600.0000     1.0000
2.4410 15.8610260.9300      3.3000 10.00003600.0000     1.0000
2.4962 15.8850260.7700      3.3000 10.00003600.0000     1.0000
2.5723 15.9200260.5100      3.3000 10.00003600.0000     1.0000
2.6669 15.9740260.3100      3.3000 10.00003600.0000     1.0000
2.7758 16.0370260.2700      3.3000 10.00003600.0000     1.0000
2.8825 16.1220260.5100      3.3000 10.00003600.0000     1.0000
2.9857 16.2010260.9400      3.3000 10.00003600.0000     1.0000
3.0927 16.2720260.9700      3.3000 10.00003600.0000     1.0000
3.2736 16.2920259.6200      3.3000 10.00003600.0000     1.0000
3.4839 16.3400256.2400      3.3000 10.00003600.0000     1.0000
3.6178 16.3080253.0800      3.3000 10.00003600.0000     1.0000
3.7383 16.1950251.5300      3.3000 10.00003600.0000     1.0000
3.8867 15.9770250.5700      3.3000 10.00003600.0000     1.0000
4.1508 15.4860247.8000      3.3000 10.00003600.0000     1.0000
4.2362 14.8340237.5300      3.3000 10.00003600.0000     1.0000
4.2428 14.5980168.1000      3.3000 10.00003600.0000     1.0000
4.2271 4.8639 106.1400      3.3000 10.00003600.0000     1.0000
```

```
4.0546 5.1027 54.66003.3000 10.00003600.0000     1.0000
4.1877 7.4691 358.5970      3.3000 10.00003600.0000     1.0000
4.0119 9.4023 337.6890      3.3000 10.00003600.0000     1.0000
3.7968 9.7521 330.6160      3.3000 10.00003600.0000     1.0000
3.6682 9.8822 326.2980      3.3000 10.00003600.0000     1.0000
3.5233 10.0300321.8580      3.3000 10.00003600.0000     1.0000
3.3221 10.0980317.0700      3.3000 10.00003600.0000     1.0000
3.1201 10.0380312.8720      3.3000 10.00003600.0000     1.0000
2.8913 9.9160 309.1210      3.3000 10.00003600.0000     1.0000
2.6758 9.7299 305.8580      3.3000 10.00003600.0000     1.0000
2.4780 9.4993 302.4680      3.3000 10.00003600.0000     1.0000
2.3297 9.3220 299.6890      3.3000 10.00003600.0000     1.0000
2.2097 9.1879 297.0200      3.3000 10.00003600.0000     1.0000
2.1143 9.0789 294.6900      3.3000 10.00003600.0000     1.0000
2.0317 8.9963 292.6600      3.3000 10.00003600.0000     1.0000
1.9567 8.9325 290.9400      3.3000 10.00003600.0000     1.0000
1.8901 8.8441 289.4800      3.3000 10.00003600.0000     1.0000
1.8347 8.7564 288.2400      3.3000 10.00003600.0000     1.0000
1.7939 8.7034 287.2200      3.3000 10.00003600.0000     1.0000
1.7627 8.6991 286.2600      3.3000 10.00003600.0000     1.0000
1.7302 8.8668 285.3900      3.3000 10.00003600.0000     1.0000
1.6952 9.6396 284.5900      3.3000 10.00003600.0000     1.0000
1.6584 9.5459 283.8200      3.3000 10.00003600.0000     1.0000
1.5193 9.4095 281.2300      3.3000 10.00003600.0000     1.0000
1.4435 9.2422 279.4100      3.3000 10.00003600.0000     1.0000
1.3905 9.0772 277.8100      3.3000 10.00003600.0000     1.0000
1.3501 8.9213 276.5200      3.3000 10.00003600.0000     1.0000
1.3160 8.7330 275.4300      3.3000 10.00003600.0000     1.0000
1.2867 8.5468 274.6100      3.3000 10.00003600.0000     1.0000
1.2579 8.4309 274.0600      3.3000 10.00003600.0000     1.0000
1.2290 8.3449 273.8400      3.3000 10.00003600.0000     1.0000
1.2019 8.2604 273.8000      3.3000 10.00003600.0000     1.0000
1.1759 8.1811 273.8100      3.3000 10.00003600.0000     1.0000
1.1507 8.0986 273.9000      3.3000 10.00003600.0000     1.0000
1.1241 8.0175 274.0400      3.3000 10.00003600.0000     1.0000
1.0969 7.8863 274.2700      3.3000 10.00003600.0000     1.0000
```

tide.txt

```
0.0000000E+00  0.0000000E+00 0.0000000E+00 0.0000000E+00 0.0000000E+00
3.6000000E+03  2.3218333E-02 2.3623333E-02 3.3333333E-02 6.8908333E-02
7.2000000E+03  5.1396667E-02 5.2926667E-02 6.6666667E-02 1.2783667E-01
```

1.0800000E+04	9.4455000E-02	9.6720000E-02	1.0000000E-01	1.7908500E-01
1.4400000E+04	1.5416000E-01	1.6046667E-01	1.6016000E-01	2.2532000E-01
1.8000000E+04	2.4893333E-01	2.5926667E-01	2.5502500E-01	2.7179167E-01
2.1600000E+04	3.9178000E-01	4.0229000E-01	3.9103000E-01	3.3289000E-01
2.5200000E+04	5.0930000E-01	5.1596000E-01	4.9712000E-01	3.5055000E-01
2.8800000E+04	6.2764000E-01	6.2520000E-01	6.0456000E-01	3.8330000E-01
3.2400000E+04	7.3206000E-01	7.2695000E-01	7.0371000E-01	4.3076000E-01
3.6000000E+04	8.1834000E-01	8.0723000E-01	7.8314000E-01	4.8570000E-01
3.9600000E+04	8.9187000E-01	8.8007000E-01	8.5493000E-01	5.4498000E-01
4.3200000E+04	9.3090000E-01	9.1638000E-01	8.9385000E-01	6.0686000E-01
4.6800000E+04	9.3988000E-01	9.2782000E-01	9.1647000E-01	6.6453000E-01
5.0400000E+04	9.1195000E-01	9.0017000E-01	8.9667000E-01	7.1591000E-01
5.4000000E+04	8.7103000E-01	8.6013000E-01	8.6541000E-01	7.5983000E-01
5.7600000E+04	8.0455000E-01	7.9358000E-01	8.1689000E-01	7.9225000E-01
6.1200000E+04	7.3197000E-01	7.2431000E-01	7.4913000E-01	8.0831000E-01
6.4800000E+04	6.6047000E-01	6.4872000E-01	6.7604000E-01	8.0734000E-01
6.8400000E+04	5.9697000E-01	5.8813000E-01	6.1741000E-01	7.9978000E-01
7.2000000E+04	5.3750000E-01	5.2344000E-01	5.5146000E-01	7.8604000E-01
7.5600000E+04	4.8039000E-01	4.6889000E-01	4.9968000E-01	7.7131000E-01
7.9200000E+04	4.3075000E-01	4.1704000E-01	4.4818000E-01	7.5525000E-01
8.2800000E+04	3.9043000E-01	3.8058000E-01	4.0748000E-01	7.3719000E-01
8.6400000E+04	3.6228000E-01	3.5556000E-01	3.8709000E-01	7.1704000E-01
9.0000000E+04	3.4405000E-01	3.4666000E-01	3.6974000E-01	6.9272000E-01
9.3600000E+04	3.4532000E-01	3.4690000E-01	3.7324000E-01	6.6740000E-01
9.7200000E+04	3.7364000E-01	3.8405000E-01	4.0145000E-01	6.4299000E-01
1.0080000E+05	4.2426000E-01	4.2802000E-01	4.3975000E-01	6.2368000E-01
1.0440000E+05	4.9408000E-01	5.1080000E-01	5.0955000E-01	6.1093000E-01
1.0800000E+05	6.1617000E-01	6.2127000E-01	6.1381000E-01	6.2049000E-01
1.1160000E+05	7.4090000E-01	7.4626000E-01	7.2363000E-01	6.4715000E-01
1.1520000E+05	8.9129000E-01	8.8852000E-01	8.6764000E-01	6.9045000E-01
1.1880000E+05	1.0376000E+00	1.0299000E+00	9.8935000E-01	7.4456000E-01
1.2240000E+05	1.1617000E+00	1.1531000E+00	1.1077000E+00	8.0909000E-01
1.2600000E+05	1.2590000E+00	1.2376000E+00	1.1987000E+00	8.8137000E-01
1.2960000E+05	1.3325000E+00	1.3020000E+00	1.2717000E+00	9.6202000E-01
1.3320000E+05	1.3736000E+00	1.3428000E+00	1.3207000E+00	1.0423000E+00
1.3680000E+05	1.3886000E+00	1.3541000E+00	1.3490000E+00	1.1188000E+00
1.4040000E+05	1.3603000E+00	1.3298000E+00	1.3359000E+00	1.1821000E+00
1.4400000E+05	1.3400000E+00	1.2881000E+00	1.3198000E+00	1.2367000E+00
1.4760000E+05	1.3014000E+00	1.2501000E+00	1.2913000E+00	1.2785000E+00
1.5120000E+05	1.2650000E+00	1.2113000E+00	1.2607000E+00	1.3140000E+00
1.5480000E+05	1.2404000E+00	1.1805000E+00	1.2355000E+00	1.3397000E+00
1.5840000E+05	1.2300000E+00	1.1603000E+00	1.2165000E+00	1.3551000E+00

1.6200000E+05 1.2064000E+00 1.1342000E+00 1.1898000E+00 1.3638000E+00
1.6560000E+05 1.2150000E+00 1.1300000E+00 1.1866000E+00 1.3764000E+00
1.6920000E+05 1.2342000E+00 1.1420000E+00 1.1903000E+00 1.3898000E+00
1.7280000E+05 1.3096000E+00 1.1922000E+00 1.2433000E+00 1.4183000E+00
1.7640000E+05 1.3445000E+00 1.2243000E+00 1.2839000E+00 1.4511000E+00
1.8000000E+05 1.3728000E+00 1.2490000E+00 1.3071000E+00 1.4747000E+00
1.8360000E+05 1.2883000E+00 1.2032000E+00 1.2521000E+00 1.4865000E+00
1.8720000E+05 1.3444000E+00 1.2705000E+00 1.2509000E+00 1.5210000E+00
1.9080000E+05 1.3077000E+00 1.2282000E+00 1.2792000E+00 1.5674000E+00
1.9440000E+05 1.4905000E+00 1.3418000E+00 1.4231000E+00 1.6186000E+00
1.9800000E+05 1.7329000E+00 1.5593000E+00 1.5305000E+00 1.6837000E+00
2.0160000E+05 1.9618000E+00 1.8114000E+00 1.8069000E+00 1.8021000E+00
2.0520000E+05 2.3283000E+00 1.9676000E+00 2.0803000E+00 2.0513000E+00
2.0880000E+05 2.4218000E+00 1.9163000E+00 2.0108000E+00 2.2264000E+00
2.1240000E+05 2.4589000E+00 1.9449000E+00 1.7585000E+00 2.3266000E+00
2.1600000E+05 2.6902000E+00 1.9586000E+00 1.7258000E+00 2.3379000E+00
2.1960000E+05 2.8173000E+00 2.0603000E+00 1.9519000E+00 2.3199000E+00
2.2320000E+05 2.7084000E+00 2.1421000E+00 2.0126000E+00 2.2706000E+00
2.2680000E+05 2.4104000E+00 1.9846000E+00 1.9485000E+00 2.1004000E+00
2.3040000E+05 2.2464000E+00 2.0731000E+00 2.0393000E+00 2.1780000E+00
2.3400000E+05 2.0682000E+00 1.9035000E+00 1.9827000E+00 2.2662000E+00
2.3760000E+05 1.8051000E+00 1.7270000E+00 1.8203000E+00 2.2248000E+00
2.4120000E+05 1.3927000E+00 1.3610000E+00 1.5449000E+00 2.1197000E+00
2.4480000E+05 1.0699000E+00 1.0846000E+00 1.2674000E+00 2.0187000E+00
2.4840000E+05 8.5234000E-01 8.9797000E-01 1.0426000E+00 1.9358000E+00
2.5200000E+05 7.4286000E-01 8.2096000E-01 9.4964000E-01 1.8593000E+00
2.5560000E+05 6.6548000E-01 7.1895000E-01 8.5207000E-01 1.7774000E+00
2.5920000E+05 5.1455000E-01 5.2304000E-01 6.9851000E-01 1.6900000E+00
2.6280000E+05 3.6811000E-01 4.0152000E-01 5.3526000E-01 1.6000000E+00
2.6640000E+05 3.0489000E-01 3.2562000E-01 4.2546000E-01 1.5129000E+00
2.7000000E+05 2.5970000E-01 2.6635000E-01 3.8936000E-01 1.4308000E+00
2.7360000E+05 1.4674000E-01 1.5426000E-01 2.9022000E-01 1.3496000E+00
2.7720000E+05 2.7191000E-02 7.4091000E-02 2.0000000E-01 1.2700000E+00
2.8080000E+05 -4.0473000E-02   8.5540000E-03 2.0000000E-01 1.1947000E+00
2.8440000E+05 -4.8413000E-02   7.5226000E-03 2.0000000E-01 1.1255000E+00
2.8800000E+05 3.0580000E-02 2.8066000E-02 2.0000000E-01 1.0625000E+00
2.9160000E+05 1.6210000E-01 1.4404000E-01 2.0000000E-01 1.0043000E+00
2.9520000E+05 3.9826000E-01 3.3063000E-01 3.7718000E-01 9.5721000E-01
2.9880000E+05 6.0956000E-01 5.0272000E-01 5.1515000E-01 9.1999000E-01
3.0240000E+05 7.3528000E-01 6.3752000E-01 6.6234000E-01 9.1030000E-01
3.0600000E+05 7.7632000E-01 7.0572000E-01 7.1243000E-01 8.9304000E-01
3.0960000E+05 7.3982000E-01 6.5793000E-01 6.6598000E-01 8.8649000E-01

3.1320000E+05	7.0766000E-01	6.5658000E-01	6.9348000E-01	8.8833000E-01
3.1680000E+05	7.0002000E-01	6.5853000E-01	6.8079000E-01	8.8626000E-01
3.2040000E+05	7.0039000E-01	6.6581000E-01	6.8612000E-01	8.8102000E-01
3.2400000E+05	7.1068000E-01	6.5322000E-01	6.8236000E-01	8.6704000E-01
3.2760000E+05	6.9661000E-01	6.3416000E-01	6.5126000E-01	8.4433000E-01
3.3120000E+05	7.1454000E-01	6.6374000E-01	6.5666000E-01	8.2131000E-01
3.3480000E+05	7.4563000E-01	6.8628000E-01	6.7490000E-01	8.1078000E-01
3.3840000E+05	7.7993000E-01	7.2074000E-01	7.2579000E-01	8.1280000E-01
3.4200000E+05	7.8719000E-01	7.0831000E-01	7.2298000E-01	8.1970000E-01
3.4560000E+05	7.7922000E-01	7.0788000E-01	7.1845000E-01	8.2583000E-01

APPENDIX B

SAMPLE CSHORE RUN CODE (MATLAB)

```
clear all
close all
%% USER INPUT
prof = load('PROFILE_SMSExtractA.txt');
Section = 1;
Domainadd = 20; %in meters

%% ROUTINE
curdir = pwd;

% script params
iplotbc     = 0;                % 1 to plot the applied boundary
conditions
iplotmorpho = 1;                % 1 to plot the computed morphology
results
iplothydro  = 1;                % 1 to plot the computed hydrodynamic
results
iplotrunup  = 1;                % 1 to plot the computed runup
position
isave       = 0;                % 1 to save the computed results

% CSHORE execution and physical params
in.header = {'------------------------------------------------------'
             'CSHORE applied to idealized planar slope'
             '------------------------------------------------------'};
in.iline  = 1;       % 1 = single line
in.iprofl = 1;       % 0 = no morph, 1 = run morph
in.isedav = 1;       % 0 = unlimited sand, 1 = hard bottom
in.iperm  = 0;       % 0 = no permeability, 1 = permeable
in.iover  = 1;       % 0 = no overtopping , 1 = include overtopping
in.infilt = 0;       % 1 = include infiltration landward of dune crest
in.iwtran = 0;       % 0 = no standing water landward of crest,
                     % 1 = wave transmission due to overtopping
in.ipond  = 0;       % 0 = no ponding seaward of SWL
in.iwcint = 1;       % 0 = no W & C interaction , 1 = include W & C
interaction
in.iroll  = 1;       % 0 = no roller, 1 = roller
in.iwind  = 0;       % 0 = no wind effect
in.itide  = 0;       % 0 = no tidal effect on currents
in.dx     = 1;       % constant dx
in.gamma  = .8;      % shallow water ratio of wave height to water
depth
in.sporo  = 0.4;     % sediment porosity
in.d50 = .3;         % d_50 in mm
in.wf = vfall(in.d50,20,0); % fall velocity
in.sg = 2.65;        % specific gravity
in.effb   = 0.005;   % suspension efficiency due to breaking eB
in.efff   = 0.01;    % suspension efficiency due to friction ef
```

```
in.slp    = .5;      % suspended load parameter
in.slpot  = .1;     % overtopping suspended load parameter
in.tanphi = .630;    % tangent (sediment friction angle)
in.blp    = 0.001;   % bedload parameter
in.rwh = .02;        % numerical rununp wire height
in.ilab = 0;         % controls the boundary condition timing. Don't
change
in.fric_fac = .015;  % bottom friction factor

% boundary conditions and timing
cd ..
WAVES_table = load('waves.txt');
WSEL_table = load('tide.txt');
LinearInterpPts = load('LinearInterpPts.txt');
interpfac = LinearInterpPts(Section)/LinearInterpPts(end);
cd(curdir);

WSEL = (WSEL_table(:,2)-WSEL_table(:,3))*(1-interpfac)+WSEL_table(:,3);
angle = 270-WAVES_table(:,3)';
angle(angle>80)=80;
angle(angle<-80)=-80;

ftime = WSEL_table(end,1);      % [sec] final time, dictates model
duration
dt = WAVES_table(1,6);         % time interval in seconds for wave and
water level conditions
if in.ilab==1;
  in.timebc_wave = [dt/2:dt:ftime];
else
  in.timebc_wave = [0:dt:ftime];
end
in.timebc_surg = in.timebc_wave;
in.nwave = length(in.timebc_wave); in.nsurg = in.nwave;dum =
ones(1,in.nwave);
in.Tp = WAVES_table(:,2)';% spectral peak period in seconds
in.Hrms = WAVES_table(:,1)'/1.416;
in.Wsetup = 0*(dum+1);   % wave setup at seaward boundary in meters
in.swlbc = WSEL';% water level at seaward boundary in meters
in.angle = angle;%incident wave angle at seaward boundary in

% Numerical Tank
x_0 = prof(:,1);
x_0 = flipud(x_0(end)-x_0);
x_0 = vertcat(x_0,x_0(end)+Domainadd);
z_0 = flipud(prof(:,2));
z_0 = vertcat(z_0,z_0(end));
xend = floor(x_0(end)/in.dx)*in.dx;
x = [0:in.dx:xend];
z_interp = interp1(x_0,z_0,x);

%%%%% TEST%%%%%
z_interp(end)=5;
%%%%%%%%%%%%%%%
```

```
in.x = x;
in.zb = z_interp;
in.fw = in.fric_fac*ones(size(in.zb)); % cross-shore values of bot fric

in.xp = xend;


%%%%%%%%%%%%%%%%%%%%%%%%%%%%%%%%run cshore%%%%%%%%%%%%%%%%%%%%%
makeinfile_CH(in);
if isunix
  ! ./clean
  !../code/cshore_usace_linux.out >scr.txt
else
  !..\code\cshore_usace_win.out
end

%% Precess Results
results = load_results_CH;
X = results.morpho(end).x;
ZB = results.morpho(end).zb;

X=X(1:end-Domainadd);
ZB=ZB(1:end-Domainadd);
ZB=flipud(ZB);
clear results

save(curdir,'X','ZB');
```

APPENDIX C

SECTION PLOTS OF LIDAR DATA (2006-2013)

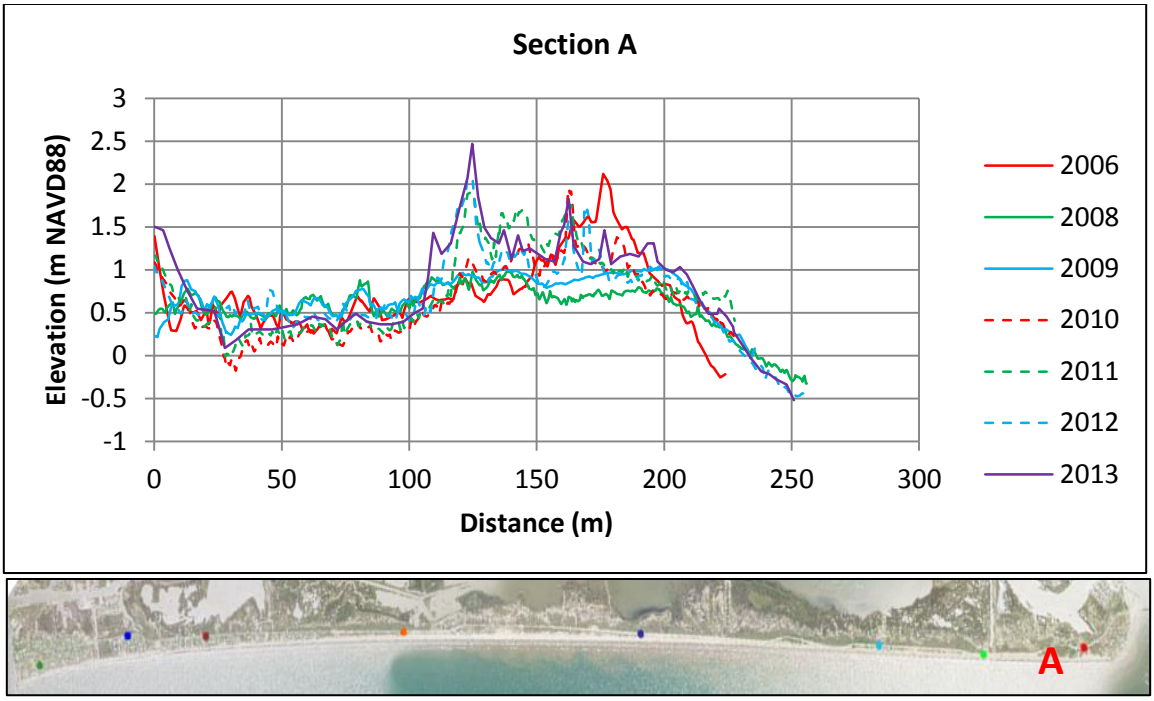

Figure C.1: Elevation profiles documenting the impact of Hurricane Ike to the foredune and beach as well as the subsequent recovery period at Section A. Cross-shore distance is positive offshore with zero at CR-257.

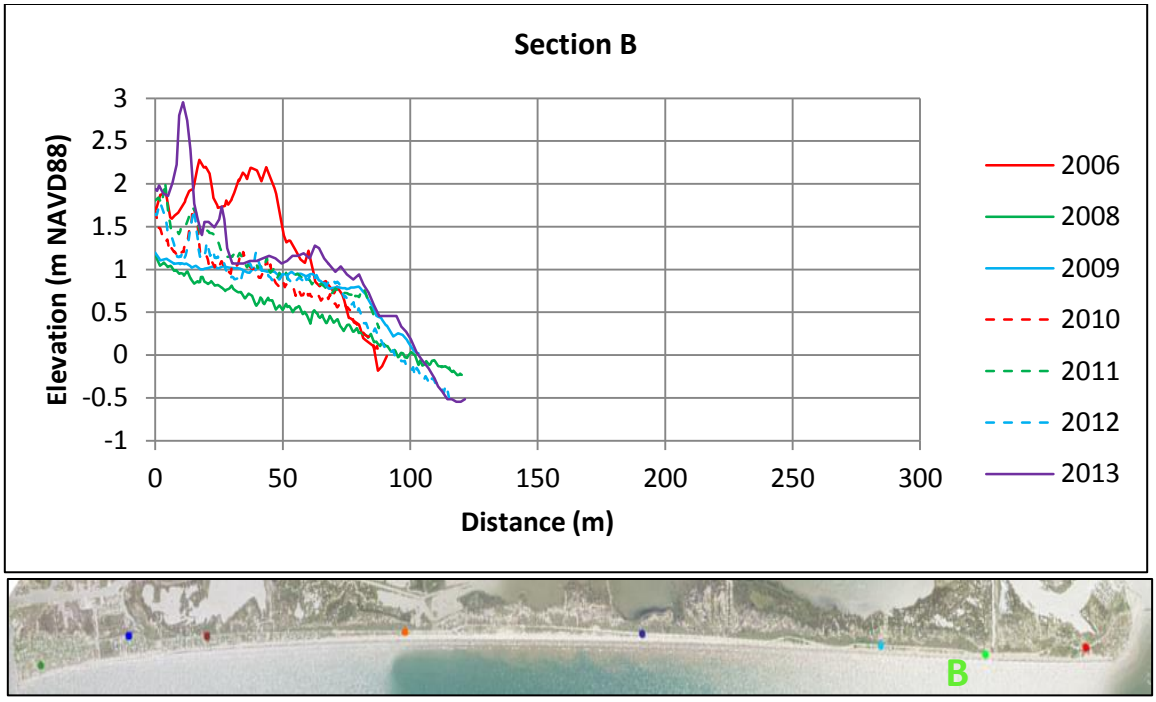

Figure C.2: Elevation profiles documenting the impact of Hurricane Ike to the foredune and beach as well as the subsequent recovery period at Section B. Cross-shore distance is positive offshore with zero at CR-257.

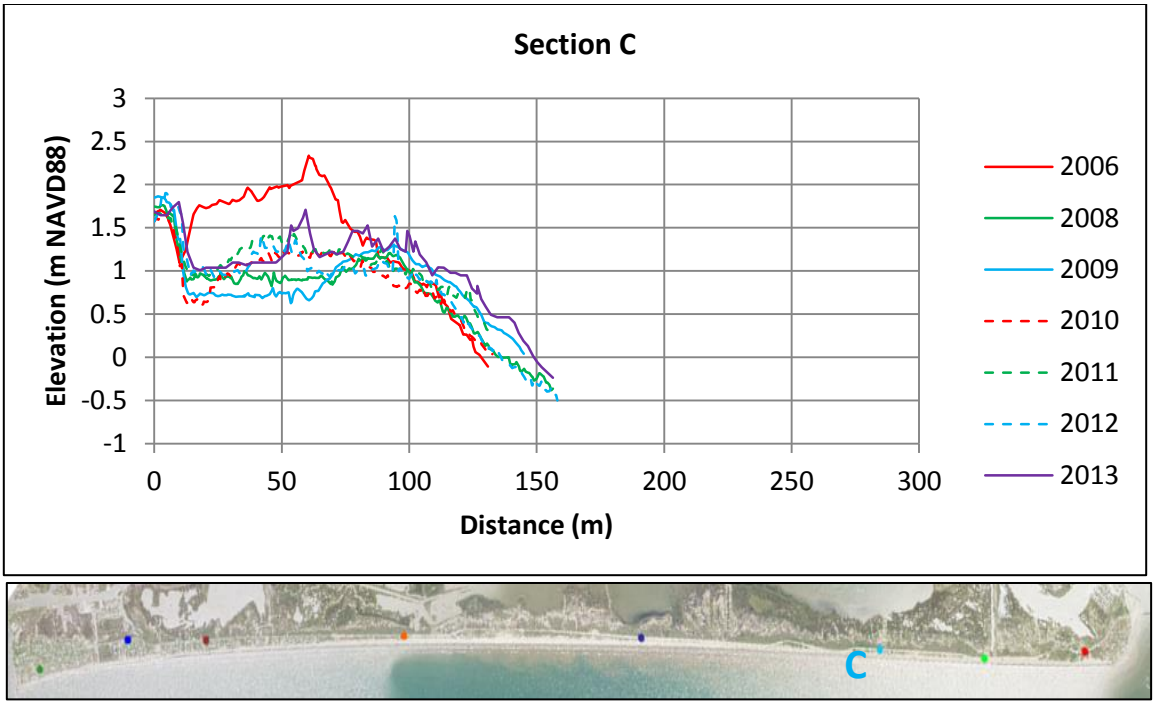

Figure C.3: Elevation profiles documenting the impact of Hurricane Ike to the foredune and beach as well as the subsequent recovery period at Section C. Cross-shore distance is positive offshore with zero at CR-257.

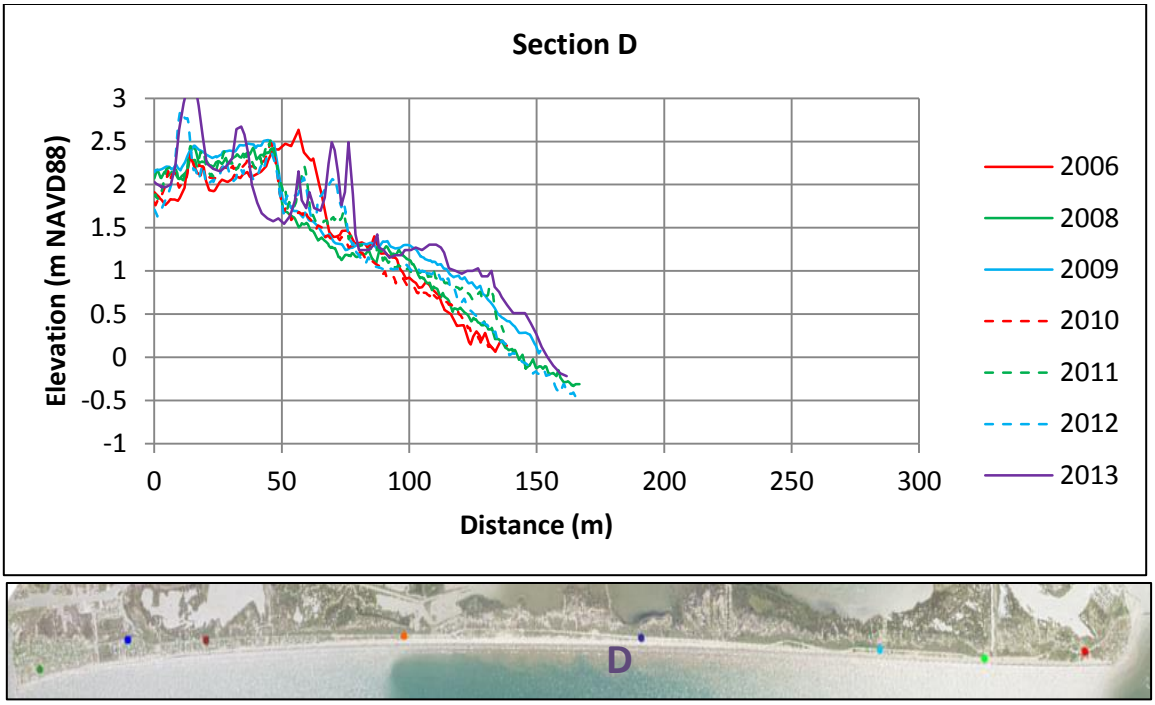

Figure C.4: Elevation profiles documenting the impact of Hurricane Ike to the foredune and beach as well as the subsequent recovery period at Section D. Cross-shore distance is positive offshore with zero at CR-257.

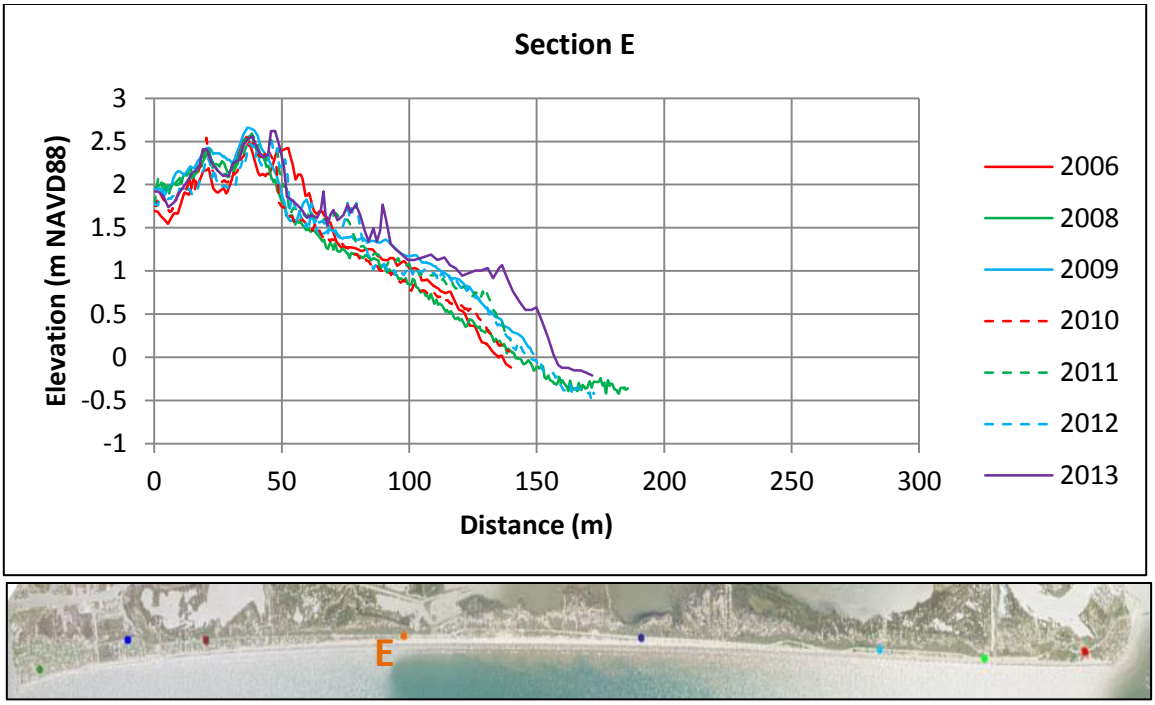

Figure C.5: Elevation profiles documenting the impact of Hurricane Ike to the foredune and beach as well as the subsequent recovery period at Section E. Cross-shore distance is positive offshore with zero at CR-257.

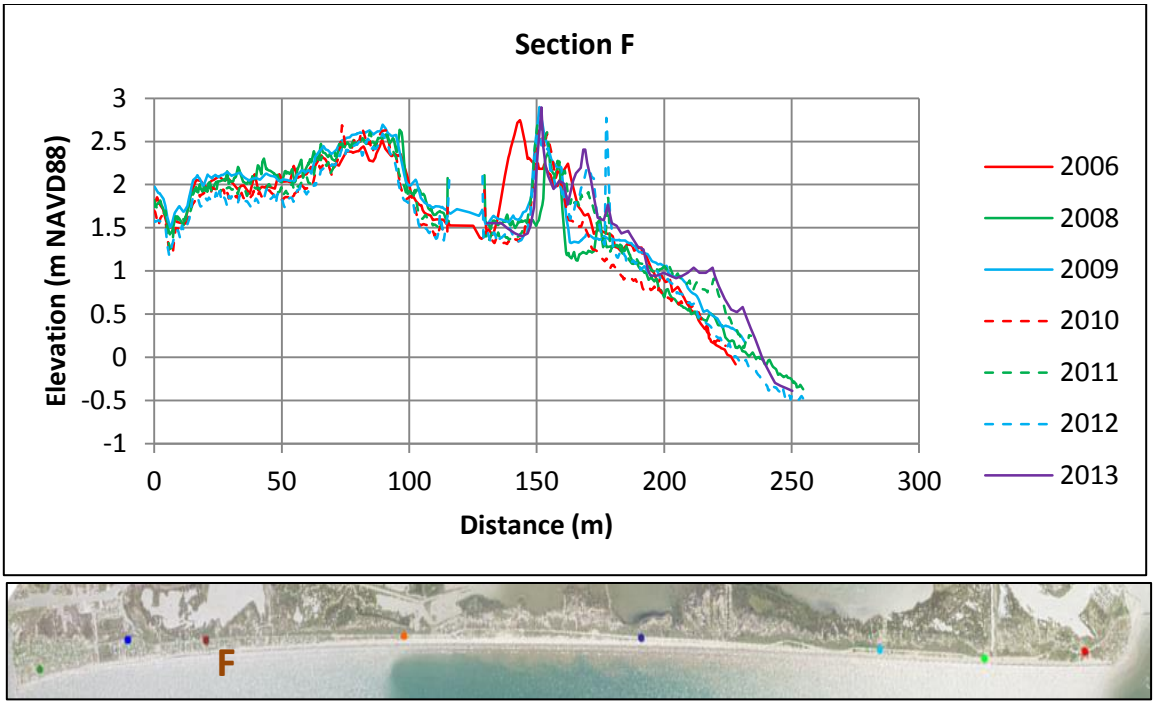

Figure C.6: Elevation profiles documenting the impact of Hurricane Ike to the foredune and beach as well as the subsequent recovery period at Section F. Cross-shore distance is positive offshore with zero at CR-257.

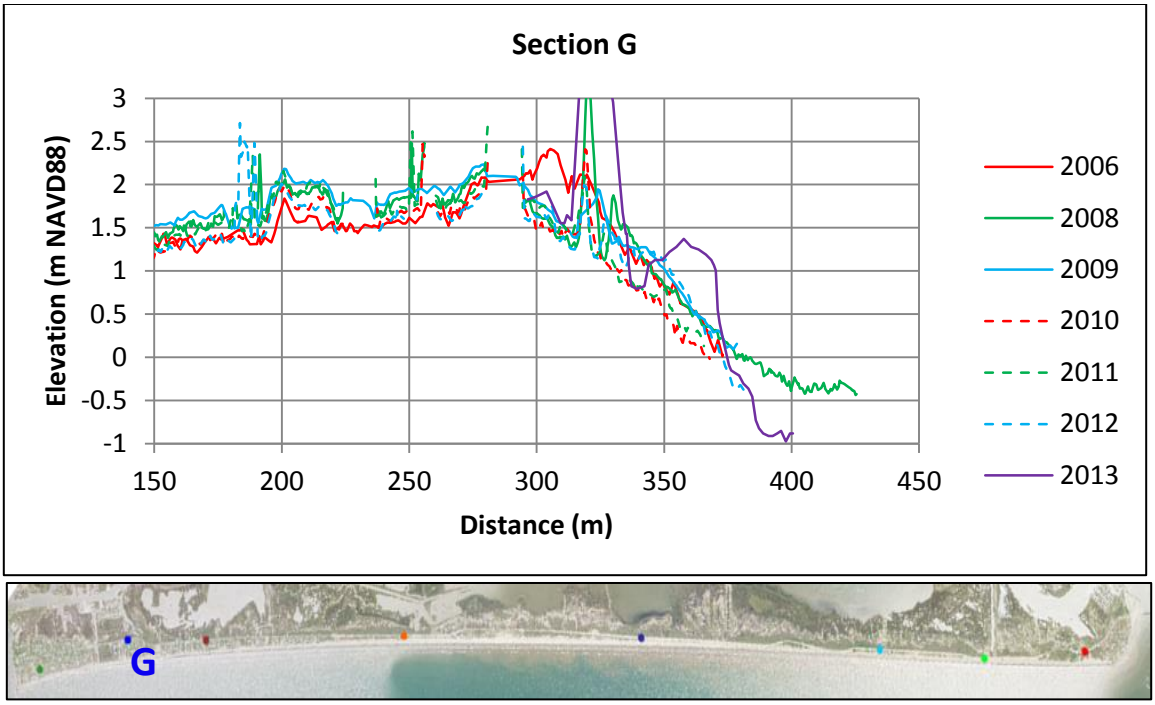

Figure C.7: Elevation profiles documenting the impact of Hurricane Ike to the foredune and beach as well as the subsequent recovery period at Section G. Cross-shore distance is positive offshore with zero at CR-257.

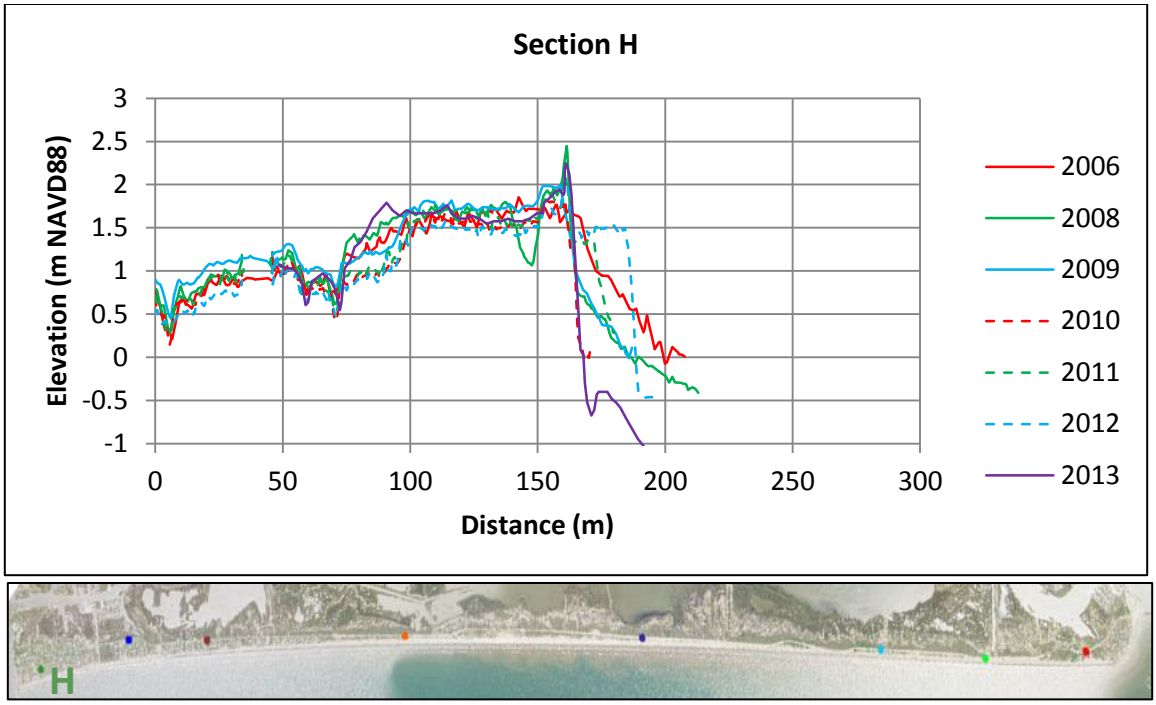

Figure C.8: Elevation profiles documenting the impact of Hurricane Ike to the foredune and beach as well as the subsequent recovery period at Section H. Cross-shore distance is positive offshore with zero at CR-257.

APPENDIX D

SECTION PLOTS OF XBEACH MODEL RESULTS

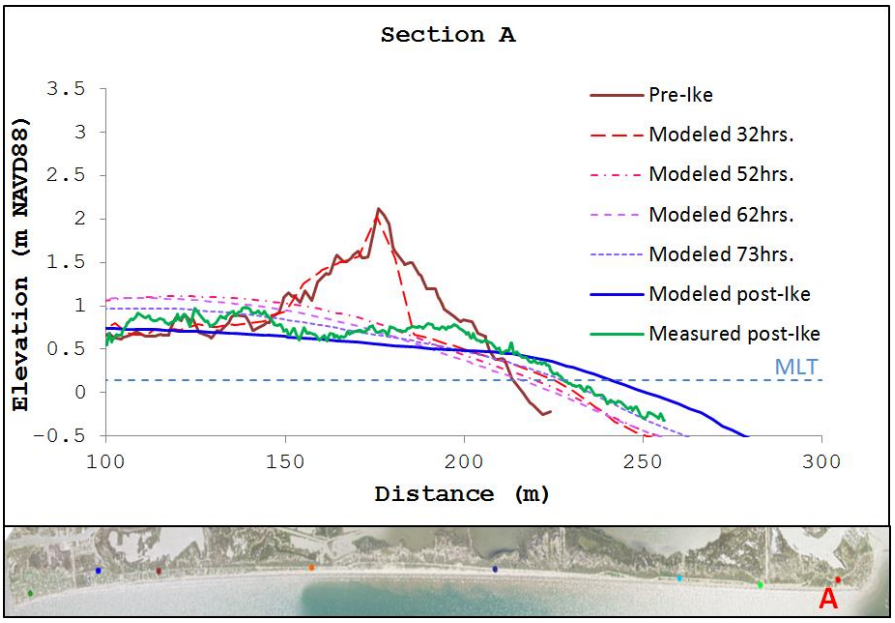

Figure D.1: XBeach simulated bed level evolution compared to pre- and post-storm bed level extracted from LiDAR data at Section A.

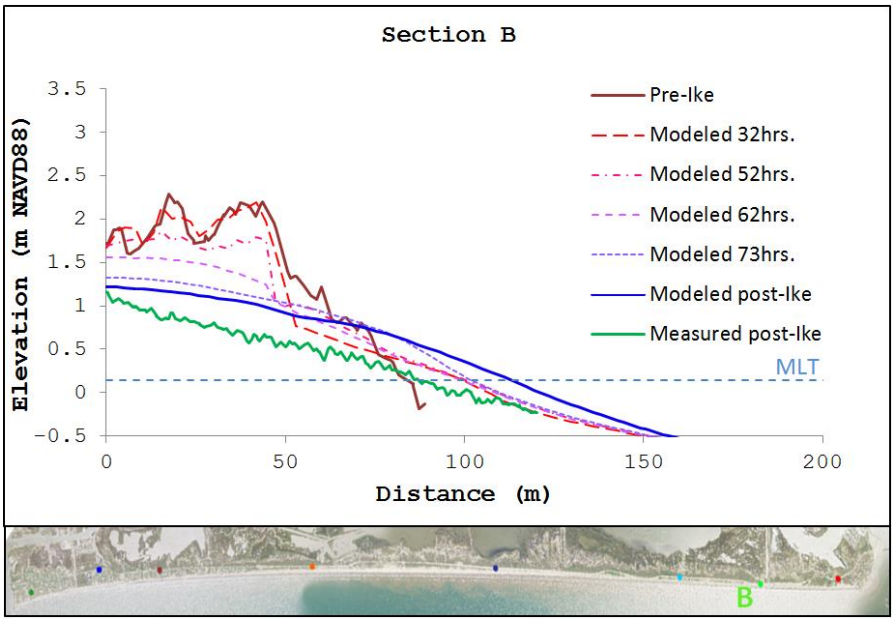

Figure D.2: XBeach simulated bed level evolution compared to pre- and post-storm bed level extracted from LiDAR data at Section B.

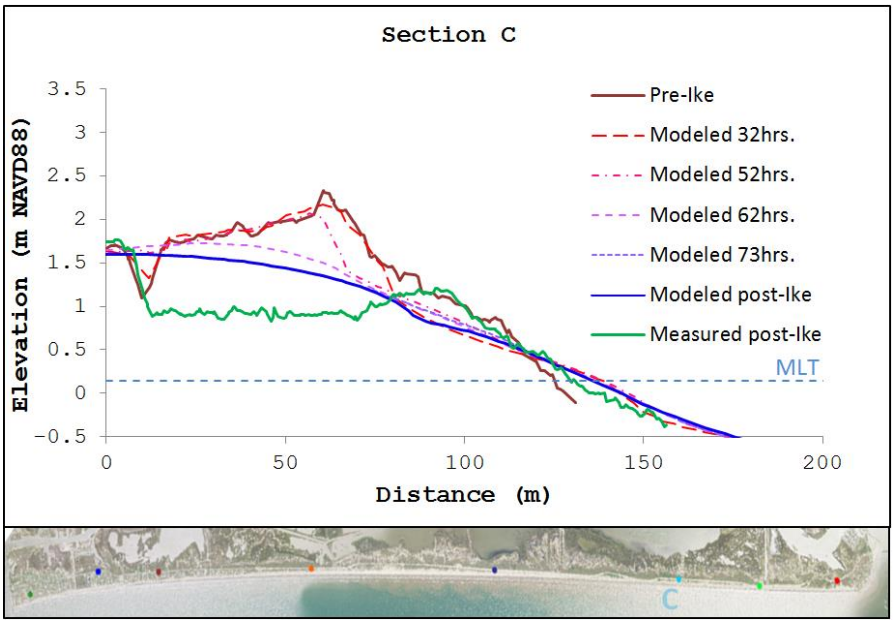

Figure D.3: XBeach simulated bed level evolution compared to pre- and post-storm bed level extracted from LiDAR data at Section C.

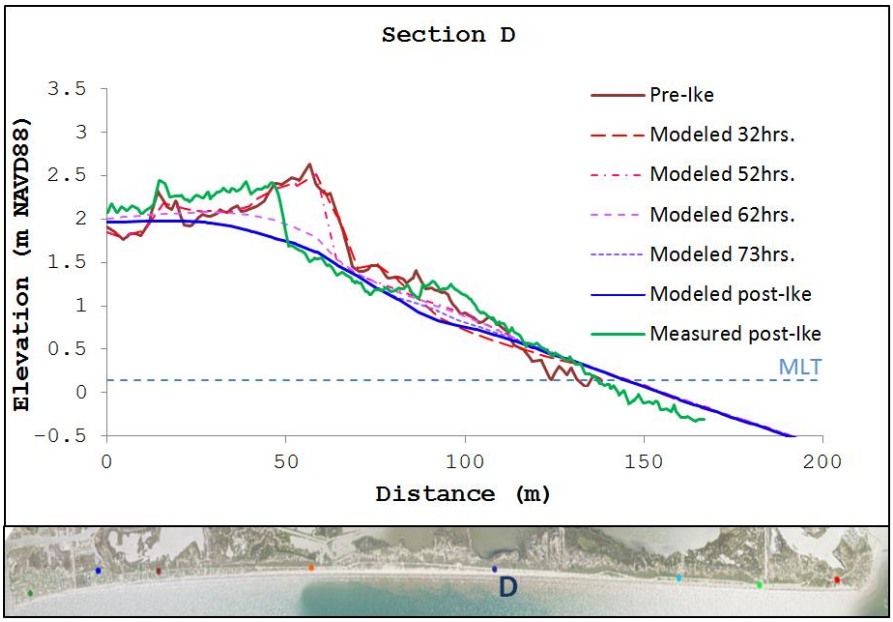

Figure D.4: XBeach simulated bed level evolution compared to pre- and post-storm bed level extracted from LiDAR data at Section D.

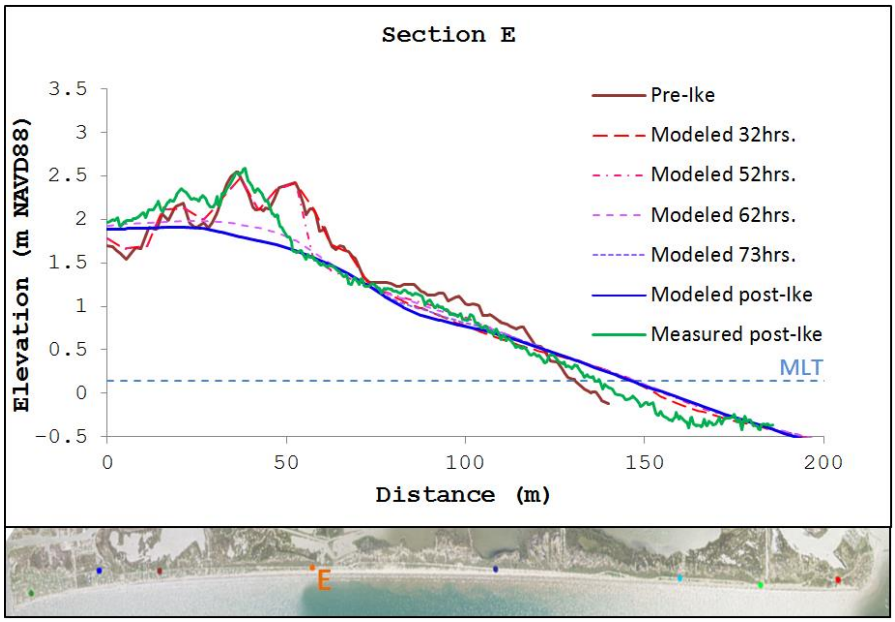

Figure D.5: XBeach simulated bed level evolution compared to pre- and post-storm bed level extracted from LiDAR data at Section E.

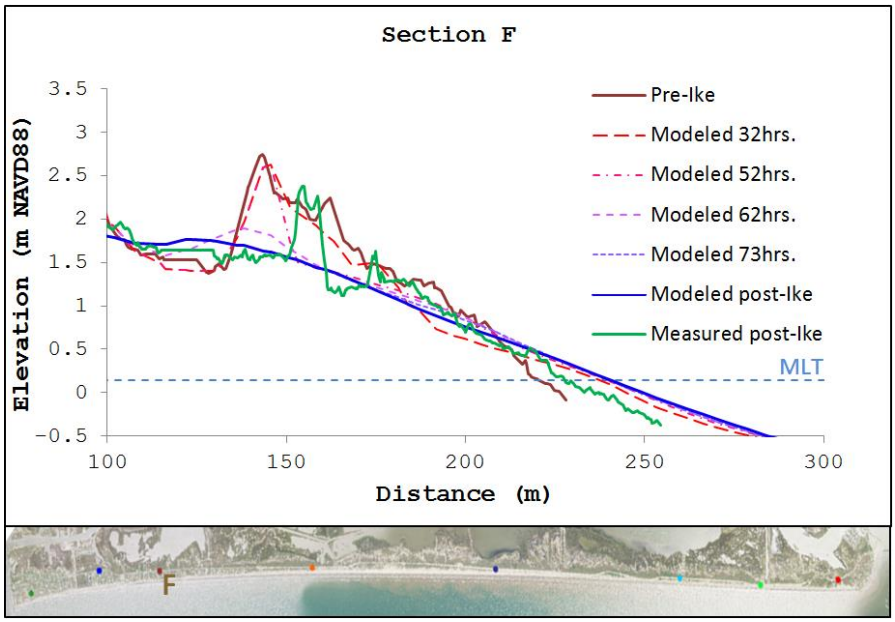

Figure D.6: XBeach simulated bed level evolution compared to pre- and post-storm bed level extracted from LiDAR data at Section F.

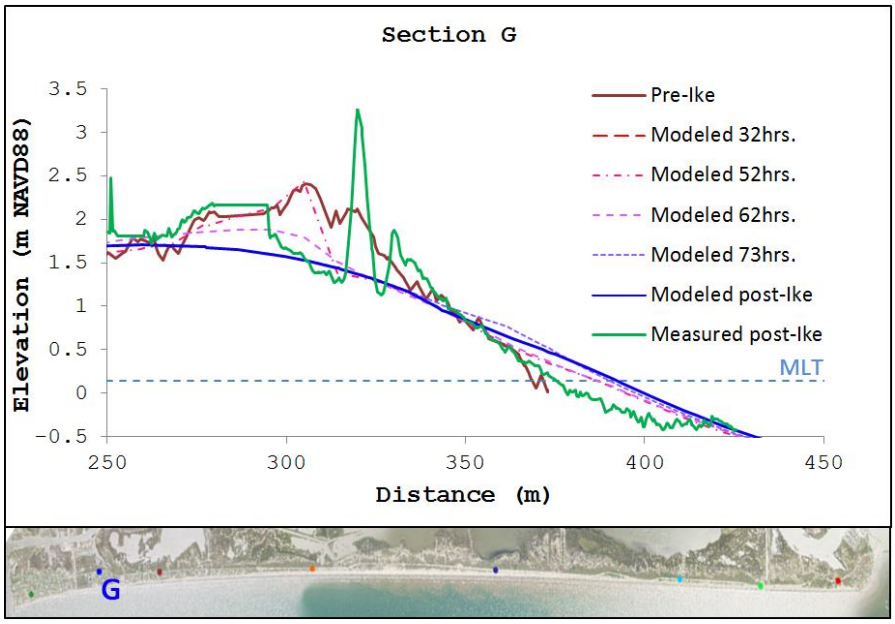

Figure D.7: XBeach simulated bed level evolution compared to pre- and post-storm bed level extracted from LiDAR data at Section G.

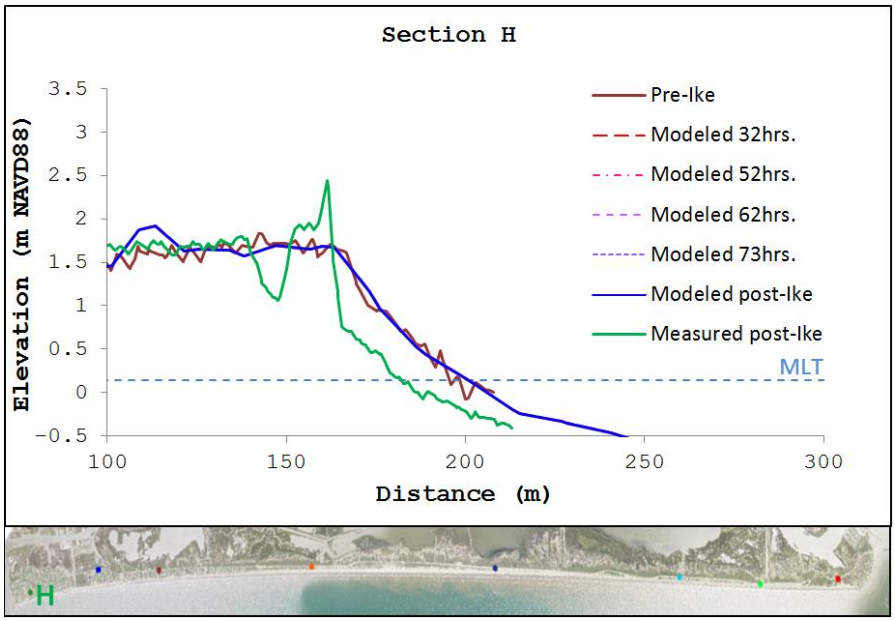

Figure D.8: XBeach simulated bed level evolution compared to pre- and post-storm bed level extracted from LiDAR data at Section H.

APPENDIX E

SECTION PLOTS OF CSHORE MODEL RESULTS

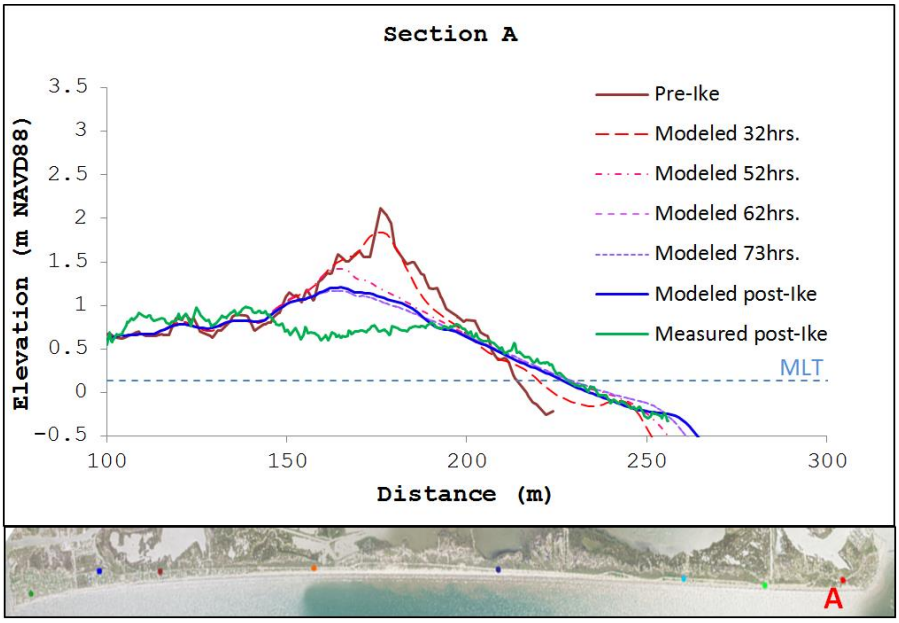

Figure E.1: XBeach simulated bed level evolution compared to pre- and post-storm bed level extracted from LiDAR data at Section A.

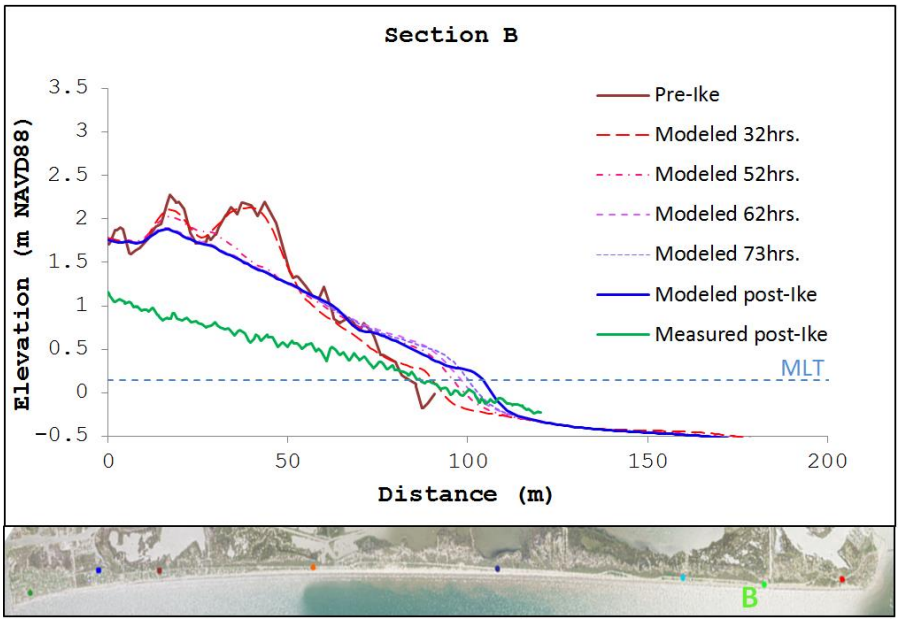

Figure E.2: XBeach simulated bed level evolution compared to pre- and post-storm bed level extracted from LiDAR data at Section B.

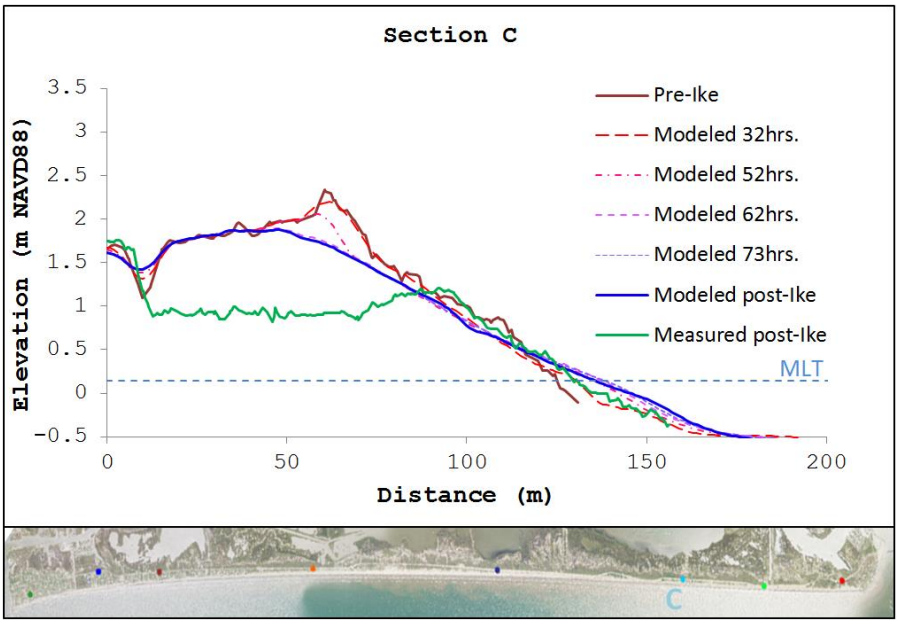

Figure E.3: XBeach simulated bed level evolution compared to pre- and post-storm bed level extracted from LiDAR data at Section C.

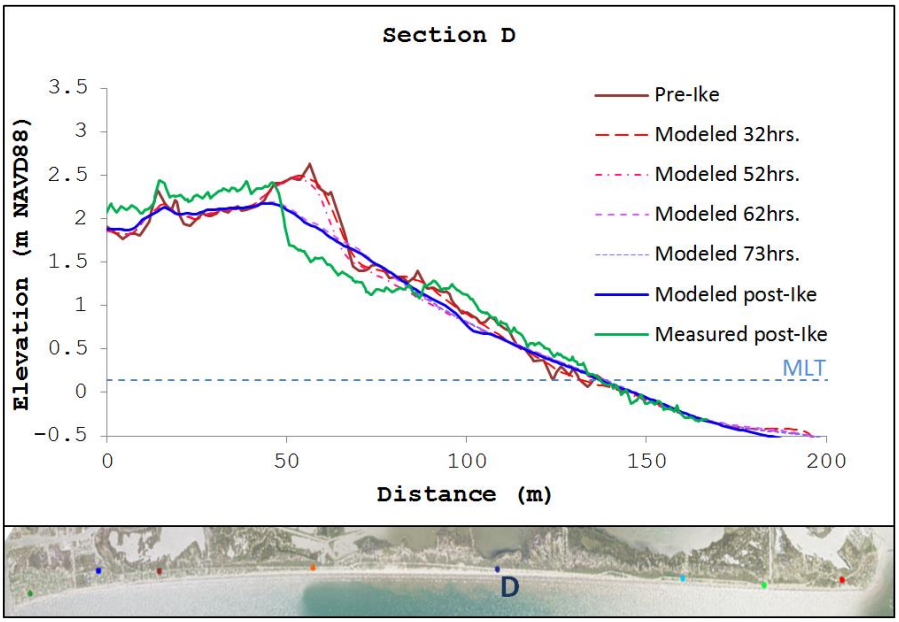

Figure E.4: XBeach simulated bed level evolution compared to pre- and post-storm bed level extracted from LiDAR data at Section D.

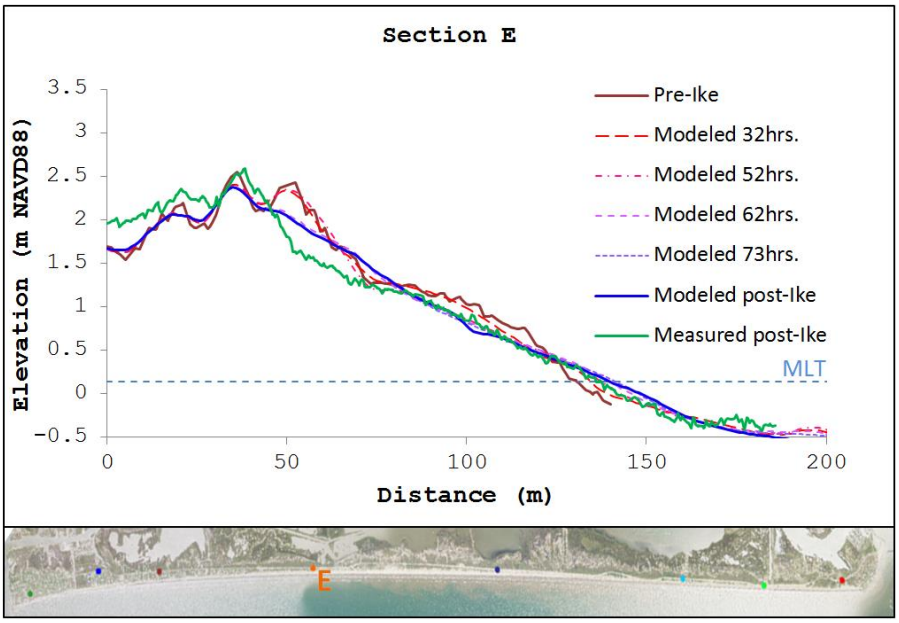

Figure E.5: XBeach simulated bed level evolution compared to pre- and post-storm bed level extracted from LiDAR data at Section E.

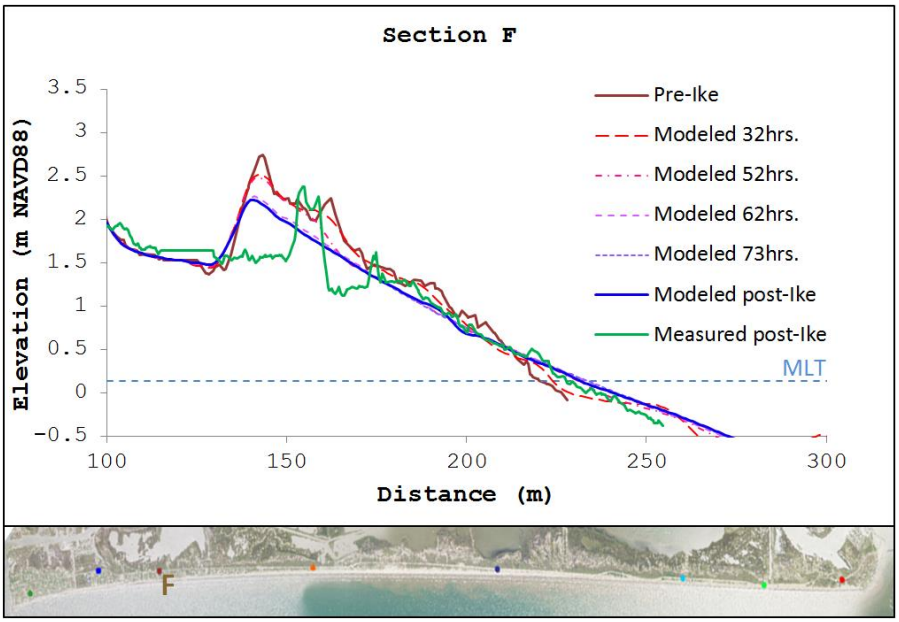

Figure E.6: XBeach simulated bed level evolution compared to pre- and post-storm bed level extracted from LiDAR data at Section F.

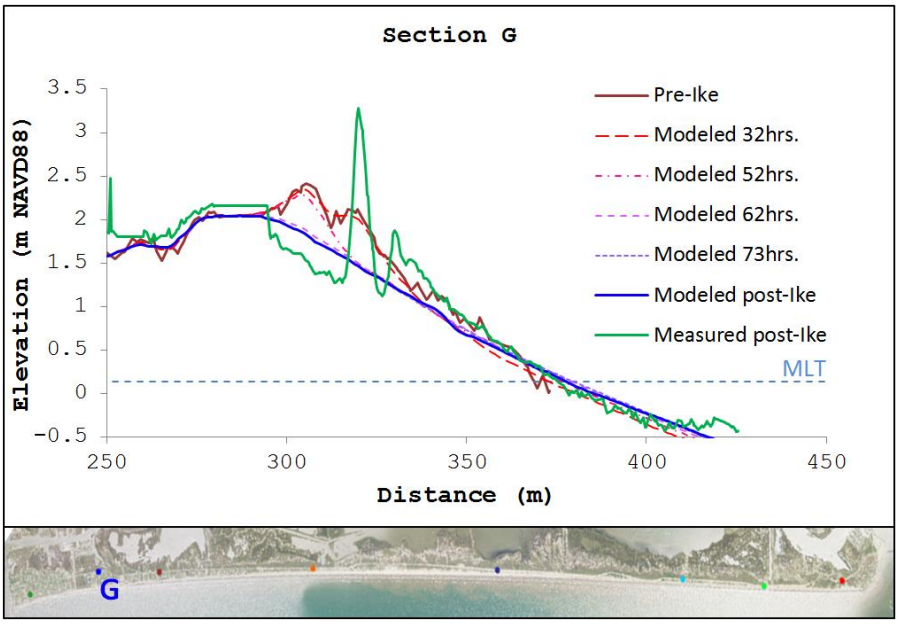

Figure E.7: XBeach simulated bed level evolution compared to pre- and post-storm bed level extracted from LiDAR data at Section G.

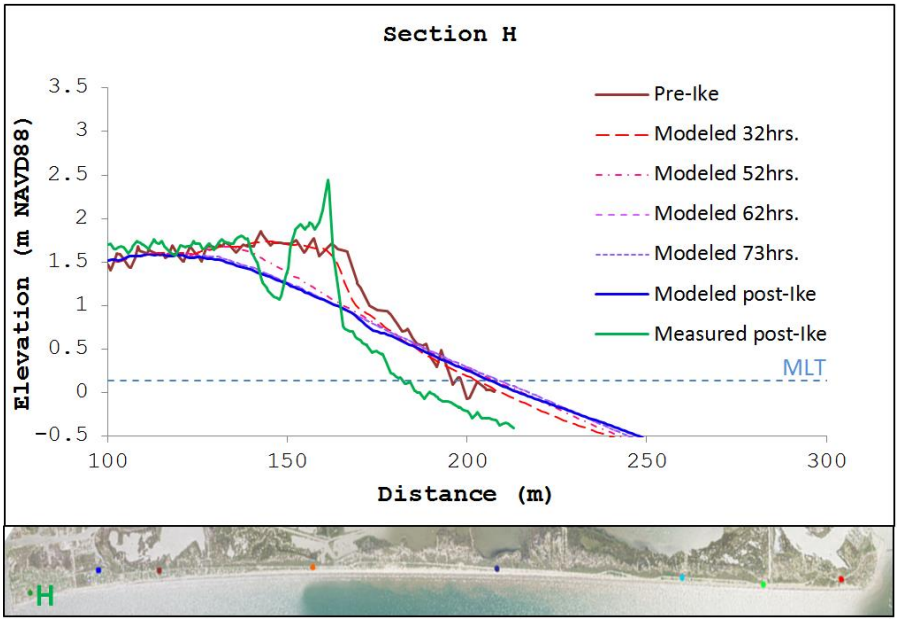

Figure E.8: XBeach simulated bed level evolution compared to pre- and post-storm bed level extracted from LiDAR data at Section H.